POLITECNICO DI TORINO

MASTER'S DEGREE COURSE IN MECHATRONIC ENGINEERING

MASTER'S DEGREE THESIS

Modeling and control design of a tyre test bench system

Supervisors

Prof. Massimo CANALE

Prof. Enrico GALVAGNO

Candidate

Davide DONGIOVANNI

December 2020

Abstract

The Tyre Test bench (TTB) of the Politecnico of Turin was developed until the end of the 90s for the analysis of the behavior of tyres up to the grip limit conditions. Subsequently, a revision of the TTB was undertaken aimed at its integration into an Hardware In the Loop (HIL) system, where a real tyre becomes one of the hardware components in the simulation loop.

According to this perspective, the TTB has been subjected to a review aimed at improving its measurement chains and, above all, allowing its management in a totally automatic mode.

The present thesis fits in this context. In particular, it is focused on the control of the system for the simulation of the vehicle motion.

The TTB simulates the road surface in contact with the tyre by means of a steel belt stretched between a driving roller and driven one. The relative position of the rotation axis of the driven rollers is adjusted by a pair of hydraulic actuators. Therefore, the control of the hydraulic actuators plays a fundamental role as it must guarantee both the necessary belt tensioning and its correct positioning during operation. The objective of this work is to achieve a rotation speed corresponding to a vehicle speed of $150\ km/h$.

In this thesis, a mathematical model of the driven roller actuation system and the belt drift motion were developed and experimentally validated. Subsequently, using the model, a controller was developed for the correct positioning of the belt. Finally, the developed controller was integrated into the machine control system, managed by a PLC, and experimentally tested.

Content index

- 3.2 Transversal drifting of the belt
- 3.3 Hydraulic model of the actuation system
  - Hydraulic piston
  - Hydraulic circuit
  - Directional proportional valve
- 3.4 Simulink model of the hydraulic actuator

- **Chapter 4: Experimental analysis and model validation**
  - 4.1 Experimental analysis on the hydraulic actuators
    - Model validation and parameters estimation
  - 4.2 Experimental validation of the belt reaction model
    - Experimental analysis of the belt forces
    - Experimental analysis of the belt translation speed and validation

- **Chapter 5: Control design for the hydraulic actuators**
  - 5.1 Hydraulic actuators identification and model validation
  - 5.2 Hydraulic actuator positioning control design
  - 5.3 Experimental analysis and validation of the actuator controlled in position

- **Chapter 6: Control design for the belt position**
  - 6.1 Identification of the actuators controlled in position
  - 6.2 Control system for the steel belt
    - Tensioning procedure
    - Belt centering design
    - Verification and validation of the centering system
  - 6.3 Controller implemented inside the PLC

- **Conclusions**
- **Thanks**
- **Bibliography**

Index of figures

Index of tables

Chapter 1

Tyre and tyre test benches

1.1 The tyre

The pneumatic wheel plays a fundamental role in the locomotion of land vehicles. They have the fundamental task of exchanging on the ground the forces necessary to achieve the motion of the vehicle, ensuring, at the same time, stability, limited energy dissipation and comfort. The pneumatic wheel consists of a rigid part, the rim, and a deformable part, the tyre, inside which a pressurized gas is introduced.

Parts of the tyre

A typical tyre is made up of about 60 different raw materials [1], each of which confers particular properties capable of modifying the characteristics of the overall product. Therefore, the combination of the tyre components must be balanced to comply with the performance indices required by the vehicle manufacturer. From the analysis of the chemical composition of a tyre, materials of various kinds are present, the main one being the synthetic and natural rubber that characterizes the compound, present in long polymer chains joined through the vulcanization process.

About 30% of the material consists of additives, such as silica, silanes and carbon black, that are used to improve rolling resistance and ensure less and regular wear of the compound.

The reinforcement materials make a crucial contribution in terms of performance and safety, they are present in concentrations ranging from 15% to 30%; among these

we find the steel wires, present both in the heel and in the belt, and textile materials, such as cables and cloths, present in the body ply (carcass). The former guarantees rim grip and driveability, while the latter gives shape and improves performance at high speeds.

Finally, in smaller percentages there are materials against aging, which protect the rubber from solar radiation, heat and oxidation (waxes and antioxidants), and resins and oils to improve the characteristics during the production process and give the compound rigidity.

Tyre structure

The tyres are classified according to their internal structure, they can contain an inner tube or to be of the Tubeless type, in which the air tightness of the inflation is fulfilled directly by the cover [2]. Nowadays, the second type is the most widespread as it is less subject to drilling; this requires that the rim has to be perfectly coupled to the heels of the tyre as it integrates the sealing function.

The tyre is made up of different parts, as shown in *figure 1.1*, which can be summarized in:

- *tread*: it is tyre element in direct contact with the ground; it plays a fundamental role in wheel-road interaction since, being responsible for the exchange of longitudinal and lateral forces, it allows traction, braking and steering actions. The tread pattern is characterized by the geometric shape of the grooves, which allow the water to be evacuated. It is made of synthetic rubber (styrene-butadiene SBR) which gives good resistance to abrasion and stability to aging, it must resist wear and protect the underlying carcass;
- *body ply*: it allows the transfer of the forces necessary to carry out all maneuvers and guarantees resistance to the inflation pressure. It is composed of Nylon threads placed side by side, hence the term cloth, which can be of variable thickness;
- *belt pack:* it consists in multiple layers of material wrapped in the circumferential direction between tread and carcass. It increases the strength of the tyre and prevent puncture damage. However, its main feature is to ensure a greater footprint on the ground resulting in a better distribution of the

forces exchanged with the ground, thanks to the ability to reduce the expansion due to centrifugal forces at high speeds.

They are made of steel, nylon or polyester ropes or wires arranged along the meridian plane or with reduced angles ($15° - 25°$). There may also be belts at different angles or a radial metal belt to better distribute the efforts.

- *sidewall*: it is the part of the tyre that connects the tread to the heel; it performs the fundamental role of transmitting the drive torque coming from the axle to the tread but, provides a minimal contribution in contrasting the vertical load. It has the task to protect the underlying carcass from abrasion, impacts with external bodies, bending fatigue and atmospheric agents; it is mainly composed of rubber reinforced with steel cords or fabric that guarantee tensile strength and flexibility, thus improving driveability and stability;
- *bead*: allows coupling with the rim; it consists of rubberised cloths to reduce wear due to the rubbing between these two bodies but it must ensure sufficient friction so that there is no relative rotation. The width of the heel strongly influences the driveability characteristic of the vehicle;
- *metal headbands*: steel bands placed inside the bead have the purpose of making the tyre-rim coupling rigid and avoiding any slipping. They can be shaped like a cable, with strands wound on a central core or with a single wire wound in a spiral. In any case, they are rubber-coated and drop-shaped profiles for appropriate coupling with the cloths;
- *reinforcements*: strips of material, usually elastomers, interposed between the tread-belt and the belt-carcass in order to better distribute the stresses generated by the contact between metal and plastic materials due to bending deformations. They are placed in the lateral areas where the edge of the steel belt could damage the rubber parts;
- *bead filler*: it is composed of rubbery material in order to fill the empty space that is generated, in the heel area, by wrapping the cloths around circles. Its mass and hardness variation affect the driveability characteristic of the tyre;
- *innerliner*: it is a thin rubber layer inserted inside the tubeless tyres. It is specially designed to prevent compressed air from escaping.

In *figure 1.1* it is possible to appreciate the section of a Tubeless radial tyre in which the main structures described above are identified by the following numbers: (1) liner, (2) body ply, (3) shoulder reinforcements, (4) headbands, (5) sidewall, (6) and (7) belt pack, (8) tread and (9) shoulder.

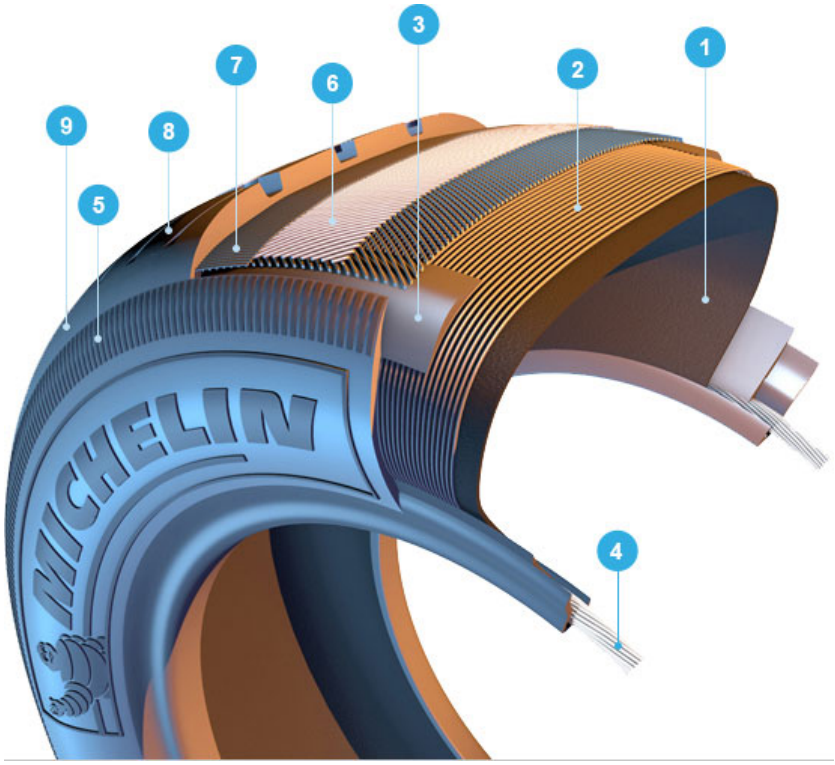

Fig. 1.1: Perspective section of a tubeless radial tyre

1.2 Tyre mechanics

In order to physically and mathematically characterize a tyre we have to define a schematic and sign convention for forces, moments and slip. In the following, it has been chosen to use the SAE convention adapted by Pacejka (*figure 1.2*). The traction or braking forces F_x are positive if they agree with the longitudinal axis x. The lateral ones F_y are positive if they agree with the orthogonal axis y. The convention define the drift angle α, the camber angle γ and the moment of self-alignment M_z [2].

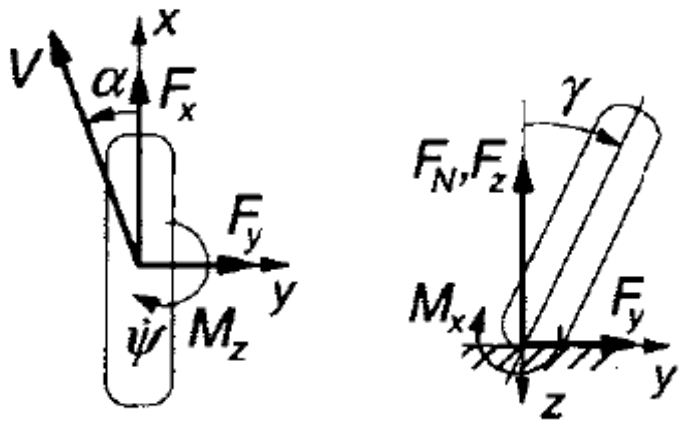

Fig. 1.2: Sign convention applied to the tyre

A fundamental tyre characteristic is its deformability due to vertical load, called elastic deformability to flattering; the nominal load F_z imposes on the tread a conformation designed to achieve optimal performance [3]. The tyre stiffness k_z is defined as the ratio between the load F_z and the deformation z:

$$k_z = \frac{F_z}{z} \tag{1.1}$$

Direct consequence of flattering is the effective rolling radius, defined, for a free wheel without torque applied to its axis, as the pseudo-radius of value R_e obtained by dividing the longitudinal velocity component V_x of the total velocity vector V by the angular rotational speed ω:

$$R_e = \frac{V_x}{\omega} \tag{1.2}$$

By examining a driven wheel (figure 1.3a), with no torque applied, a point of the tread entering in the tyre-road contact area shows a decreasing distance from the wheel center, passing from the undeformed radius to the effective rolling radius. It follows that the points inside the contact area move with a lower tangential speed than those outside it. The tread area located near the trailing edge will accelerate and will be subjected to a tractive effort; on the contrary, the tread area portion, which is close to the leading edge, decelerates and is compressed. In *figure 1.3* it possible to see the longitudinal trend of the surface stress and speed in the tread contact area.

If we consider a wheel on which a driving or braking torque acts, the trend of the efforts changes considerably. By considering a braking torque M_y applied to the wheel axis, this will be balanced by the longitudinal braking force $-F_x$ and by the vertical load F_Z. The application point of this latter force on the ground will be further away from the projection on the ground of the wheel center than in the driven wheel case. The tyre will be subjected to a sliding and by reducing the angular speed the effective rolling radius increases; for high braking torques it is also possible to obtain a radius R_e greater than the radius R_0 due to the flattering imposed by the vertical load. For this reason, the peripheral speed in the contact area may be higher than that in the unladen part of the tyre. Therefore, the tread area subjected to traction increases. The tread element located at the leading edge will be in adhesion and by moving forward in the tread area, the local speed increases. Therefore, also local deformations and tangential stresses increase until the adhesion limit imposed by Coulomb's law is reached. If this limit is exceeded, sliding begins and the tangential force decreases in the trailing part of the contact area. It fallows that the sliding is a local characteristic that refers to the single point of the tread in the contact.

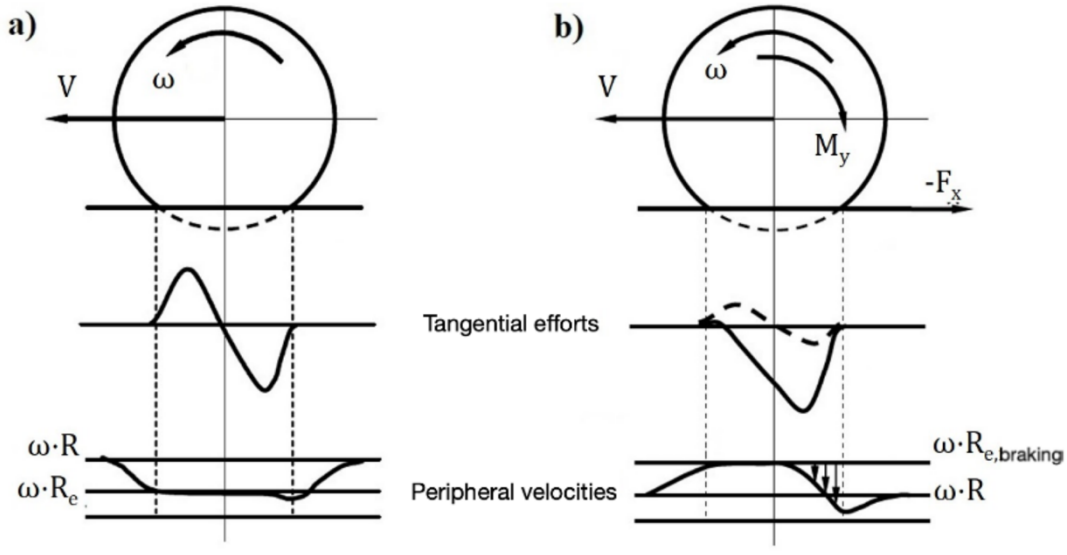

Fig. 1.3: Trend of tangential stresses and peripheral speeds in the contact area a) driven wheel; b) braked wheel.

Longitudinal slip

When a torque is applied in the same direction of the wheel angular velocity, the effective radius R_e decreases. Therefore, the peripheral speed in the leading contact area is lower than the speed of the portion of tyre not in contact with the ground. Therefore, the tread near to the leading edge is subjected to a tangential compression stress.

When a driving torque is applied to the wheel, a slip coefficient s is defined as:

$$s = -\frac{V_x - R_e\omega}{V_x} = \frac{\omega - \omega_0}{\omega_0} = \frac{\omega}{\omega_0} - 1 \tag{1.3}$$

The negative sign leads to a positive slip coefficient when a driving torque is applied; in this case, the angular velocity ω will be greater than ω_0. With the locked wheel, the slip coefficient is $s = -1$.

Unlike the sliding, the slipping is a global parameter that describes the motion of the rigid part of the wheel; it does not provide information on the adhesion or sliding conditons of the individual points in the contact area. It can be said that slip and sliding are two very different concepts: sliding is a local property of each contact point, while slippinig is a global property of the motion of the entire body [4].

To calculate the vehicle's forward speed, it is necessary to solve the vehicle's dynamic equilibrium equation; so, it is essential to know the trend of the longitudinal forces exchanged by the tyre as a function of the slip coefficient. The typical trends shown in *figure 1.4* are obtained from experimental tests. It can be noted that for low values of the slip coefficient s, the force is directly proportional to s and the longitudinal stiffness C_k can be defined as the tangent to the zero-slip curve. It is also possible to appreciate the proportionality between the longitudinal forces and the vertical load F_z. The peak of the curve is obtained for slip values between 0.1 and 0.15 and it represents the optimum force value during braking able to minimize stopping distance.

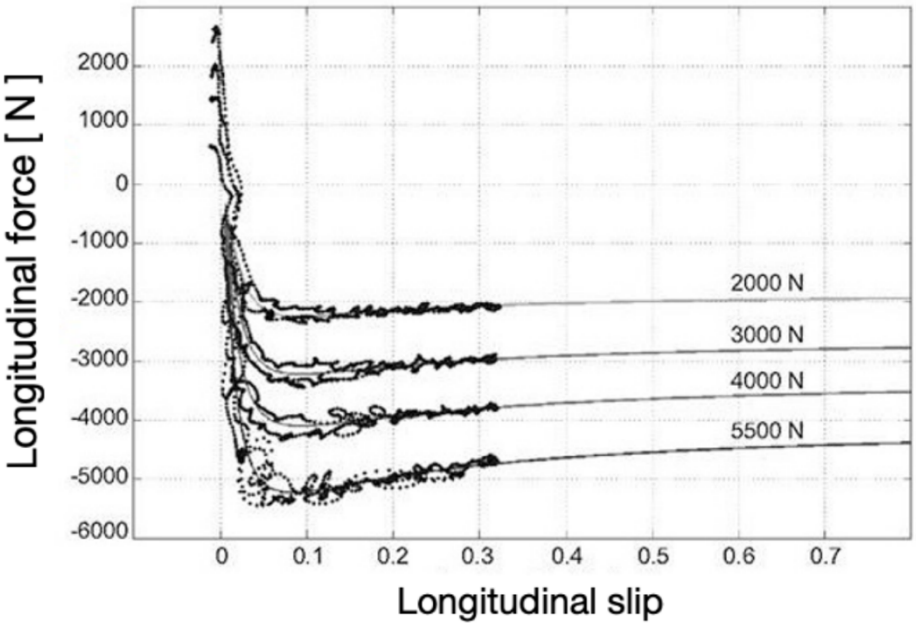

Fig. 1.4: Trend of the longitudinal force F_x as a function of the slip coefficient s and the vertical load F_z.

Generally, we refer to the longitudinal adhesion coefficient defined as:

$$\mu_X = \frac{F_x}{F_Z} \tag{1.4}$$

whose maximum value for tyres of civil use is around the unit.

Lateral slip

When a wheel is facing a curve, behavior similar to the acceleration/braking situation occurs. In this case, the forward speed vector will usually be not parallel to the median plane of the wheel. In the tyre-road contact area, the tread will begin to deform trying to align itself with the direction of the speed. In order to analyse the lateral slip, the drift angle α is introduced and it is defined as the arctangent of the ratio between the lateral and longitudinal component of the speed:

$$tan\alpha = -\frac{V_y}{V_x} \tag{1.5}$$

the negative sign has the purpose of making α positive when positive lateral force is applied.

As seen in the longitudinal case, in order to obtain the speed in the lateral direction V_y, it is necessary to solve the dynamic equilibrium equation of the entire vehicle. It follows that the trend of lateral forces as a function of the drift is required.

Figure 1.5a shows the trend of the forces exchanged in the lateral direction. It is possible to define a lateral stiffness $C_{y\alpha}$ as the tangent to the function at zero drift, where the force is linearly proportional to the drift angle.

The lateral stiffness is proportional to the vertical load, but this relationship is not linear.

Due to the rolling resistance, the point of application of the forces is displaced with respect to the projection on the contact track of the wheel center. For this reason, in addition to a lateral force, a concentrated torque is created, called self-alignment moment M_z. This tends to align the median plane of the wheel with the velocity vector, thus counteracting the deformation imposed by the lateral force. *Figure 1.5b* shows the trend of the self-alignment moment M_z as a function of the drift angle at different vertical loads.

Just as in the longitudinal forces case, it is possible to introduce the lateral adhesion coefficient as:

$$\mu_Y = \frac{F_Y}{F_Z} \tag{1.6}$$

whose peak values are around the unit for tyres of civil use.

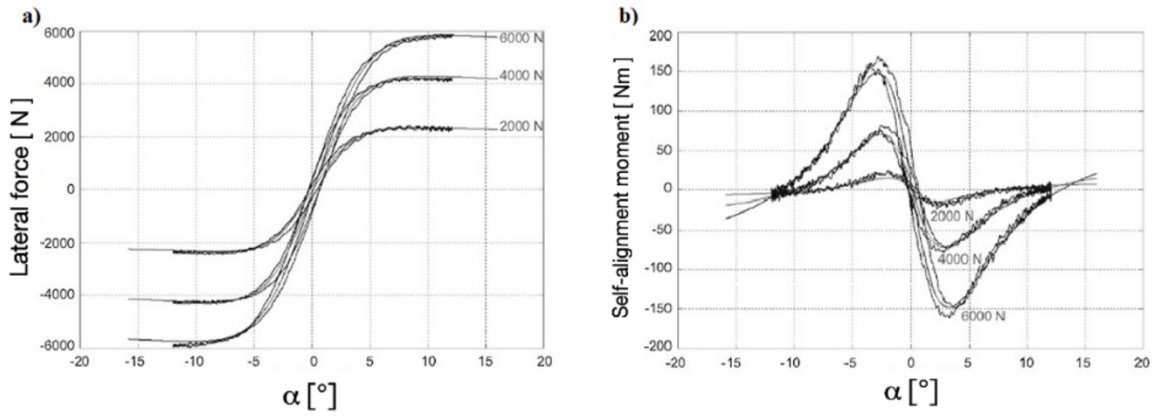

Fig. 1.5: Trends of the lateral force F_y (a) and of the self-alignment moment M_z (b) as a function of the drift angle α at different vertical loads F_z

A further parameter that influences the trend of lateral forces is the camber angle γ; it is defined as the angle between the median plane of the wheel and the normal to the road in the plane transverse to the vehicle. The presence of camber produces a lateral force that is usually much lower than that the one produced by the drift α [5].

1.3 Type of tyre test benches

From the discussion made in the previous paragraphs, it is clear that the tyre is a key element of the vehicle as a whole. For this reason, its design and development are fundamental in order to achieve objectives in terms of: safety and comfort of the driver and passengers, efficiency of the vehicle to reduce consumption and consequent polluting emissions, and fulfilling the performance required by the user.
For these reasons, since the 1960s, the world of research, both industrial and academic, has understood the importance of having experimental data on the main characteristics of a tyre and has begun to think of machinery that would allow them to be obtained.
From the beginning it became clear that the relative friction between the tyre and the ground plays a fundamental role. The first tyre testing machines were heavy vehicles, whose trolleys were adapted to be able to mount a test wheel that was in contact with the real road, the so-called Tyre Test Trailer (*figure 1.6*).

Fig. 1.6: Modern tyre test trailer example

In 1970 the Cornell Aeronautical Laboratory in Buffalo, New York, designs, patents and builds the first large-scale machine for laboratory tyre testing. This is the first machine to use a steel belt to simulate the road.

Tyre testing machines can be classified according to how the road surface is simulated: it is possible to distinguish between roller machines and flat belt machines. The figure 1.7 reports an example of both the tyre test benches (*TTB*). Roller machines can also be divided into concave curvature and convex curvature. The difference between them lies in the relative position between roller and wheel. In the concave curvature machines, the wheel is inside the roller; in the convex ones, the wheel is. The simulation of the road through a curved surface causes important and complex variations in the measurement of the forces and the moments exchanged by the tyre.

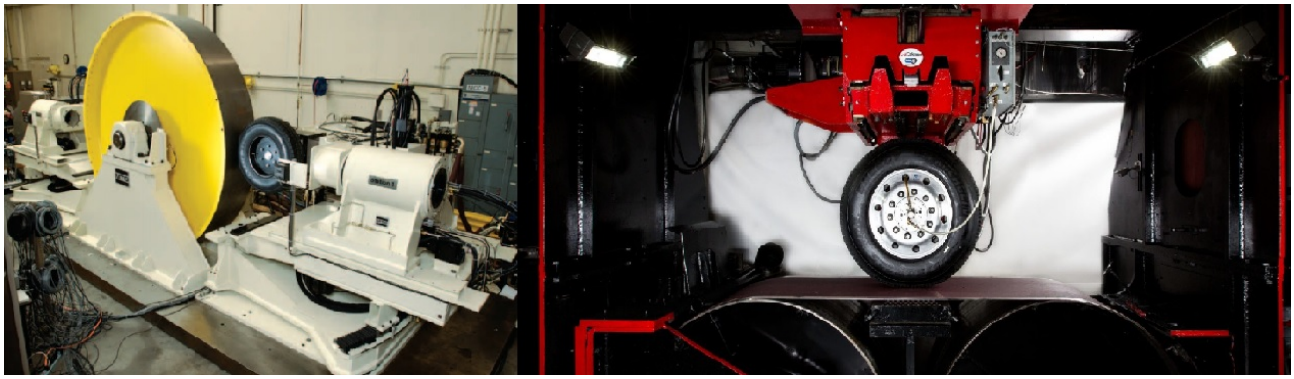

Fig. 1.7: Type of tyre test benches: roller machine (left) and flat belt machine (right)

The flat belt tyre test benches typically consists of a steel belt wound on two large rollers, one of which is usually moved by a motor. These machines are able to control the slip if the motor of the wheel and the motor of the driving roller are controlled independently. The contact area is located in the middle, where the belt is flat and is held in position by a special mechanical, static or dynamic bearing below.

1.4 The tyre test bench of the Energy Department of Polito

The tyre testing machine, installed in the laboratory of the Energy Department of the Polytechnic of Turin, was designed and developed by Prof. Alberto Morelli between the end of the 70s and the first half of the 80s.

At the time, the test bench was totally mechanical and in order to be able to perform tyre tests, it was necessary to continually calibrate and set up by specialized users.

Motion generation and transmission

The machine is of the flat belt type, made of stainless steel. *Figure 1.8*, *figure 1.9* and *figure 1.10* show the front, side and rear views in which it is possible to identify all the main systems and devices that make up the tyre test bench and which will be described below.

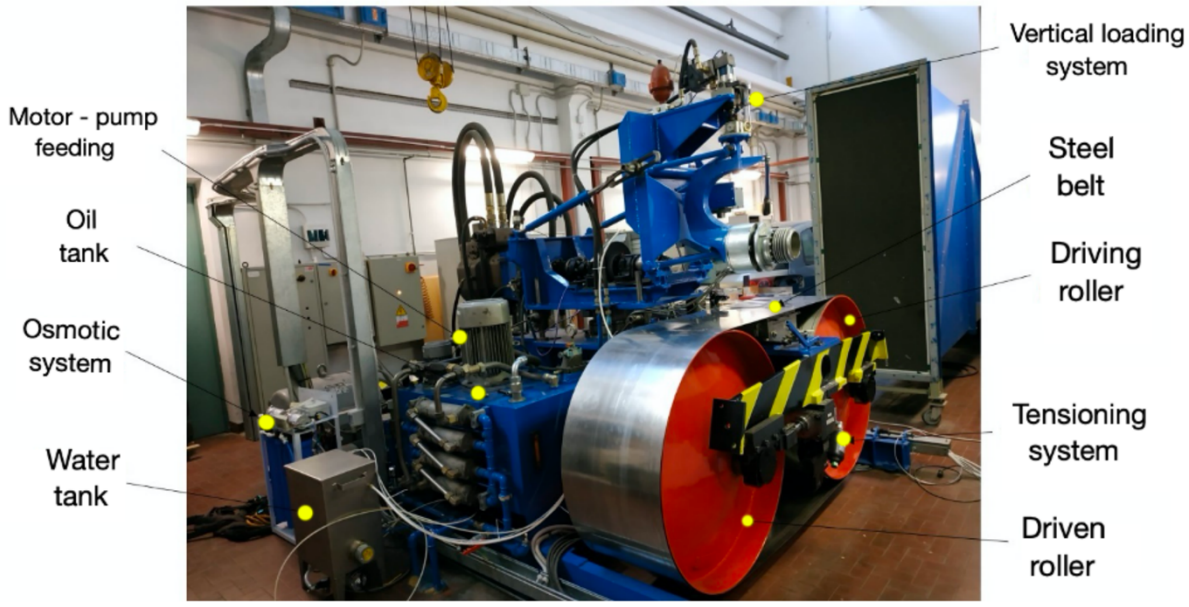

Fig. 1.8: Front view of the Polito's tyre test bench

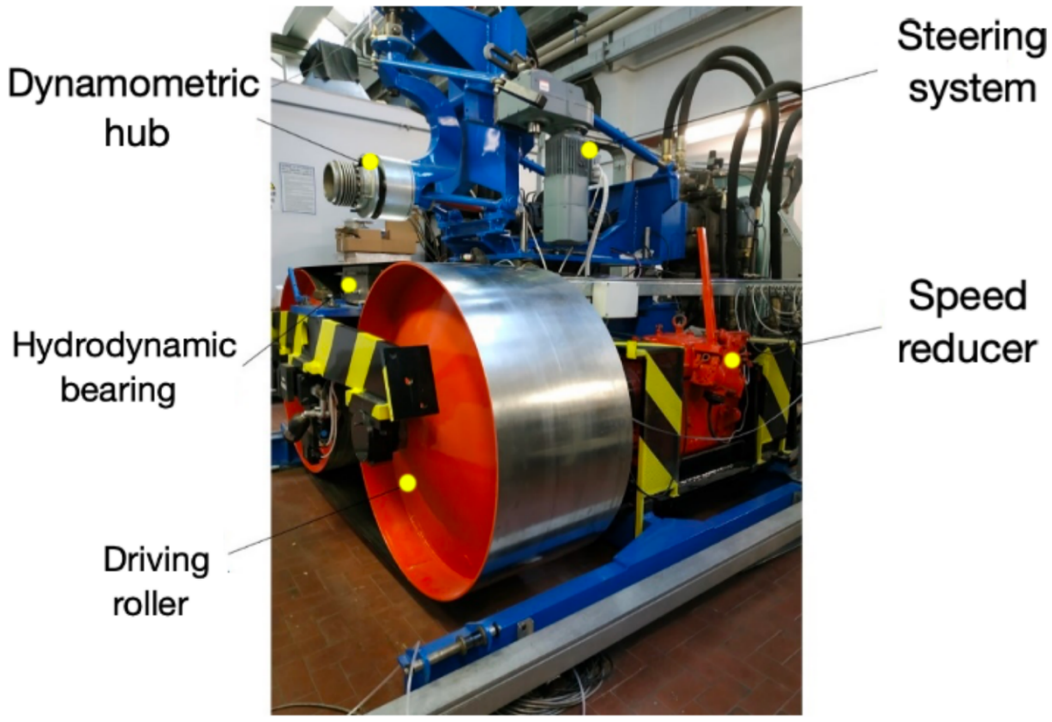

Fig. 1.9: Side view of the Polito's tyre test bench

Fig. 1.10: Rear view of the Polito's tyre test bench

The wheel and belt motions are obtained by means of closed-circuit hydraulic transmissions, carried out by means of variable displacement pump-motors, the schematizations of which are shown in *figure 1.11*. The hydraulic machines, pluricylindrical volumetric axial pistons, which constitute the primary and the secondary of each transmission, have a maximum displacement of $250\ cm^3$ and $225\ cm^3$, respectively. These hydrostatic transmissions can operate up to a pressure of $350\ bar$. The pumps and motors displacement can be varied continuously by means of electric motors or hydraulic circuits, making possible to pass from conditions of slipping in traction to locking of the wheel during braking. The forward and return flow circuits are connected by a normally closed pressure relief valve. This allows, in the event of high pressure in one of the two branches, the short-circuiting of the motor, so as to evacuate the excess flow rate and restore the correct pressure value. The maximum motor rotation speed is $2800\ rpm$. The pumps of both transmissions are connected to the same shaft, connected to a three-phase asynchronous electric motor that rotates at a constant speed of $1450\ rpm$.

The closed circuit conformation with a single electric motor allows a balance of the powers involved between the two transmissions. As matter of fact, one braking of the wheel corresponds to the traction of the belt and vice versa, the connection of the

transmission allows the recovery of the energy released by the braking element, which is transferred to the pulling element. This configuration allows, despite each hydrostatic transmission having a nominal power of $350\ kW$, to power the entire bench with a single $100\ kW$ electric motor [6].

A five-gear speed reducer for industrial vehicles is interposed along the belt transmission between the output shaft of the hydraulic motor and the roller hub. This allows to adapt the speed range of the rollers to that of the wheel; the selection of the transmission ratio is made at the beginning of the test and cannot be changed while the machine is running. The speed reduction ratios are shown in Table 1.1, defined as:

$$\tau = \frac{n_{motor}}{n_{Roller}} \tag{1.7}$$

where n indicates the rotation velocity.

Gear	τ [−]
I	8,67
II	4,71
III	2,46
IV	1,38
R	-7,40

Tab 1.1 – Speed reducer ratios

The belt is supported and moved by two steel rollers with a diameter of $1\ \mathrm{m}$, one motorized and the other idle.

The wheel is constrained by a dynamometric hub to a suspension with transverse quadrilaterals (parallelograms) whose direction of shaking is perpendicular to the plane of the belt. The suspension is able to steer and allows variations in the drift angle α in the range $-25\,° < \alpha < +25\,°$. Its movement is achieved by means of an electromechanical drive consisting of a three-phase electric motor, whose rated power is $1.1\ \mathrm{kW}$ and its speed is $1415\ \mathrm{rpm}$, combined with a speed reducer with a ratio of 83.5.

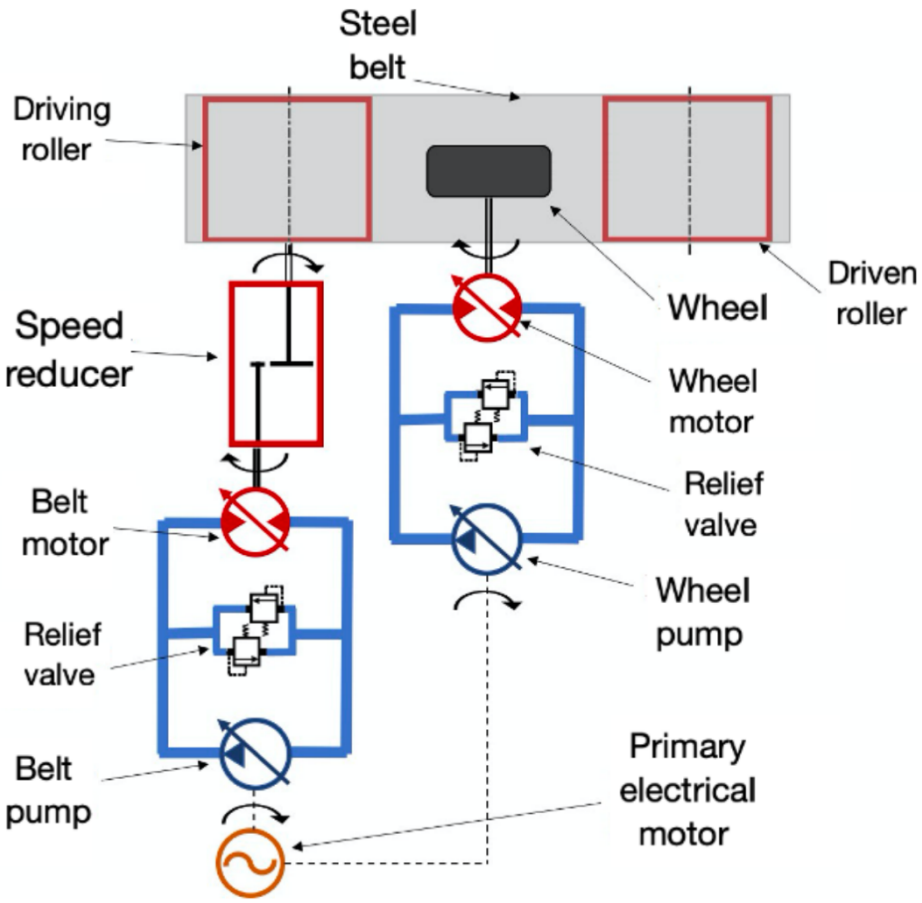

Fig. 1.11: Simplified hydraulic / mechanical scheme of the TTB

The flattering of the tyre is obtained with a hydraulic servo-actuator capable of imposing a maximum vertical load of $25\ \mathrm{kN}$, this also allows dynamic variations with frequencies up to $100\ \mathrm{Hz}$. This configuration allows to approximate constant load conditions during the tests, regardless of the operating conditions of speed, drift and slipping.

The variation of the camber angle ($0\,° < \gamma < 30\,°$) is obtained by tilting, with the machine stopped, the support structure of the quadrilateral suspension with respect to the rolling surface.

Road simulation surface

The main classification feature of a TTB has been found to be the simulation surface of the road. In this machine, it consists of a stainless steel belt; this was achieved by welding a sheet of metal with a width of $450\ mm$ and a thickness of $0.8\ mm$.

The belt is set in motion by two steel rollers with a diameter of $1\ m$ and supported in the area of contact with the tyre by a hydrodynamic bearing. It is placed under tension by means of two double-acting hydraulic cylinders, acting on the axis of the driven roller. The two actuators, independent of each other, also make possible to tilt the rotation axis of the roller. The double-acting cylinders are controlled by a proportional solenoid valve which, by generating a pressure imbalance between the two chambers of the actuator, manages the displacement of the piston and therefore the release of the rod. For control purposes, there is a magnetostrictive position transducer (with a resolution of *0.01 mm*), incorporated in the cylinder structure, and a couple of pressure transducers in the connecting lines.

The hydropower supply of the actuation subsystem is guaranteed by a volumetric pump with internal gears that guarantees a constant delivery flow rate. Figure 1.12 shows a photograph depicting the hydraulic devices acting on the driven roller for its control. In particular, the following are indicated: driven roller (1), double-acting hydraulic cylinder (2), position sensor (3), pressure transducers (4), proportional solenoid valve (5).

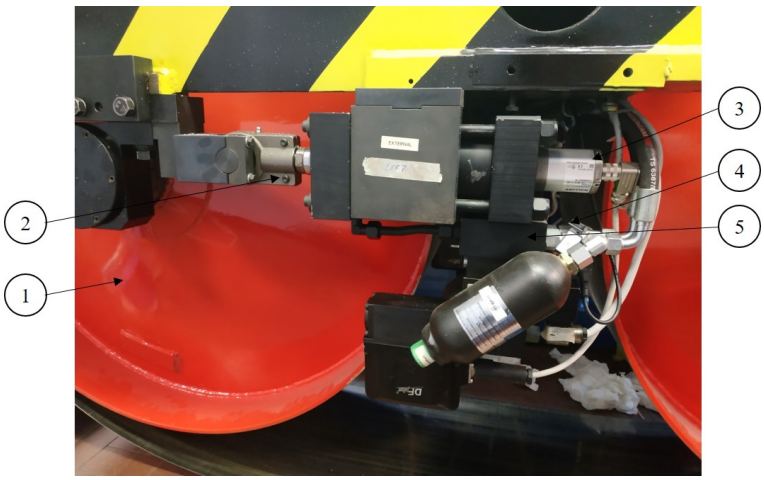

Fig. 1.12: Hydraulic actuator

Control and measurement systems

The entire machine, including all auxiliaries, is managed by a Beckhoff CX-2577EC Programmable Logic Controller (PLC); this multifunctional controller allows, in addition to the sequential logic functions, measurement, regulation, positioning and control operations. A PLC is composed of a central unit (CPU), it is the brain of the system that organizes the activities of the controller, one or more input/output units (I/O), which allow the connection between the central unit and the system to be controlled, and a programming unit, which allows the human interface with the machine. The latter consists of an Asem touchscreen panel.

The I/O system of the PLC manages analogical signal and digital signal. The digital communication between the devices is performed by using Profibus (Process Field Bus).

Two Kistler torque transducers are located on the transmission shafts, one located between the output shaft of the speed reducer and the roller hub and the other between the shaft coming out of the hydraulic motor and the wheel. Both measure the torque and the angular speed of the respective transmission, the first with a full scale of $3\ kNm$ and the second of $2\ kNm$. The same technology (Profibus) is used for the weighing system (vertical load on the tyre), consisting of four load cells located under the hydrodynamic bearing. The profibus protocol is also used for communication between PLC and the absolute multiturn encoder that equips the electric gearmotor, for the variation of the steering angle of the wheel, and the relative inverter.

The control and compensation of the lateral displacements of the belt with respect to the rollers are carried out by means of two actuators operated by differential solenoid valves. A Keyence multifunction laser micrometer, based on CCD technology, is used for measuring the belt position. Extremely precise discrimination is achieved by acquiring the edge of the through-beam laser light, rather than the amount of light received. It allows the measurement of a displacement of $0.2\ mm$ with sampling frequencies higher than $1\ kHz$.

The main element around which the machine was designed is the five-component dynamometric hub that allows the measurement of the forces and torques exchanged on contact between the wheel and the belt. The longitudinal and normal forces

exchanged between the belt and the tyre induce shear stresses inside the columns equipped with strain gauges, which constitute the sensitive elements of the hub.

The PLC is programmed by means of the TWINCAT 3 suite and it has been extended in order to allow the direct integration of Matlab's Simulink models.

Chapter 2

Theoretical analysis and estimations

The following chapter shows some theoretical analyzes regarding the steel belt and the actuation system. In the first part, the belt stress under the TTB working condition is analyzed. Based on this first analysis, the maximum stress to which the belt can be brought is estimated.
Successively, after a brief analysis of the forces that acts on the belt, the minimum belt tension required in order to avoid the relative sliding between belt and rollers along longitudinal and transversal directions is estimated.

2.1 Stress analysis

The steel belt inside the TTB is subject to a system of forces coming from the rollers and the tyre. In order to avoid excessive deformation or damages to the belt, the belt stress has to be lower than certain limits.
The total belt stress results from three different effects [7]: bending stress, centrifugal stress and tight/slack side stress. In the following paragraph, these stresses are analyzed in order to estimate the limit working conditions of the belt.

Bending stress:

It occurs because the belt is rotating around the rollers. In particular, defining the neutral axis as the one not subject to bending, the belt is compressed in the belt portion below the axis, while it is stretched in the above part.
It is possible to estimate the bending stress as:

$$\sigma_b = \frac{E\ t}{(1-\nu^2)D} \tag{2.1}$$

where:

- E is the material Young's modulus;
- t is the thickness of the belt;
- ν is the material Poisson's modulus;
- D is the rollers diameter.

It follows that σ_b does not depend on the system working condition and its value can be estimated as:

$$\sigma_b = \frac{2{,}1\ 10^{11}\ 0.8\ 10^{-3}}{(1-0.33^2)\ 1} = 189MPa$$

Centrifugal stress:
It is due to the centrifugal forces acting on the belt rotating around the rollers.
It depends on the belt material and its working velocity and it is equally distributed throughout the belt during operation.
It is possible to estimate the centrifugal stress as:

$$\sigma_{cf} = \rho\ v^2 \tag{2.2}$$

where:

- ρ is the density of the belt material;
- v is the tangential velocity of the belt.

It follows that σ_{cf} depends on the system working condition. By considering a maximum velocity of $150\ km/h$, its value can be estimated as:

$$\sigma_{cf} = 7800\ \left(\frac{150}{3{,}6}\right)^2 = 14MPa$$

Tight side-stress:

It represents the stress along the straight side of the belt. Inside our TTB, its value depends on the preload applied by the hydraulic actuators and consequently on the force exerted by the driven roller to the belt.

It is possible to evaluate the stress as:

$$\sigma_t = \frac{T}{A} \tag{2.3}$$

where:

- T is the tensile force in the straight side of the belt;
- A is the cross-sectional area of the belt.

The *figure 2.1* reports a simple schematization of the considered forces. The thrust force of both the hydraulic actuators is identified as F_F.

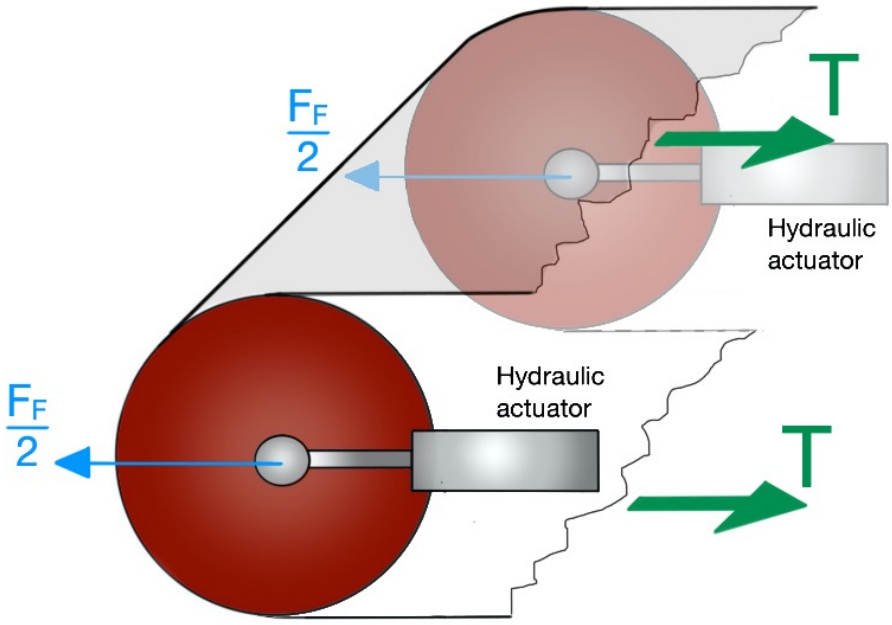

Fig. 2.1: Schematization of the thrust force generated by the hydraulic actuators

2.2 Estimation of the belt preload

As the previous paragraph shows, the tensile force depends on the working condition. Therefore, it is important to estimate the belt preload that has to be provided by the hydraulic actuators.

The total belt stress can be obtained as:

$$\sigma_{tot} = \sigma_b + \sigma_{cf} + \sigma_t \tag{2.4}$$

Considering the tearing of the belt as superior limit, it is possible to approximate σ_{tot} to the $U.T.S.$ of the steel belt with the welding.

Considering the working scenario, the tearing of the steel belt can heavily damage the TTB and it has to be firmly avoided.

A possible design guideline is to consider as upper limit for the stress the $\sigma_{0.01\%}$. This choice implies also a minimal and elastic deformation of the steel belt.

By considering the worst case scenario, where $\sigma_b = 189\,MPa$, $\sigma_{cf} = 14\,MPa$ and $\sigma_{0.01\%} = 440\,MPa$, we could apply a belt preload able to generate a tight side stress up to $\sigma_t \cong 240\,MPa$. In order to have a high safety factor, the maximum preload of the belt is limited by applying static stress around $110\,MPa$ at most.

Considering the above scenario, the preload of the belt will be equal to:

$$\boxed{T = \sigma_t\, L\, t \cong 40\,kN}$$

this is the preload applied by each of the hydraulic actuator of the driven roller. In the following, we will consider the sum of the thrust forces provided by the hydraulic actuators F_F equal to $80\,kN$.

The application of a preload lower than the estimated one, ensure a safety factor higher than:

$$S.F. \geq \frac{U.T.S.}{\sigma_{tot}} = 2.8$$

where the considered $U.T.S.$ is equal to 1240 MPa for the steel of our belt.

2.3 Rollers-belt dynamical analysis

The following paragraph analyzes the forces exchanged between the roller and the belt. Based on the forces along the longitudinal and transverse directions, the preload to be provided by the hydraulic actuators is estimated.

Dynamical analysis along the longitudinal direction

Inside the TTB there are multiple forces and couples that need to be analyzed in order to be able of conduct tests on a tyre. The *figure 2.2* shows the belt-roller system from a lateral point of view.

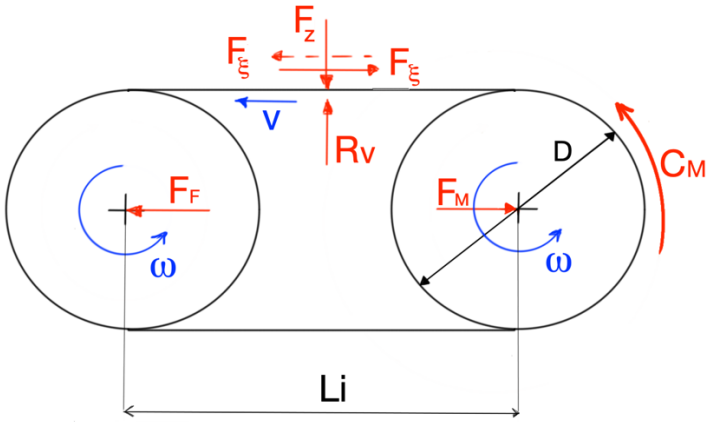

Fig. 2.2: Schematization of the main forces and couples acting inside the TTB

F_z is the loading force acting on the tyre, F_ξ is the force exchanged between tyre and belt along the longitudinal direction of the belt, R_v is the axial journal bearing reaction, C_M is the torque imposed by the motor to the driving roller.

F_F and F_M represent the thrust force of the actuator and the constraint force along the belt longitudinal direction, respectively.

The force F_ξ can be directed from the driving roller to the driven one and vice versa. Therefore, in the following formulas it is reported as $\pm F_\xi$ (+ sign from the driven to the driving roller direction).

The balance of forces and couples acting inside the TTB can be analyzed as follow:

System dynamic equilibrium

$$F_F = F_M \pm F_\xi$$

$$C_M = \pm F_\xi \frac{D}{2}$$

Driven roller dynamic equilibrium

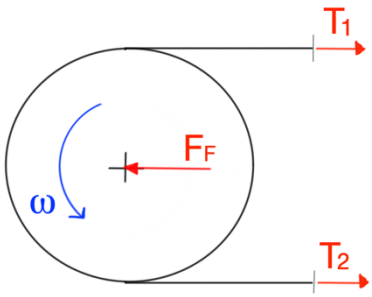

$$F_F = T_1 + T_2$$

$$T_1 = T_2 = \frac{F_F}{2}$$

Driving roller dynamic equilibrium

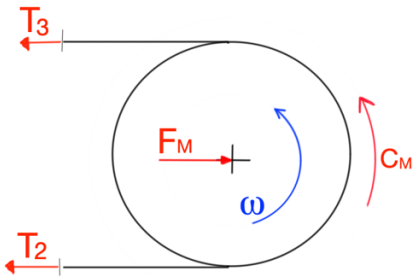

$$F_M = T_3 + T_2$$

$$C_M = (T_2 - T_3)\frac{D}{2}$$

Belt dynamic equilibrium

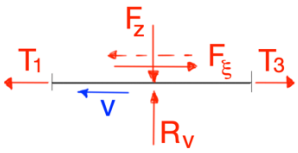

$$T_1 = T_3 \pm F_\xi$$

$$F_z = R_v$$

Variation in the belt stress and velocity

The relationships between the belt stretching and the velocity of the roller can be analyzed by applying the belt friction theory [8]. It is known that, at the beginning of the contact among belt and pulley, it possible to define a grip angle θ' followed by a slip angle θ^* as show in *figure 2.3*. In the grip angle the belt stress does not change. In the slip angle the inlet tension matches the outlet one by following an exponential law.

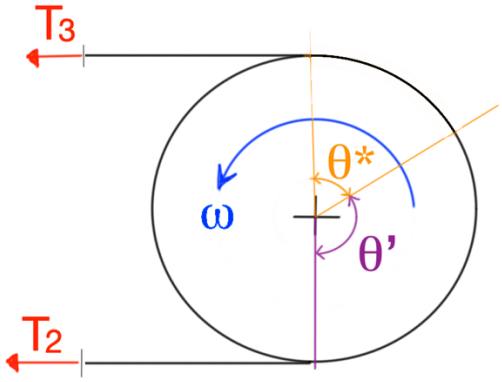

Fig. 2.3: Grip angle θ' and slip angle θ^* in the driving roller

At the same time, the local velocity of the belt changes in accordance with the tension as:

$$v = v_0(1 + \frac{T}{E\,S})$$

where v_0 is the velocity of the belt at null tension and S is the belt cross-section area. It follows that the most stressed belt side has a higher speed.

When the force F_ξ exchanged between tyre and belt along the longitudinal direction of the belt is equal to zero, the belt tension is constant everywhere and equal to a half of F_F.

By applying a F_ξ, i.e. when the tyre is braking or accelerating with respect to the belt, the motor has to apply a torque able to balance the F_ξ effect:

$$C_M = \mp F_\xi \frac{D}{2}$$

By assuming the rotational velocity of the driving roller to be constant, the belt velocity along the grip angle of the driving roller is constant too. It follows that the belt velocity and the belt tension vary only along the slip angle portion of the driving roller. The *figure 2.4a* represents the condition where the tyre is accelerating with respect to the belt, while in *figure 2.4b* it is shown the velocity of the steel belt when the tyre is decelerating with respect to the belt.

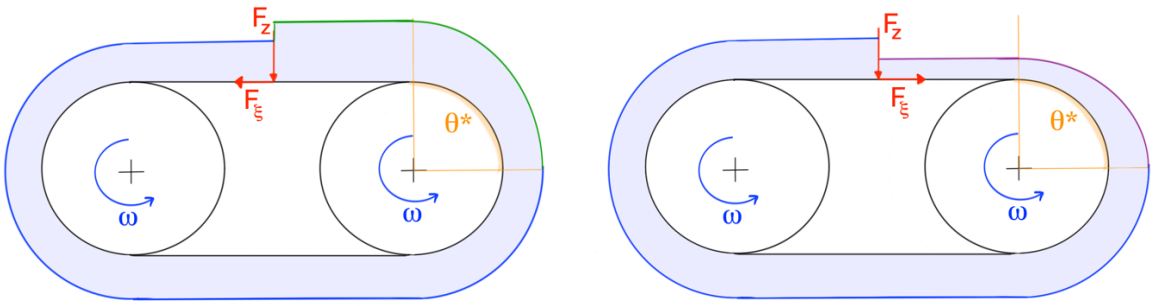

a) F_ξ *negative* b) F_ξ *positive*

Fig. 2.4: Variation in the belt velocity caused by the tyre longitudinal force F_ξ

It follows that the rotational speed of the driven roller is not affected by F_ξ as well as its inlet and outlet tension.

Tangential adherence

When the slip angle $\vartheta^*$of the driving roller reaches its maximum value, which is equal to 180°, the slipping condition on the roller is obtained. This working condition can be associated to the maximum force F_ξ that can be applied to our system.

When F_ξ is positive, we can sketch:

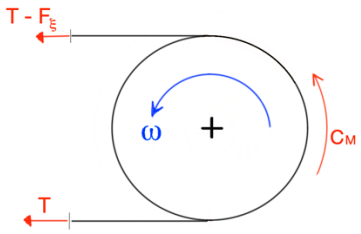

In this condition we have:

$$\frac{T}{T - F_\xi} = e^{f\vartheta^*}$$

that can be written as:

$$F_\xi = T\left(1 - e^{-f\vartheta^*}\right) \leq T(1 - e^{-f\pi}) = F_{\xi\,max} \tag{2.5}$$

When F_ξ is negative, we can sketch:

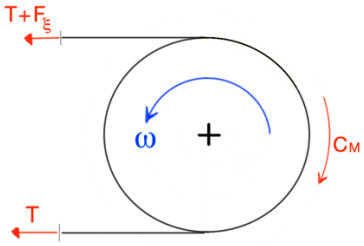

In this condition we have:

$$\frac{T + F_\xi}{T} = e^{f\vartheta^*}$$

that can be written as:

$$F_\xi = T\left(e^{f\vartheta^*} - 1\right) \leq T(e^{f\pi} - 1) = F_{\xi\,max} \tag{2.6}$$

Dynamical analysis along the transversal direction

The experimental analysis evidences that steel belt can drift along the transversal direction when the system is rotating. It is important to investigate this phenomenon in order to be able to control it.

Before starting the analysis, it is important to estimate a maximum value for the adjustment angle in the rotation axis of the driven roller.

The angle between the axes of the driven and the driving roller can be modified acting on the position of the hydraulic actuators.

Considering a starting scenario where there is no misalignment in the actuators and the provided F_F is equal to $80\ kN$, It follows a belt strain of about:

$$\epsilon = \frac{\sigma_t}{E} = 5.2\ 10^{-4}$$

that implies a total belt deformation of $\Delta L_t = 2.9$ mm.

The deformation of the straight portions of the belt should be of the order of magnitude of $\Delta L_\xi = \Delta L_t/2 \cong 1.5\ mm$.

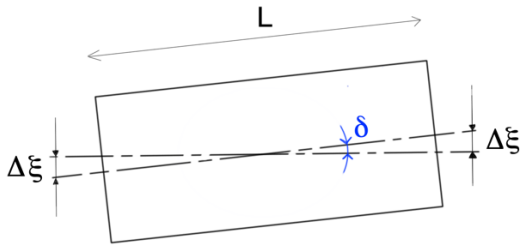

Fig. 2.5: Anti-symmetrical displacement correction

In the adjustment of the driven roller position, by supposing an anti-symmetrical correction displacement of the actuators as shown in *figure 2.5*, it is possible to evaluate a maximum adjustment angle of about

$$\delta_{max} = \text{arctg}\left(\frac{2\Delta L_{\xi max}}{L}\right) \simeq \frac{2\Delta L_{\xi max}}{L} = 0.37°$$

This angle implies a null belt stress in one side and a double stress on the other side.

In order to analyze the phenomenon of drifting among the belt and the rollers, a general configuration has to be considered. The figure 2.6 shows a top view of the belt-roller system when the rotation axis of the driven roller is slightly tilted by the angle δ and the steering angle of the tyre is α. The main forces acting on the system are reported.

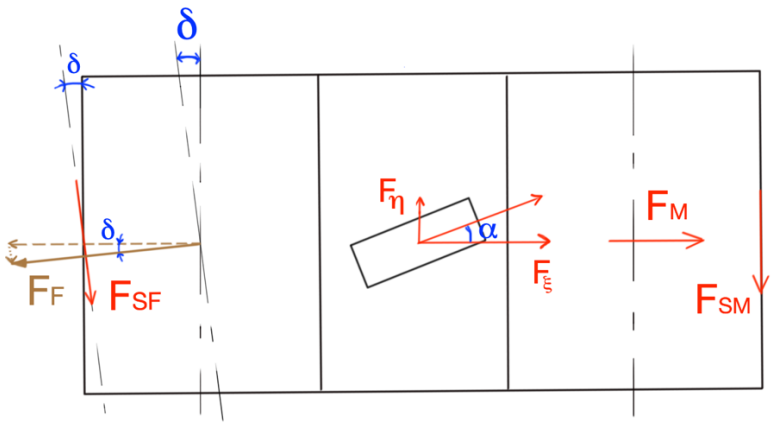

Fig. 2.6: Most relevant forces and angles from an above point of view

F_ξ and F_η are the forces exchanged between the tyre and the belt along the belt in the longitudinal and transversal direction, respectively. F_F and F_M represent the thrust forces of the actuators and the constraint force at the driving roller along the belt longitudinal direction, and F_{SF} and F_{SM} are the friction forces between rollers and belt along the transversal direction.

System dynamic equilibrium

$$F_\eta = F_{SM} + F_{SF}\ \cos\delta + F_F\ \sin\delta$$
$$F_\xi = F_F\ \cos\delta - F_M - F_{SF}\ \sin\delta$$

Being the angle δ lower than δ_{max} ($0.37° = 5.9\ mrad$) the previous relationship can be simplified in:

$$F_\eta \cong F_{SM} + F_{SF} + F_F\ \delta$$
$$\pm F_\xi \cong F_F\ - F_M - F_{SF}\ \delta$$

Thanks to the symmetry of the system, we can write:

$$F_{SM} \cong \frac{F_\eta}{2}$$
$$F_{SF} + F_F\ \delta \cong \frac{F_\eta}{2} \qquad (2.7)$$

The non-slipping condition along the transversal direction requires that:

$$F_{SM} \leq f_s\ F_M = f_s\left(F_F\ \mp\ F_\xi - F_{SF}\delta\right) \cong f_s\left(F_F\ \mp\ F_\xi\right)$$

(2.8)

$$F_{SF} \leq f_s \, F_F$$

By introducing *eqs.2.7* into the *inequalities 2.8* we obtain:

$$F_\eta \pm 2 \, f_s \, F_\xi \leq 2 \, f_s \, F_F$$

$$F_\eta \leq 2(f_s + \delta) \, F_F \tag{2.9}$$

These inequalities show that the effect of the tilt angle δ (5.9 10^{-3}) can be neglected with respect to the friction effect ($f_s \cong 0.1 \div 0.8$). Therefore, the belt has to be kept in position by guaranteeing a thrust force from the actuators that is big enough and the rotational axis of the driven roller in the correct position.

Thrust forces requested to the hydraulic actuators

In order to estimate the requested thrust forces, it is important to introduce the tyre load and its actions inside the equations. In *figure 2.7* the reference frame reporting the forces exchanged between the tyre and the belt is depicted.

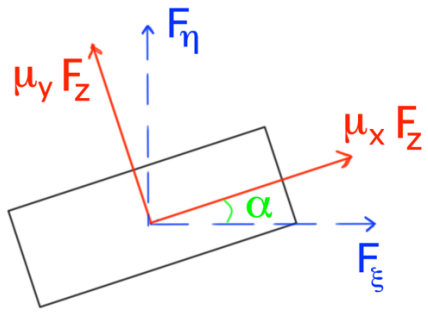

Fig. 2.7: Schematization of forces

The vertical tyre load F_z and the tyre steering angle α are related to F_ξ and F_η:

$$F_\xi = F_z \, (\mu_x \cos\alpha - \mu_y \sin\alpha)$$

$$F_\eta = F_z \, (\mu_y \cos\alpha + \mu_x \sin\alpha) \tag{2.10}$$

where μ_x and μ_y are the longitudinal and transversal tyre friction coefficients, respectively.

By introducing the *eqs.2.10* into *inequalities 2.9*:

$$F_F \geq \frac{F_z}{2(f_s + \delta)} (\mu_y \cos\alpha + \mu_x \sin\alpha)$$

$$F_F \geq \frac{F_z}{2f_s} (\mu_y \cos\alpha + \mu_x \sin\alpha) \pm F_z (\mu_x \cos\alpha - \mu_y \sin\alpha) \quad (2.11)$$

The following table reports the estimation of the minimum thrust forces that the hydraulic actuators have to provide. It is possible to notice that the chosen coefficients represent a worst scenario situation. In the working situation, the steering angle is generally lower than $15°$, the longitudinal and transversal tyre friction coefficients μ_x and μ_y are lower than the unity and the friction coefficient f_s might be close to 0.1 only if some water interposes among the steel belt and the rollers. In future, the latter condition will be prevented through the usage of an air journal bearing instead of the one with water.

α [°]	μ_x , μ_y	f_s	$F_{F_{min}}^{(1)}$	$F_{F_{min}}^{(2)}$
15	1	0.5	2 F_z	2 F_z
15	1.5	0.5	3 F_z	3 F_z
15	1	0.1	5 F_z	7 F_z
15	1.5	0.1	8 F_z	9 F_z

(1) Imposed by the tangential adherence: *inequalities (2.5) and (2.6)*
(2) Imposed by the transversal adherence: *inequality (2.11)*

Tab. 2.1: Resume of the thrust forces F_F requested to the actuators

These data evidence that in order to guarantee the tangential and transversal adherence between the belt and the rollers, it is required that the hydraulic actuators provide a total thrust force:

- belt-roller dray contact

$$F_F \cong 3\, F_Z$$

- belt-roller wet contact

$$F_F \cong 9\, F_Z$$

In our TTB the vertical load F_z is limited to $10\ kN$. Therefore, by applying a thrust force F_F greater than $90\ kN$ it is possible to satisfy both the requirements imposed by the adherence if the belt-roller contact is wet. Instead, when the belt-roller contact is dry a thrust force of only $30\ kN$ is required.
These values of the thrust force are in accordance to the maximum thrust force previously estimated in the belt stress analysis section.

In conclusion, by applying a total thrust force F_F in the range $50\ kN \div 80\ kN$ it is possible to guarantee the adhesion and prevent an excessive deformation of the steel belt.

Chapter 3

Mathematical and Simulink models

The tyre test bench represents the physical system that we have to analyze and check in order to be able to carry out experimental tests on the tyre.
In order to design a control system for the TTB it is necessary to describe its behavior in the form of mathematical relationships. The following chapter analyzes the driven roller actuation system, in particular, it is dedicated to the description of the steel belt motion and the hydraulic actuators.
Considering the steel belt, this is described and modeled with regard to the forces exchanged with the roller and its lateral translation speed, while the description and modeling of the hydraulic actuators is based on the datasheets of the hydraulic piston and the control valve.

3.1 Forces exchanged between rollers and belt

The *figure 3.1* depicts the driven roller in two characteristic positions: a) when the actuators are moving and the belt is not fully in contact to the roller, and b) when the roller and belt are fully in contact and the belt is pulled.

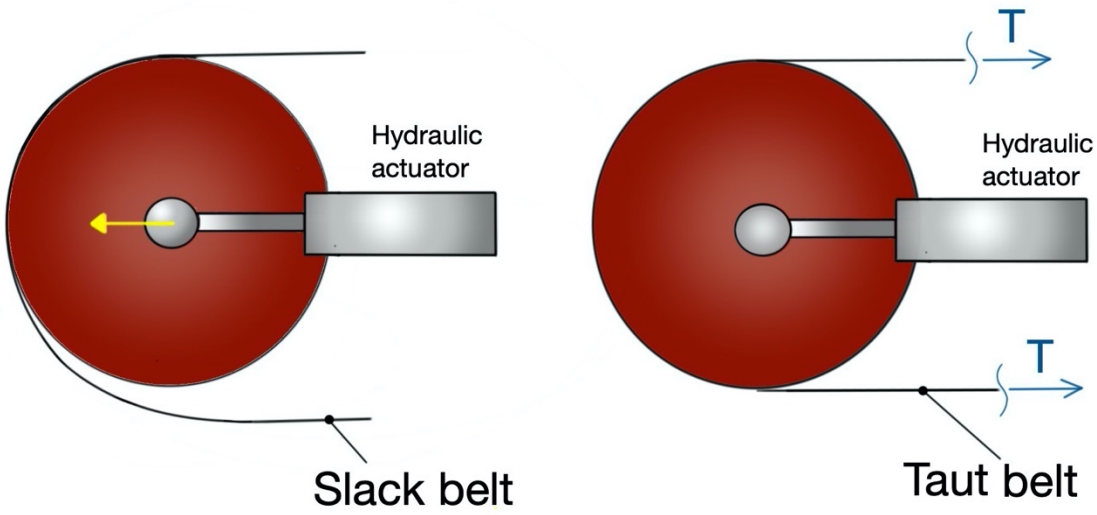

Fig. 3.1: Belt shape before and after tensioning

In the following the belt is modelled as an infinite number of infinitesimal springs connected in parallel. Each spring represents the stiffness imposed by a slice of amplitude $d\xi$, of the belt.

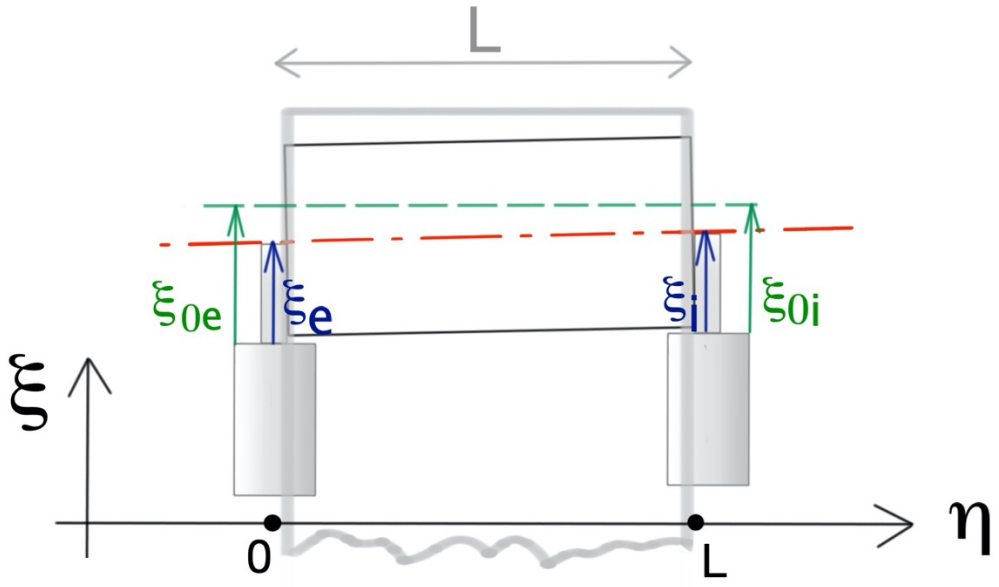

Fig. 3.2: Driven roller and belt seen from above

The *figure 3.2* sketches the belt-driven roller system and the actuators. The positions of the pistons of the external and internal hydraulic actuators are ξ_e , ξ_i, respectively,

while the positions at which the steel belt starts to be taut are ξ_{0e} , ξ_{0i} thus providing a reaction force.

The position of the driven roller along the transversal coordinate η are:

$$\xi(\eta) = \xi_e + \frac{\xi_i - \xi_e}{L}\,\eta$$

The infinitesimal stiffness moving along the transversal position of a quantity $d\eta$ is:

$$dK = \frac{E\,t}{l}\,d\eta$$

where:

- *E:* Young Modulus of belt steel;
- *t:* thickness of the belt;
- l*:* longitudinal length of the straight part of the belt.

Then it is possible to evaluate the infinitesimal force exchanged at a general transversal position as:

$$dF(\eta) = dK\,[\xi(\eta) - \xi_0(\eta)] = \frac{E\,t}{l}\,[\xi(\eta) - \xi_0(\eta)]\,d\eta$$

where:

$$\xi_0(\eta) = \xi_{0e} + \frac{\xi_{0i} - \xi_{0e}}{L}\,\eta$$

Considering the balance of forces and momentum, it is possible to analytically express the forces required by the hydraulic actuators as:

$$F_e = \frac{E\,t}{l}\left[\frac{\xi_e - \xi_{0e}}{3} + \frac{\xi_i - \xi_{0i}}{6}\right]L \qquad (3.1)$$

$$F_i = \frac{E\,t}{l}\left[\frac{\xi_e - \xi_{0e}}{6} + \frac{\xi_i - \xi_{0i}}{3}\right]L \qquad (3.2)$$

where L is the transversal width of the belt.

According to the obtained *eq. 3.1* and *eq. 3.2,* the *Simulink* model of *figure 3.3* has been generated. It provides the reactions force provided by the steel belt to the extremities of the driven roller, i.e. to the hydraulic actuators.

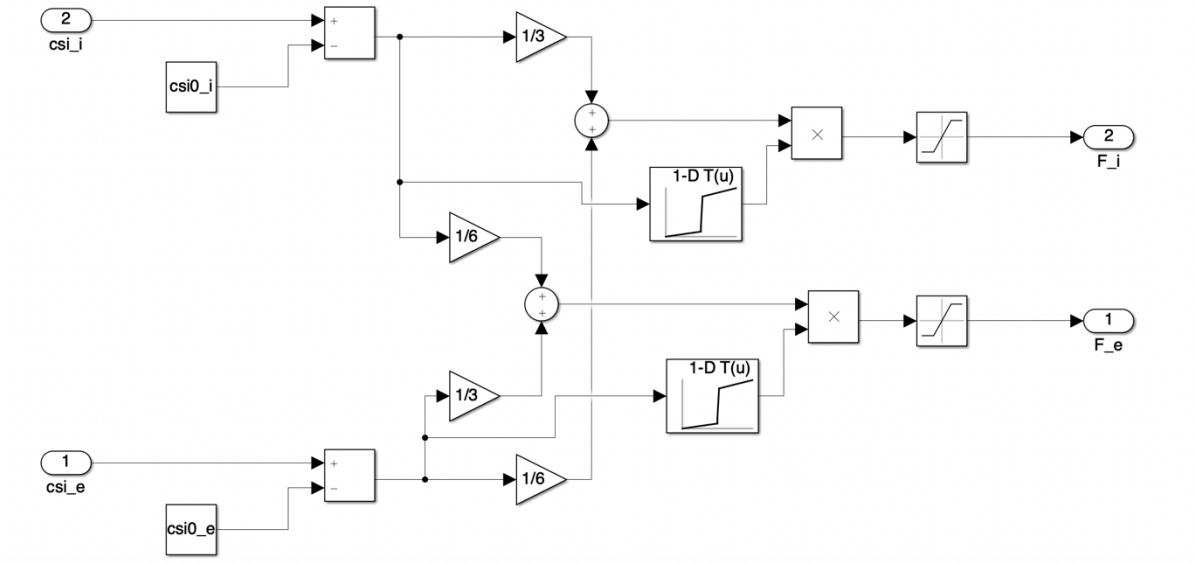

Fig. 3.3: Simulink model of the reaction forces provided by the belt to the hydraulic actuators

The lookup tables are used to represent the winding of the belt around the driven roller. An experimental data analysis allows to estimate the stiffness provided by the belt with respect to the internal/external side of the driven roller.

3.2 Transversal drifting of the belt

When the steel belt is rotating around the rollers, it might drift along the transversal direction (η). This translation is due to the misalignment in the rotation axes of the rollers and eventually to an excessive transversal force provided by the tyre. The *figure 3.4a* and *3.4b* depicts the scenario from an above and later point of view. The *figure 3.4c* sketches the drifting of the belt in case of unparallel rotation axes.

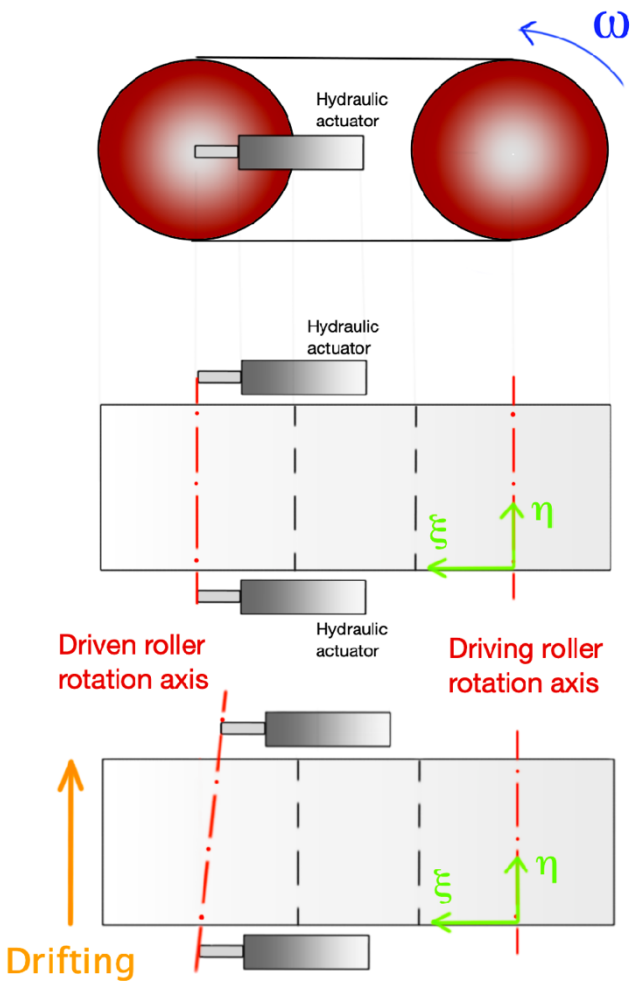

Fig. 3.4: Schematization of the framework

Supposing the adherence condition between the belt and the rollers, the phenomenon can be modeled as a belt winding around the driven roller. Referring to *figure 3.4*, it is possible to state that

$$d\eta = k \frac{\Delta\xi}{L} R \, d\vartheta$$

where:

- $d\eta$: infinitesimal drifting along the transversal direction
- R : radius of the driven roller
- $\Delta\xi$: misalignment between the pistons of the hydraulic actuators
- L : total longitudinal length of the steel belt
- $d\vartheta$: infinitesimal angle of rotation of the driven roller
- k: experimental coefficient

The above relationship can be derived with respect to the time in order to describe the drifting speed of the belt

$$\dot{\eta} = k\,\Delta\xi\,\frac{R}{L}\,\omega \tag{3.3}$$

The *eq. 2.16* is the mathematical model of the drifting velocity of the belt as a function of to the roller rotation speed ω and the misalignment in the positions of hydraulic actuators $\Delta\xi$. Acting on the misalignment $\Delta\xi$ it is possible to obtain the parallelism of the rotation axes of the rollers and control the belt transversal position.

The *figure 3.5* shows the *Simulink* model implemented for the belt. In particular, the model is able to describe the belt tensioning (*eq. 3.1* and *eq. 3.2*) and the drifting of the steel belt with respect to the rollers (*eq. 3.3*).

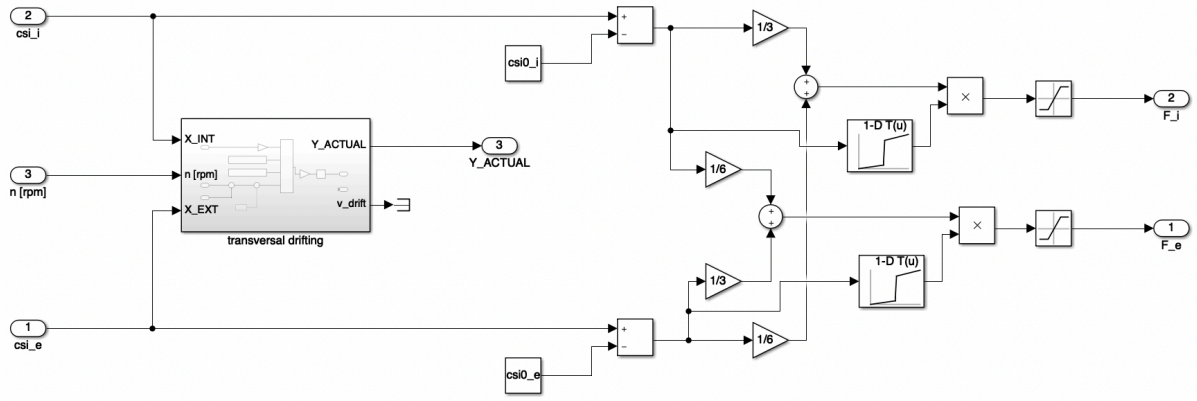

Fig. 3.5a: Simulink model of the belt-roller exchanged forces

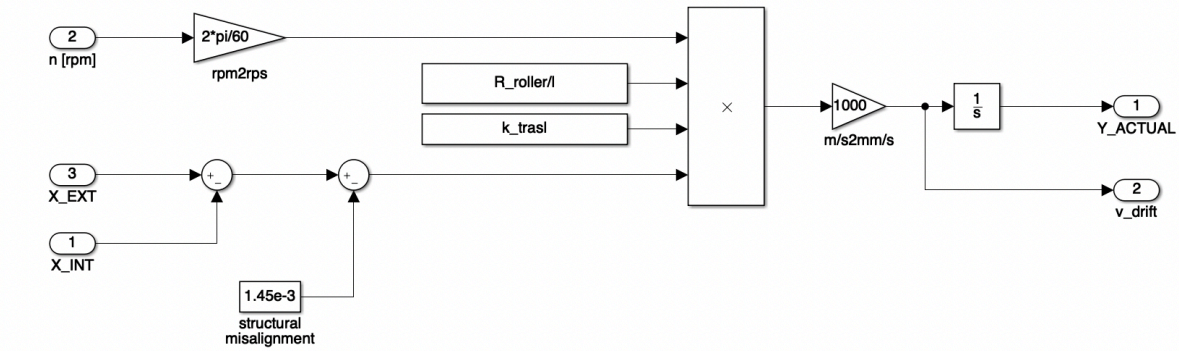

Fig.3.5b: Simulink model of the belt transversal drifting

3.3 Hydraulic model of the actuation system

The actuation system of the driven roller, sketched in *figure 3.6*, presents two hydraulic actuators. The actuation system is responsible of guaranteeing the desired tightness of the steel belt and the centering of the latter one with respect to the rollers. Therefore, the hydraulic actuators carry out a fundamental role and being able to control their extraction position, it is possible to set a precise position and inclination of the driven roller's rotation axis. The latter possibility allows to impose the desired belt tightness and prevent the sliding of the belt along the longitudinal and transversal directions.

The position controller for the hydraulic actuator is developed in the relative chapter, the following paragraph is dedicated to its mathematical description.

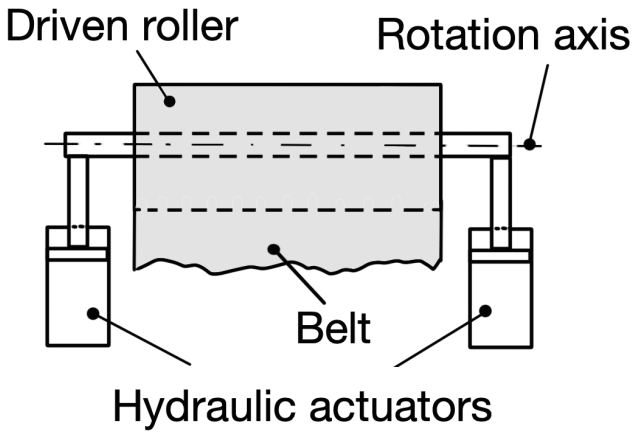

Fig. 3.6: Actuation system of the driven roller

The hydraulic actuators are felt by hydraulic oil whose flow is controlled by a directional proportional valve. According to the excitation signal of the valve, it is possible to extract or retract the piston. The *figure 3.7* shows a simplification of the hydraulic circuit that is employed for the actuator movement.

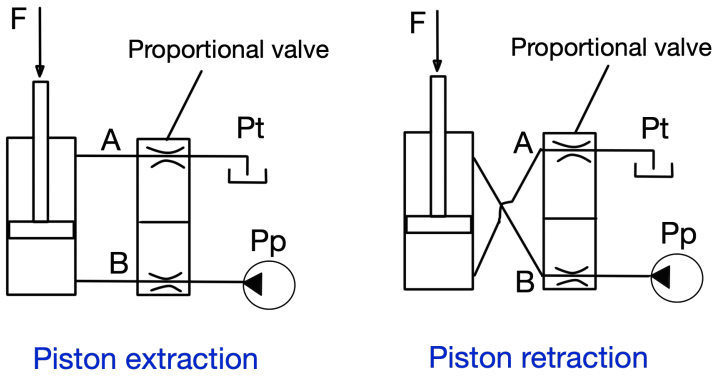

Fig. 3.7: Simplification of the hydraulic circuit

Hydraulic piston

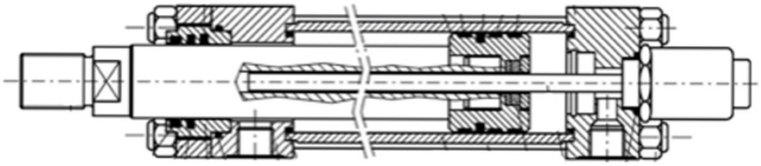

Fig. 3.8: Section of the hydraulic piston

The figure 3.8 reports a cross section of the hydraulic actuator employed in the TTB [9]. They show a cylinder diameter of $D = 80\ mm$ with a stem diameter of $D_{steam} = 36\ mm$. It follows a net surface of $50\ cm^2$ in the thrust direction and of $40\ cm^2$ in the retraction direction. This difference in the net surfaces causes the different flow rates flowing in/out the piston chambers.

The mechanical behavior of the hydraulic piston can be modelled as a second order system

$$F_0 + m\frac{dv}{dt} + \beta v = p_{up}S_{up} - p_{dw}S_{dw} - \frac{v}{|v|}F_a \pm R_v \qquad (3.4)$$

where the following terms appear:

- pressure in the up-side chamber P_{up}
- pressure in the down-side chamber P_{dw}

- force coming from the belt reaction F_0
- damping coefficient β
- half mass of the driven roller m
- velocity of the piston v
- static and dynamic friction F_a

$$F_a = \begin{cases} F_{up} - F_{dw} - F_0 \ , & v = 0 \\ F_d \ , & v \neq 0 \end{cases} \tag{3.5}$$

- constraint reaction due to the piston geometry R_v

The positive direction of motion of the piston is assumed in accordance to the extraction direction of the piston.

A simple schematization of the piston extraction is reported in *figure 3.9*.

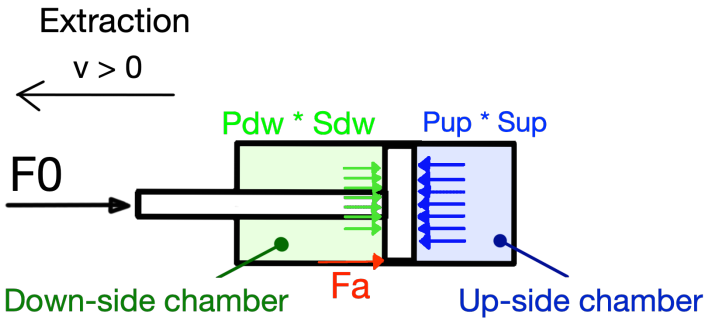

Fig. 3.9: Schematization of the forces acting in the hydraulic piston

Hydraulic circuit

The up-side and down-side piston chambers of the piston are modelled considering the oil compressibility and the presence of air trapped into it. These considerations lead to the utilization of an effective bulk modulus of the oil that depends on the pressure inside the chambers.

To derive a model of the pressure variation inside the chambers of the piston, the continuity equation is written:

$$Q_{up} = S_{up}\, v + \frac{V_{up}}{E} \frac{dp_{up}}{dt} \tag{3.6}$$

$$S_{dw}\, v + Q_{dw} = \frac{V_{dw}}{E} \frac{dp_{dw}}{dt} \tag{3.7}$$

where Q_{up} and Q_{dw} are the volumetric flowrates flowing into the up chamber and flowing out the downstream chamber, respectively.

The bulk modulus E of the oil is the one computed by considering that a percentage of entrained air is present [10]. This consideration lead to a model that consider an effective bulk modulus through the following equation:

$$E_{\mathrm{ef}} = \frac{(1-\alpha)\cdot\left(1+\frac{m\cdot(p-p_0)}{E_0}\right)^{-\frac{1}{m}} + \alpha\cdot\left(\frac{p_0}{p}\right)^{\frac{1}{\kappa}}}{\frac{1}{E_0}\cdot(1-\alpha)\cdot\left(1+\frac{m\cdot(p-p_0)}{E_0}\right)^{-\frac{m+1}{m}} + \frac{\alpha}{\kappa\cdot p_0}\cdot\left(\frac{p_0}{p}\right)^{\frac{\kappa+1}{\kappa}}} \tag{3.8}$$

where:

- E_0 is the reference bulk modulus of air free oil
- α is the volumetric content of entrained air at initial pressure
- m is the pressure related term in the bulk modulus of oil
- p_0 is the reference pressure
- k is the polytropic index

Directional proportional valve

The directional proportional valve [11], *figure 3.10*, is able to impose a flow rate whose quantity and direction depends on the provided electrical command signal. In particular, it receives as input command signal a bipolar voltage in the range of $\pm 10\ V$. According to the sign of the command signal, it is possible to impose the direction of the piston motion at a velocity that is proportional to the amplitude of the command itself. The model of the valve is represented by a couple of adjustable turbulent nozzles whose cross-sectional area depends on the command signal. The nozzles connect the output of the valve (A and B) to the sources p_p (oil at the pressure imposed by the hydraulic pump) and p_t (oil at ambient pressure).

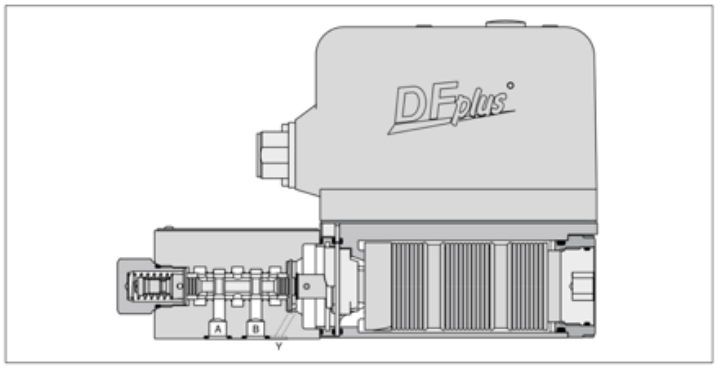

Fig. 3.10: Directional proportional valve

Starting from the datasheet of the valve it is possible to model the static and dynamic behavior.

Static Behavior

The static characteristic of the proportional valve is extracted from the datasheet and reported in *figure 3.11*. It represents the flow rate passing through the nozzles according to the excitation command. The abscissa was normalized with respect to the maximum excitation value of $10\ V$, while the flow rate has been normalized with respect to the nominal value Q_n $(25\ l/min)$.

The nominal flow rate has been obtained considering a pressure drop across the orifice of $\Delta p_{35} = 35\ bar$.

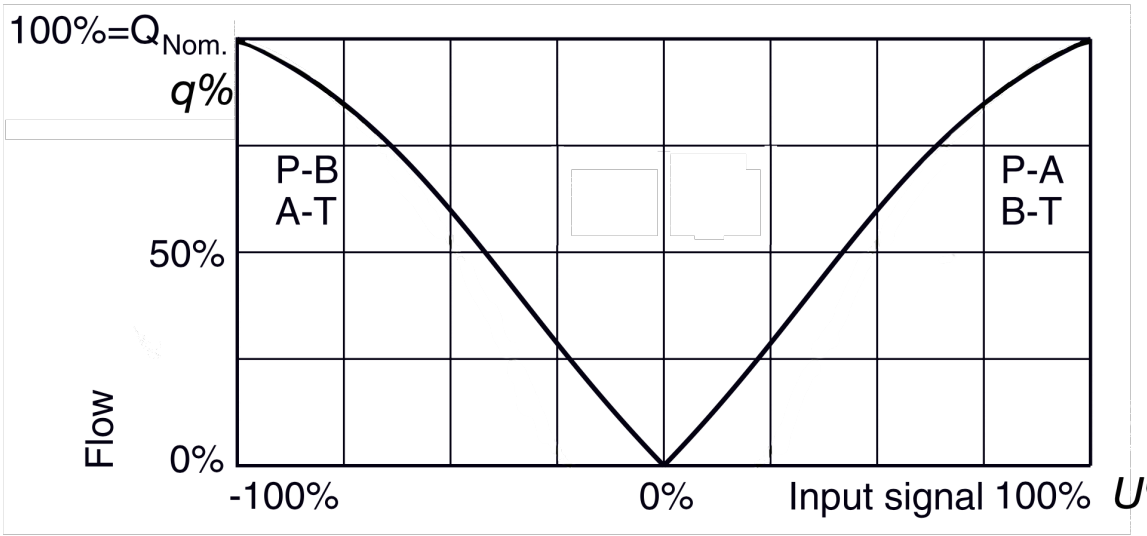

Fig. 3.11: Percentage of flow rate according to the percentage of input signal

The effective flow rate passing through the orifice undergoing a pressure drop Δp can be obtained as

$$Q = q_{\%} Q_n \sqrt{\frac{\Delta p}{\Delta p_{35}}} \tag{3.9}$$

The pressure drops Δp across the orifices of the valve are not equal because of the different incoming and outcoming flow rates in the piston. This follows the different section of the upstream and downstream piston chambers.
Another important characteristic of the valve is related to the effective pressure drop in the orifices when the control signal is approaching to zero. During this phase the sled position is inaccurate and a portion of the oil coming from the hydraulic pump goes directly in the ambient shortcutting the piston. The sketch below represents the phenomenon in case of command signal approaching zero from the positive side.

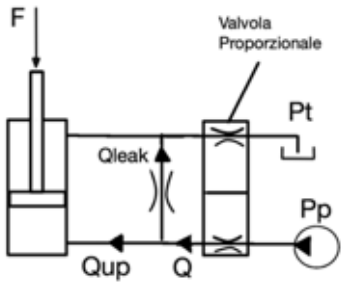

Fig. 3.12: Leakages due to zero crossing

The leakages are modeled by means of a laminar nozzle shortcutting the piston inlet and outlet.

Dynamic behavior

The dynamic of the valve can be analyzed considering the magnitude bode plot (*figure 3.13*) that is reported in the datasheet.

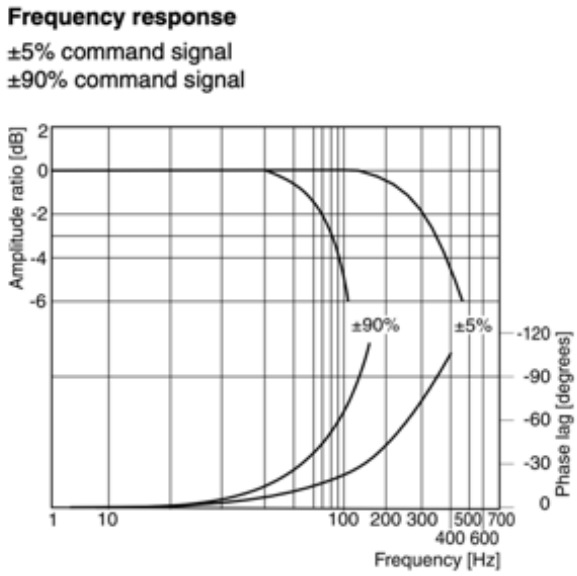

Fig. 3.13: Bode plot of the flow rate with respect to the command signal

The valve's dynamic can be approximated as a first order low pass filter whose cut-off frequency ($-3\ dB$) depends on the amplitude of the input command signal. The cut-off frequency f_c ranges between $80\ Hz$ to $350\ Hz$. The model simplifies the characteristic considering the worst-case scenario ($f_c = 80\ Hz$), even if during the control phase is likely to deal with small amplitude variation in the control signal.

3.4 Simulink model of the hydraulic actuator

The model of the hydraulic actuator is reported in *figure 3.14*. It is characterized by four main blocks:

- Mechanical system: models the dynamical behavior of the piston
- Up/Down piston chambers: represent the pressure variation inside the piston chambers. "*Q > 0 (in)*" means that the oil flow rate is considered positive when incoming in the chambers of the piston.
- Proportional valve: represents the behavior of the directional proportional valve.

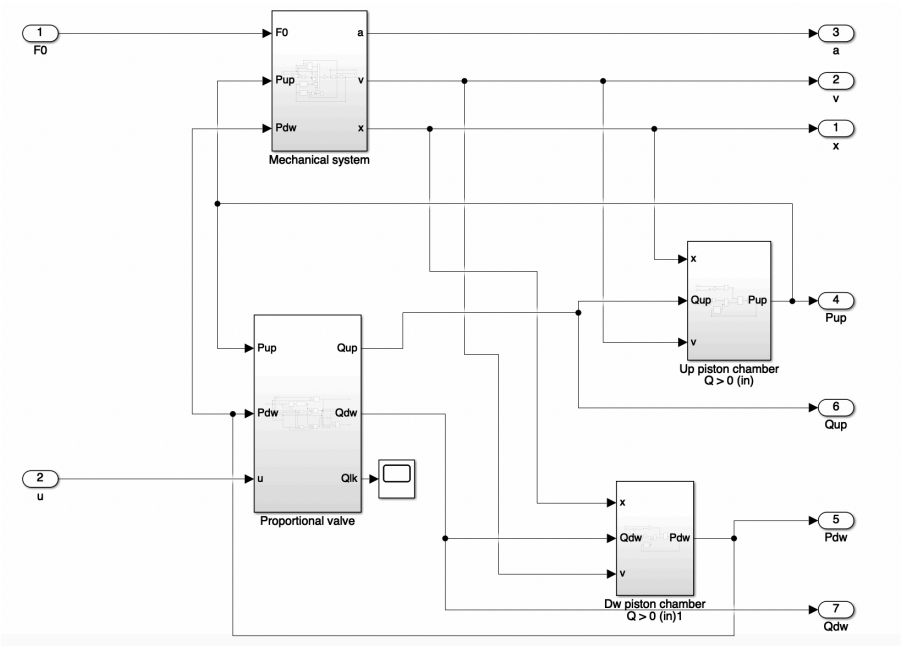

Fig. 3.14: Simulink model of the hydraulic actuator

The model receives as input the reaction force provided by the steel belt F_0 and the input command signal u. The outputs of the model are the parameters that are considered of interest. These last are analysed singularly as the outputs of the main blocks composing the hydraulic actuator.

Mechanical system

The model of the mechanical system (*figure 3.15*) describes the dynamic of the hydraulic piston. It has been generated as the implementation of the mathematical *eq. 3.5* inside the *Laplace* domain.

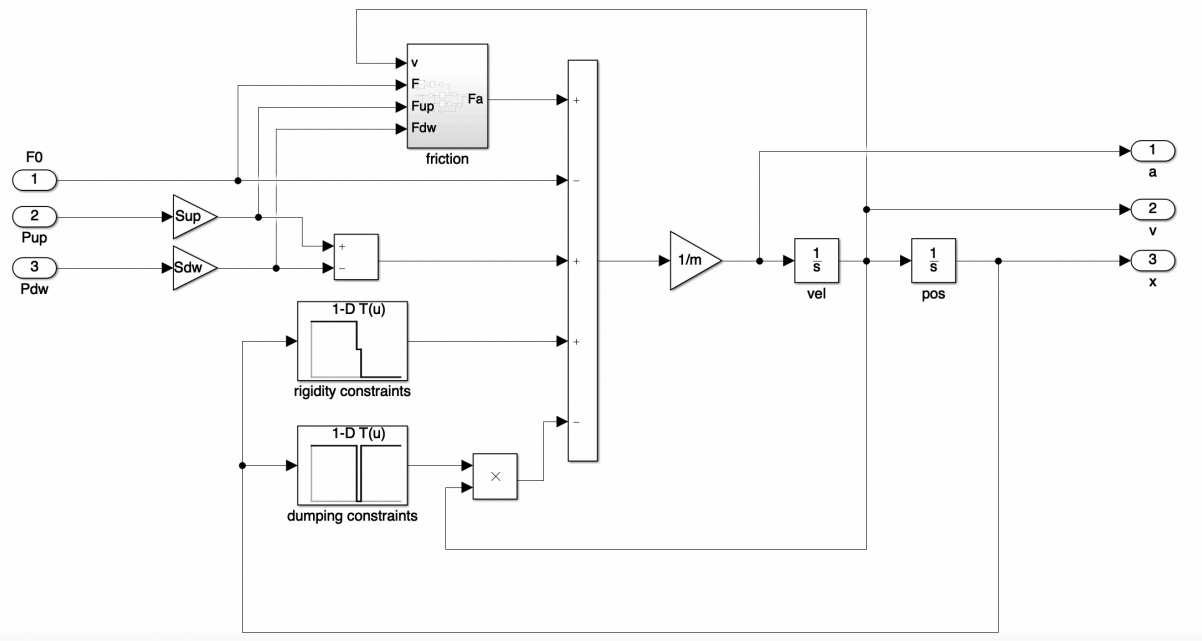

Fig. 3.15: Simulink model of the hydraulic piston

INPUT

- F: force coming from the belt reaction (F_0)
- P_{up} and P_{dw}: pressures in the up-side and down-side chambers

OUTPUT

- x: piston position
- v: piston velocity (positive in the extraction phase)
- a: piston acceleration

Where:

- *Rigidity constraints:* represent the piston side walls constraints.
- *Fa:* represents the friction inside the cylinder (*eq. 3.4*). Until the resultant of the active forces do not overcome the maximum static friction reaction (represented through the saturation block based on $F_{a_{max}}$), the piston remains still. When the above condition is no more verified, the piston starts moving and the friction switches from static to dynamic. The switching transition from F_a to F_d occurs when the piston velocity falls between a range of ($0.9 \div 1.1$) mm/s. This phenomenon is modeled through the sigmoidal functions *f1_a* and *f2_a*.

The Simulink model for friction is reported in *figure 3.16*

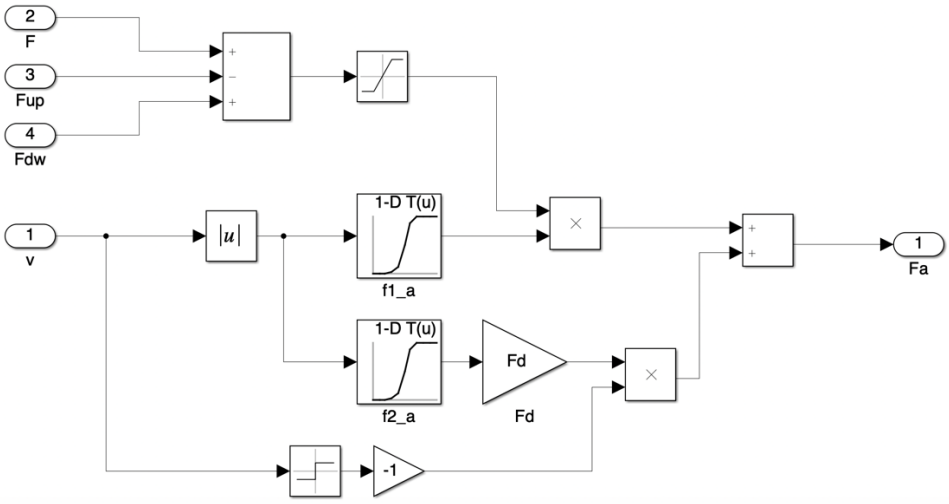

Fig. 3.16: Simulink model of friction

Up/Down piston chambers

The Simulink model of the chambers of the piston is the implementation of the continuity equations (*eq. 3.6* and *eq. 3.7*). The effective bulk modulus is calculated as shown in *eq. 3.8* and implemented through the lookup table.

The *figures 3.17* and *3.18* report the realized Simulink model of the up-side and down-side piston chambers respectively.

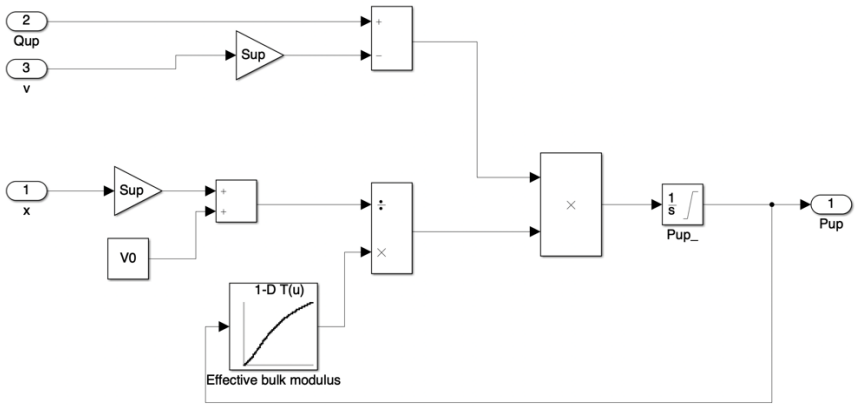

Fig. 3.17: Simulink model of the upstream chamber inside the piston

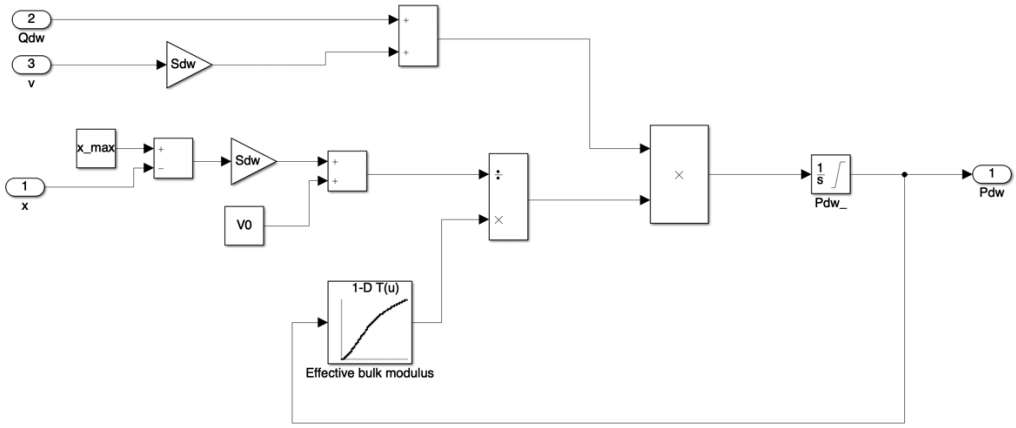

Fig. 3.18: Simulink model of the downstream chamber inside the piston

Proportional valve

The model of the directional proportional valve (*figure 3.19*) takes care of the computation of the oil flow rates that are exchanged with the piston starting from the excitation command signal and the pressures inside the piston chambers.

The model computes the percentage of flow rate $q_{\%}$ using a lookup table that represents the characteristic shown in *figure 3.11* and a first order low pass filter with a cut-off frequency of $80\ Hz$ that simulate the dynamic behavior obtained from the bode plot of *figure 3.13*.

The logic is realized according to the sign of the input command signal and recalling that the oil flow rate is considered positive when outcoming from the valve, i.e. when incoming in the piston chamber.

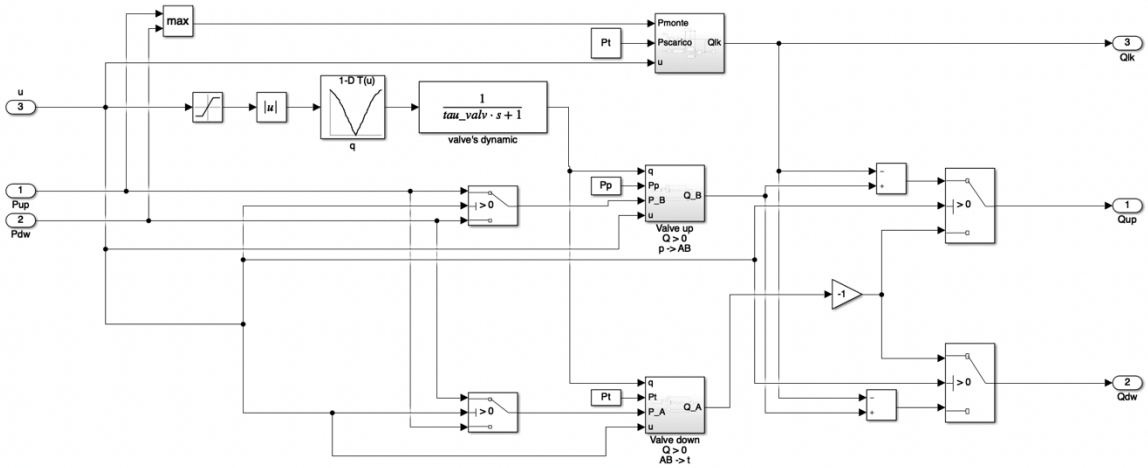

Fig. 3.19: Simulink model of the proportional valve

INPUT

- u: excitation command signal
- P_{up}: pressure in the up-side chamber of the piston
- P_{dw}: pressure in the down-side chamber of the piston

OUTPUT

- Q_{up}: volumetric oil flow rate incoming the up-side chamber of the piston
- Q_{dw}: volumetric oil flow rate incoming the down-side chamber of the piston
- Q_{lk}: represents the leakages

The Simulink blocks *valve Up* and *valve Down* in figure 3.19 are built in accordance to the *eq. 3.9* and consider also the asymmetry inside the valve that are experimentally evidenced.

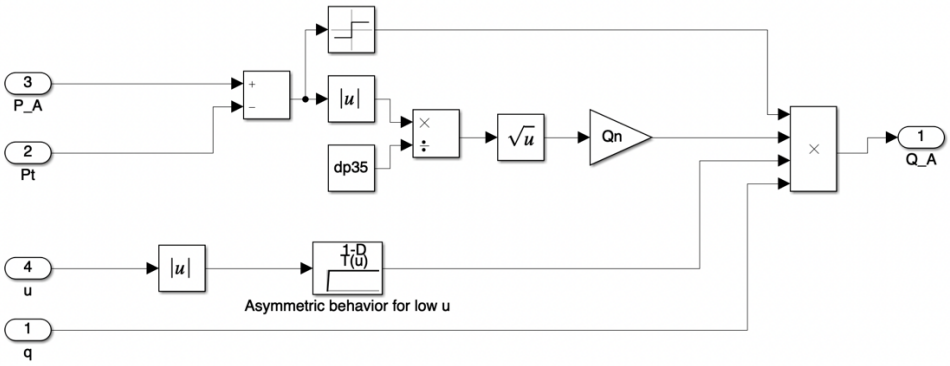

Fig. 3.20: Simulink model of the valves inside the proportional valve

Chapter 4

Experimental analysis and model validation

The following chapter aims to show some of the activities carried out with the TTB. Specifically, the experimental activities aimed at refining and validating the models created are reported and analyzed.

4.1 Experimental validation of the hydraulic actuators

In order to verify the model of the hydraulic actuators, a basic experimental test has been conducted. Providing a constant excitation command to both the actuators it is possible to analyze the extraction and retraction phases of the pistons.
The tyre test bench allows to measure the positions of the pistons and the pressure inside the up-stream and down-stream chambers of both the hydraulic actuators. In the *figures 4.1* and *4.2* are shown the measured trends obtained by the application of an input command signal U of different amplitudes.

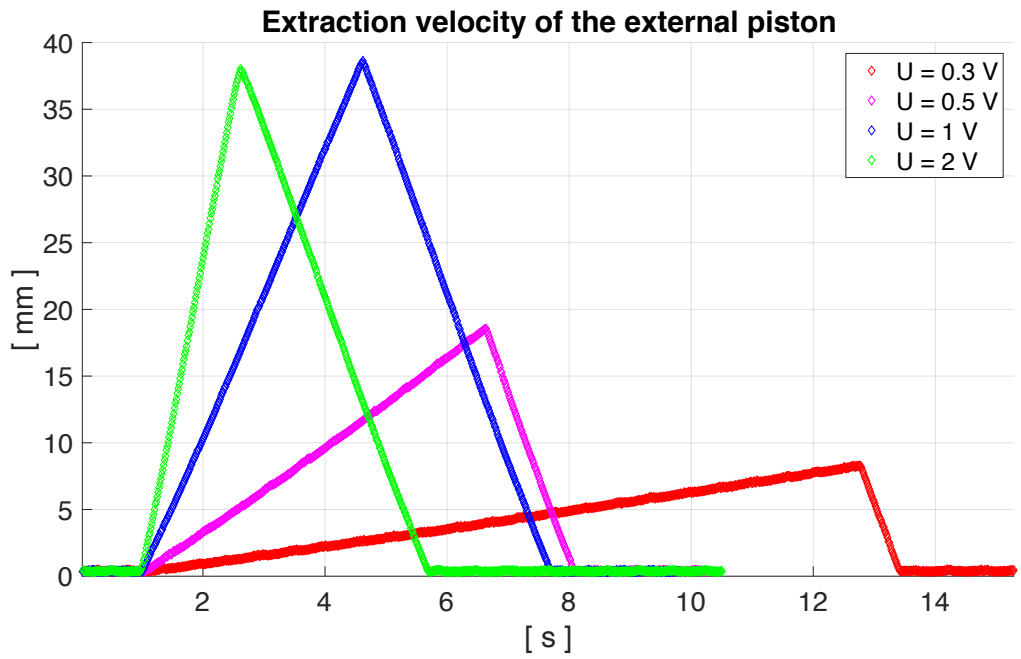

Fig. 4.1: extraction velocity of the external actuator with respect to U

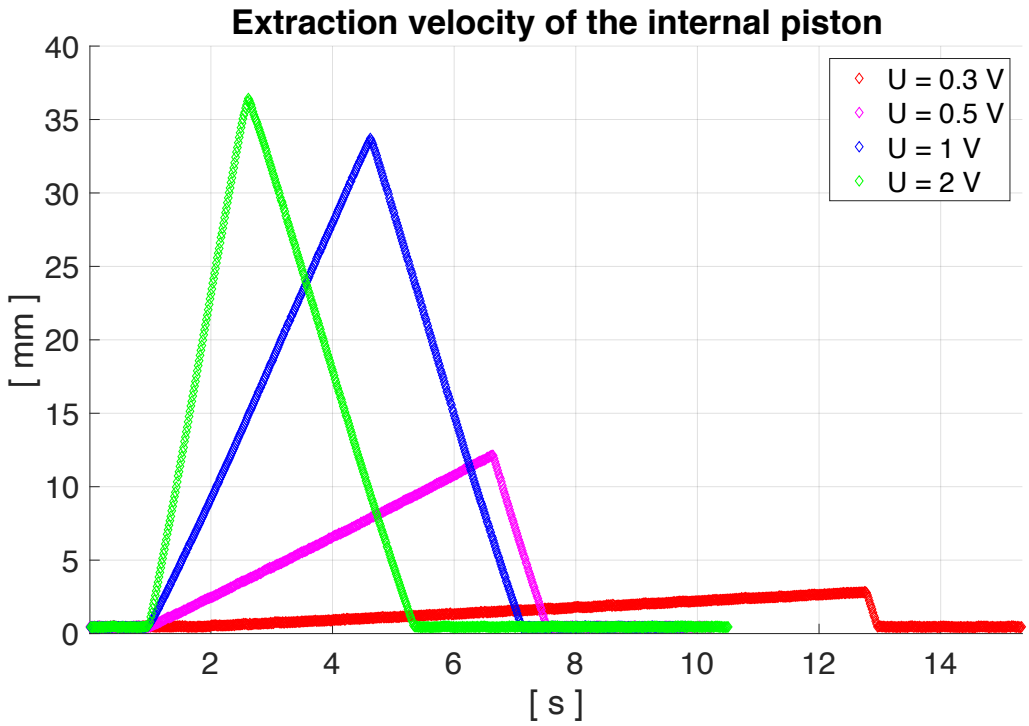

Fig. 4.2: extraction velocity of the internal actuator with respect to U

From the measurements of the positions of the pistons it is possible to estimate the extraction velocities. The *tab. 4.1* reports the amplitude of the provided constant input

U and the estimation of the extraction velocities starting from the measurements of the positions.

U [%]	*U [V]*	*External extraction velocity [mm/s]*	*Internal extraction velocity [mm/s]*
1	*0.1*	*-*	*-*
3	*0.3*	*0.68*	*0.22*
5	*0.5*	*3.28*	*2.07*
10	*1*	*10.7*	*9.19*
20	*2*	*24.1*	*23.0*

Tab. 4.1: Extraction velocities of the actuators according to the command signal

The *figures 4.1* and *4.2* do not show the positions of the pistons for the first case where $U = 0.1\,V$ because there were no motions.

The pistons are extracted thanks to the establishment of certain pressures within the cylinder chambers. Since the dimensions of the chamber sections are known, it is possible to calculate the thrust forces produced by the actuators.
In order to be able to fully characterize the hydraulic actuators, *figure 4.3* and *4.4* show the pressures gauged inside the cylinder chambers in the case of $U = 0.5\,V$.

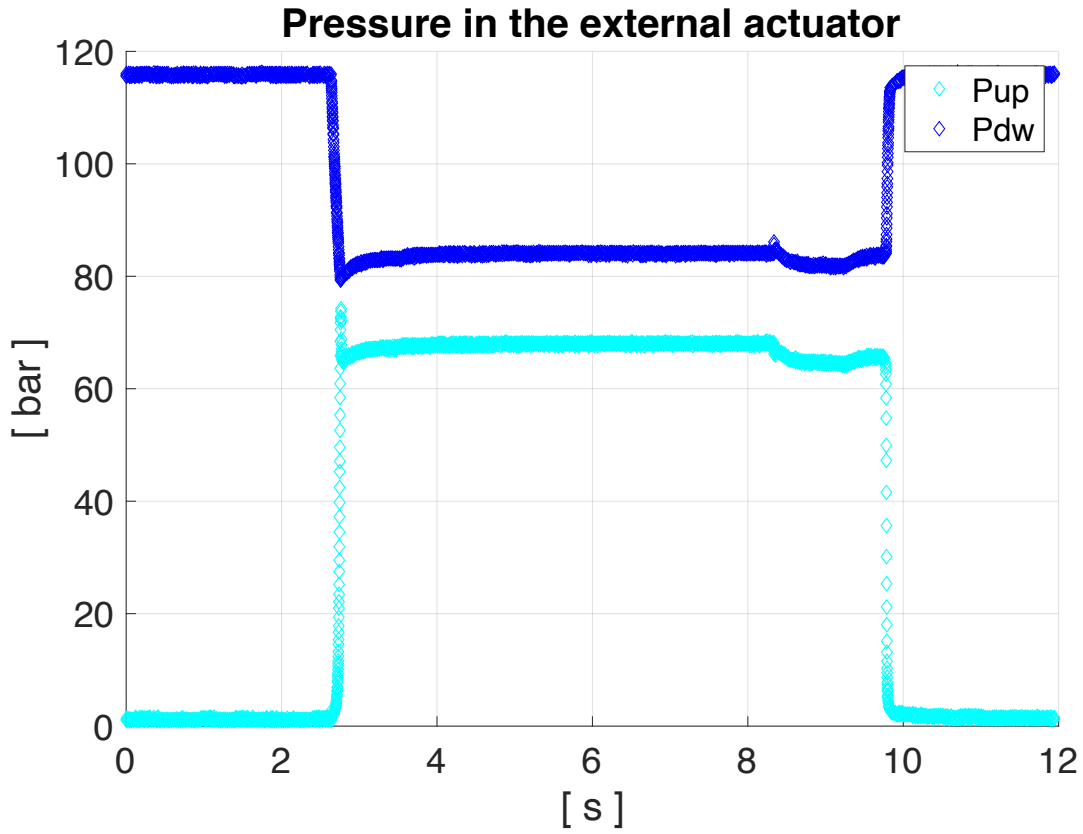

Fig. 4.3: Up-stream and down-stream pressures in the cylinder of the external actuator for $U = 0.5\,V$

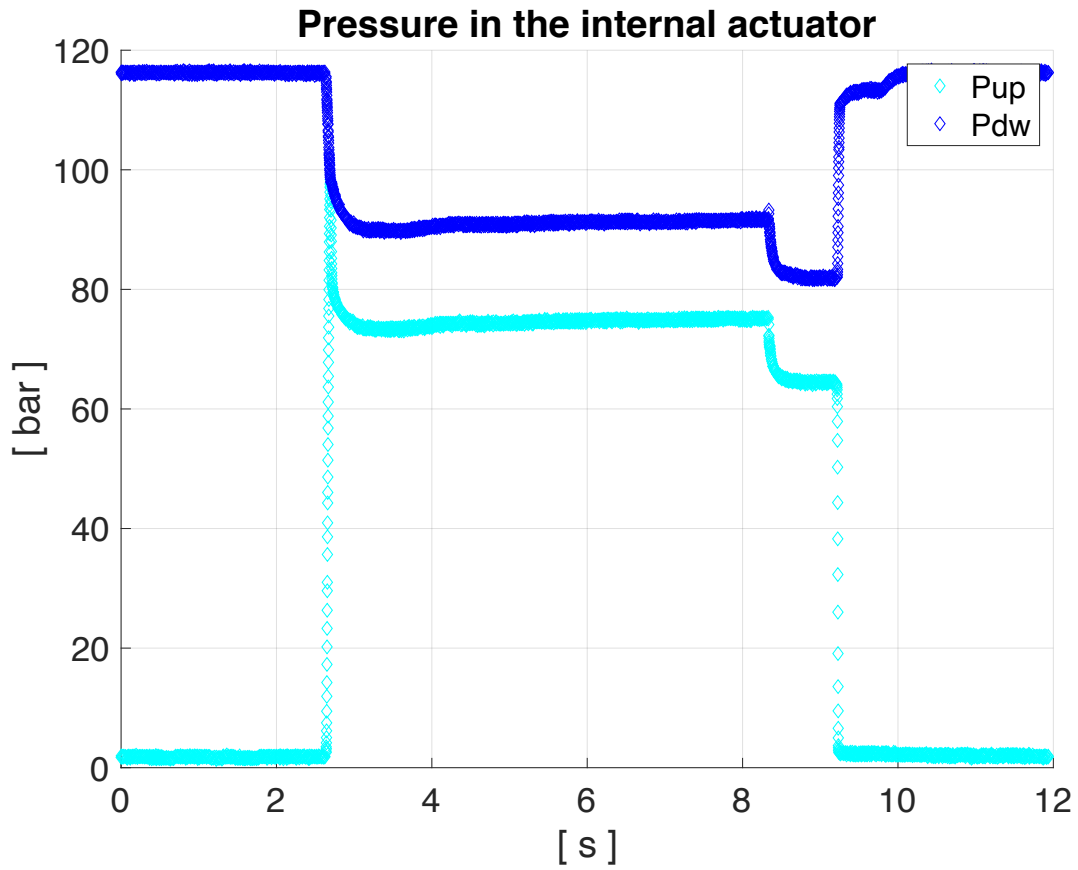

Fig. 4.4: Up-stream and down-stream pressures in the cylinder of the internal actuator for $U = 0.5\,V$

Model validation and parameters estimation of the hydraulic actuators

After carrying out the experimental activity described in the previous paragraph, it was possible to refine and validate the model of the hydraulic actuators.
Specifically, the tests conducted on the TTB were also conducted through the model in order to analyze and minimize the differences in behavior between the two.

Starting from the results reported in *tab. 4.1*, it is possible to notice that both the actuators are not able to move until the command signal exceeds a certain threshold. It is also possible to observe that the extraction velocities of the actuators are different, but they become similar for increasing amplitude values of the command signal U. These phenomena are attributable to the presence of an offset inside the effective static characteristic of the proportional valve (*figure 3.11*). It is plausible that

the position of the sled inside the proportional valve is less accurate when the command signal U is close to zero.

Starting from the measurements, an estimation of the offset has been calculated for both the actuators and the model of the proportional valve has been modified. In particular, the lookup table emulating the static characteristic has been revised in accordance to the experimental analysis.

After having refined the static characteristic of the proportional valves by bringing the knowledge on the offsets, the model of the actuators and the position measurements made on the TTB are compared in *figures 4.5* and *4.6*.

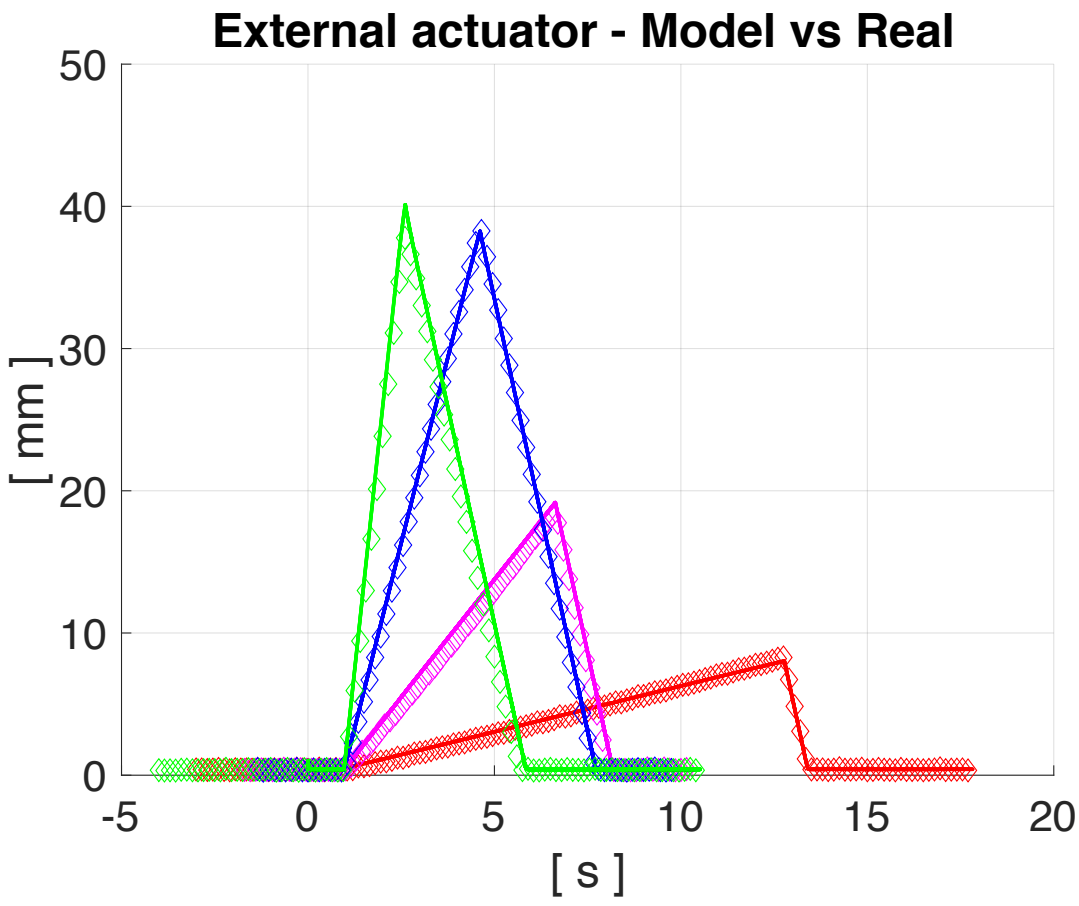

Fig. 4.5: Model comparison in the extraction velocity of the external piston

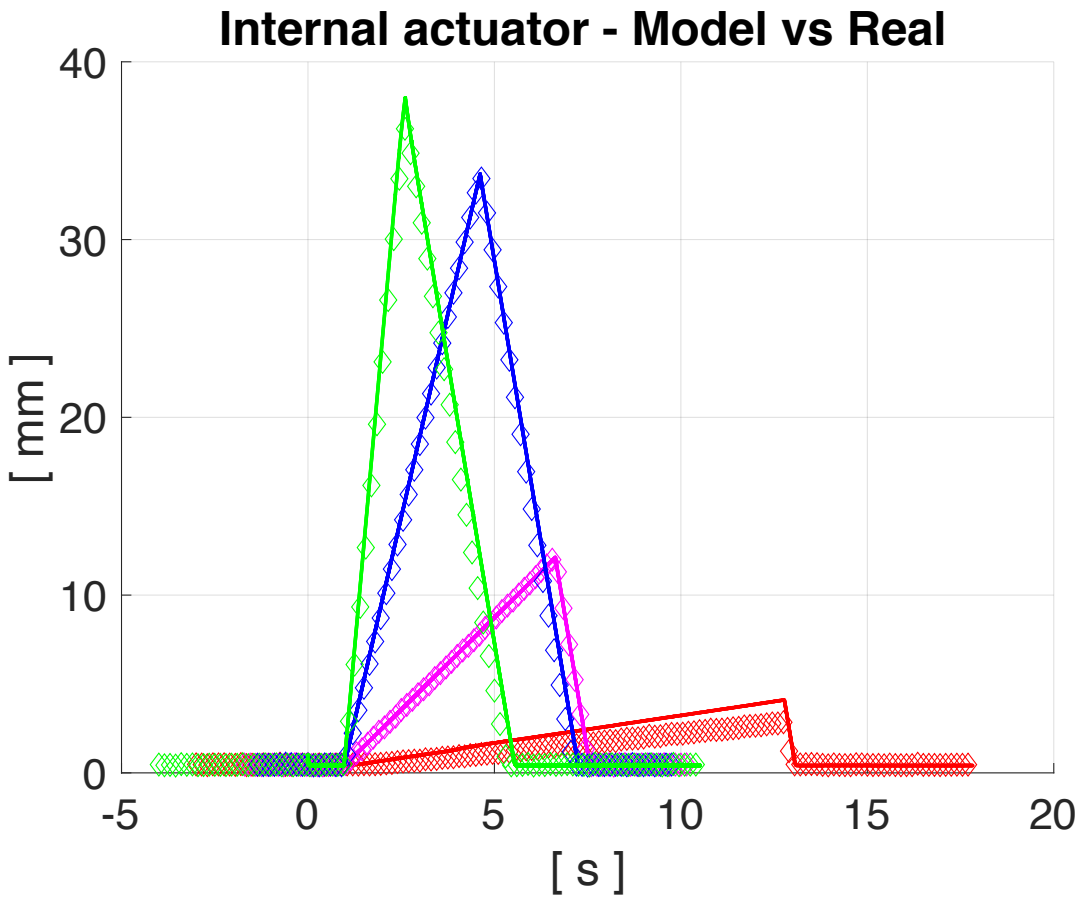

Fig. 4.6: Model comparison in the extraction velocity of the internal piston.

The estimation of the velocities of extraction is reported inside *tab. 4.2*.

U [%]	*U [V]*	*External extraction velocity [mm/s]*	*External extraction velocity MODEL [mm/s]*	*Internal extraction velocity [mm/s]*	*Internal extraction velocity MODEL [mm/s]*
1	*0.1*	-	-	-	-
3	*0.3*	*0.68*	*0.65*	*0.22*	*0.31*
5	*0.5*	*3.28*	*3.31*	*2.07*	*2.07*
10	*1*	*10.7*	*10.4*	*9.19*	*9.14*
20	*2*	*24.1*	*24.6*	*23.0*	*23.4*

Tab. 4.2: Comparison of the extraction velocities of the actuators

The speeds obtained by the model are similar to those actually measured on the TTB. It is possible to observe that the largest relative error regarding speed is obtained in the case of extraction with $U = 0.3\ V$ in the internal actuator, specifically an error of about 40% is obtained. *In order to have a better match between reality and the model, it would be necessary to conduct a new experimental activity with the aim of characterizing the static characteristic of the proportional valves of the actuators when low command signals are provided. As will be evidenced in the next part of this work, this will be not required for the purpose of this thesis.*

In order to fully characterize the model of hydraulic actuators, we have to analyze the forces generated by the actuators too.
Neglecting the damping coefficient and considering the eq. 3.4 adapted to the cases under consideration, it is possible to approximate the dynamic friction as:

$$F_d = p_{up} * S_{up} - p_{dw} * S_{dw} \tag{4.1}$$

Figures 4.7 and *4.8* show the comparison between actual and numerical forces.

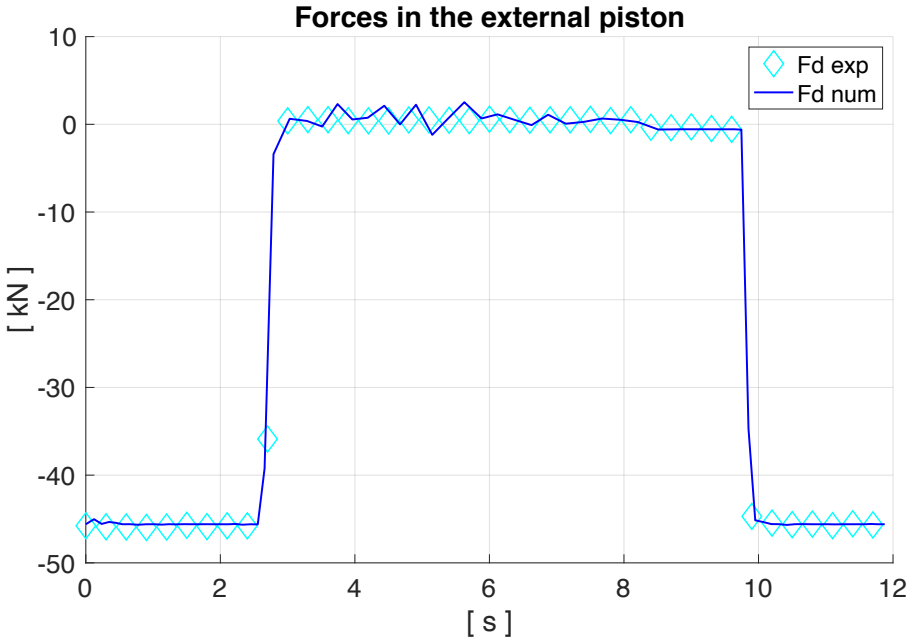

Fig. 4.7: Forces provided by the external piston

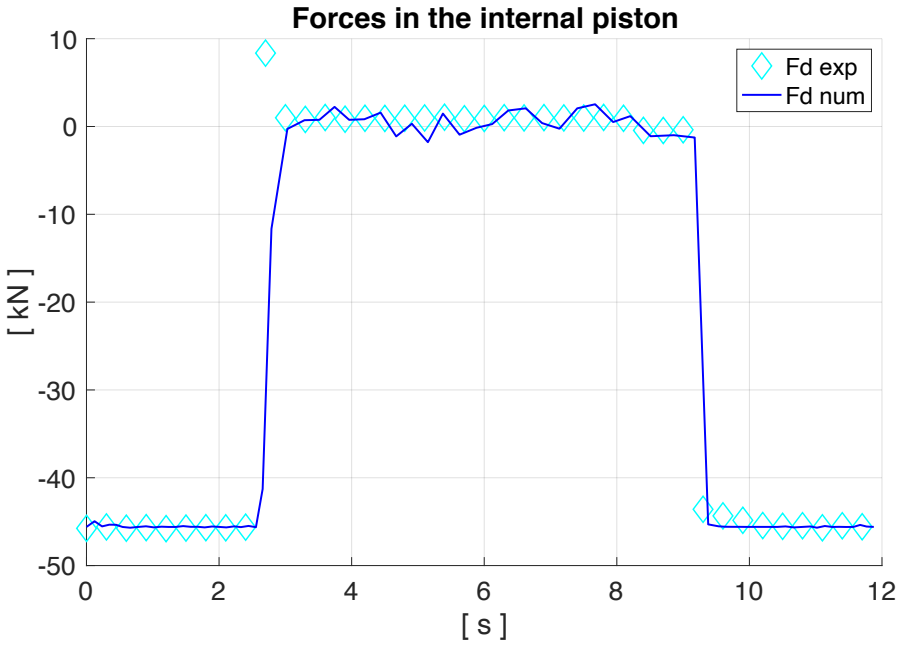

Fig. 4.8: Forces provided by the internal piston

Noting that the extraction of the pistons takes place at a constant speed, it is possible to estimate the value of the dynamic friction inside the pistons.
It was possible to observe that the dynamic friction assumes a value of about 500 N for the external actuator and 1200 N for the internal actuator. These experimentally found values were used to refine the actuator models.

4.2 Experimental validation of the belt reaction model

The TTB steel belt will perform the task of simulating the road surface during future tests on the tyre. Since the belt is one of the most important components for the functioning of the test bench, it is necessary to characterize it by means of a model capable of adequately describe its behavior. As explained in previous chapters, two mathematical models were made regarding the forces exchanged between the rollers and the belt and its transversal translation speed.

As previously done for the actuators, it is necessary to test these models in order to refine the parameters and validate them.

Experimental analysis of the belt forces

In order to refine and validate the model, an experimental activity was carried out which involves the extraction of the driven roller by means of the hydraulic actuators and the analysis of the forces that they exert on the belt.

In order to avoid the damaging of the driven-roller bearings, the inclination of the roller axis has to be limited. Therefore, a similar extraction speed of the two actuators is required. With the aim of obtaining an extraction speed of about $2 \div 3\ mm/s$ and by referring to the data of $tab.\,4.1$, command signals of $0.5\ V$ and $0.4\ V$ are provided to the internal and the external actuators, respectively.

Figures 4.9 and *4.10* show the control signals U $[\%]$, the pistons positions pos $[mm]$ and the pressures inside the chambers P_{up}, P_{dw} $[bar]$, for the external actuator and internal one, respectively.

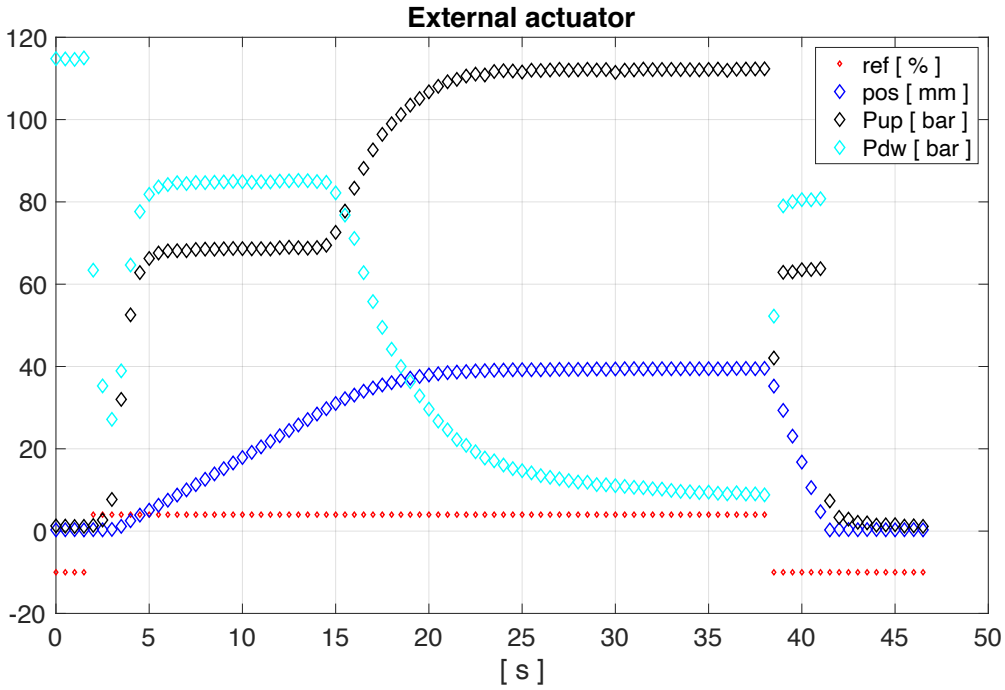

Fig. 4.9: Trends in the external actuator

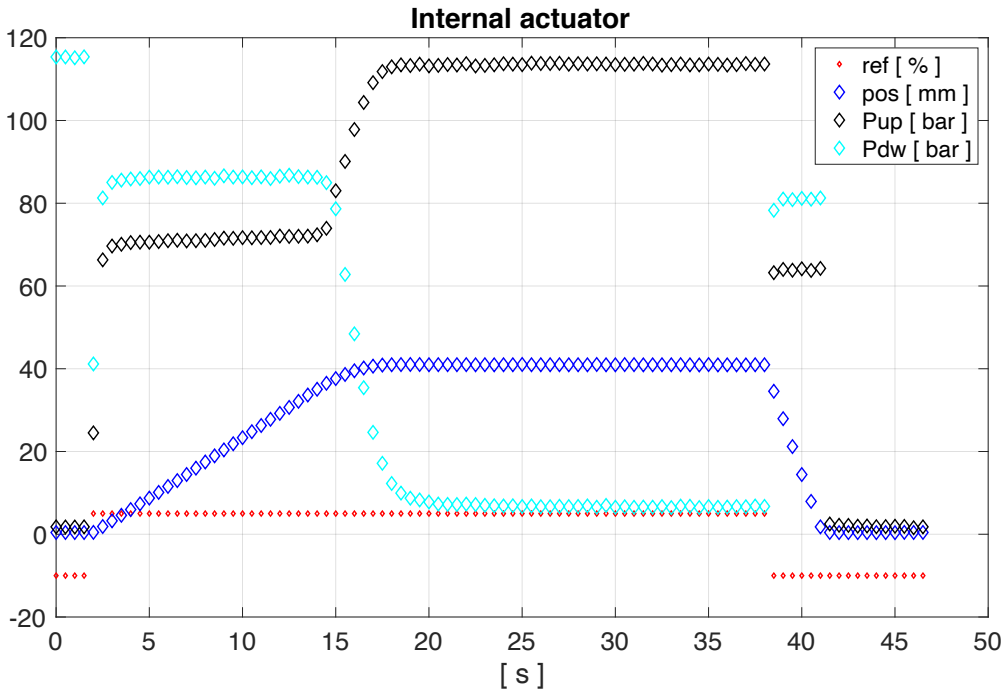

Fig. 4.10: Trends in the internal actuator

The same test was carried out using the Simulink model generated for the actuation system. As anticipated, the aim is to compare the results produced by the model with the measurements made on the TTB.

The comparisons regarding the piston positions and pressures in the chambers of the actuators in the absence of the belt reaction are omitted, as they have already been addressed in the paragraph relating to the validation of hydraulic actuators.

This phase aims at analyzing the forces developed by the actuators during the wrapping of the belt around the driven roller.

Figure 4.11 shows the good accordance between experimental and numerical results regarding the piston movement laws.

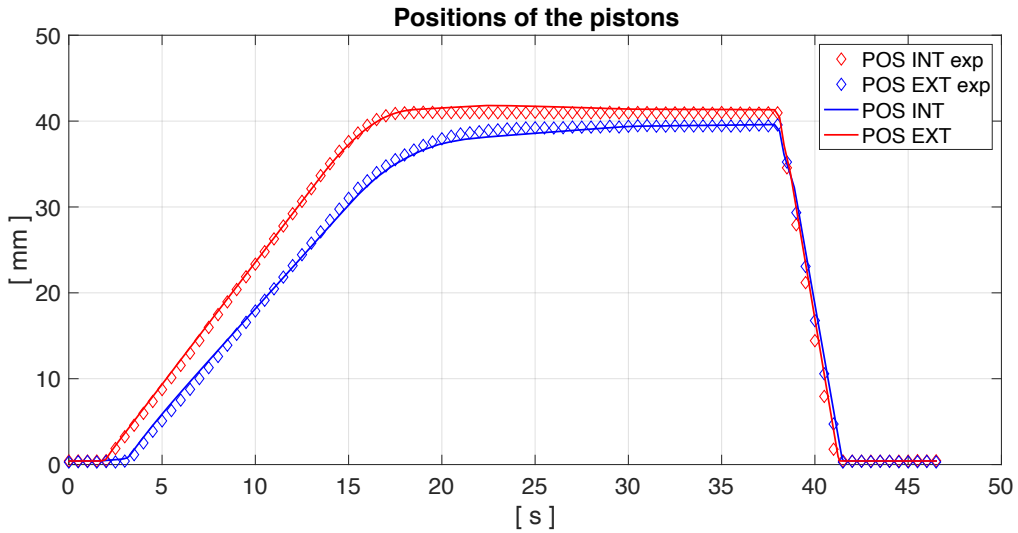

Fig. 4.11: Comparison between experimental and numerical positions of the pistons

It can be underlined as the extraction of the pistons begins at different time instants. This behavior is mainly due to the differences found in the proportional valves of the hydraulic actuators. The delay in the extraction of the external piston causes the internal one to come into contact with the belt first. As a result, the internal part of the belt begins to be stressed in advance of the external one. The effect can be seen by analyzing the reaction forces exerted by the tape on the actuators that are plotted in *figure 4.12*.

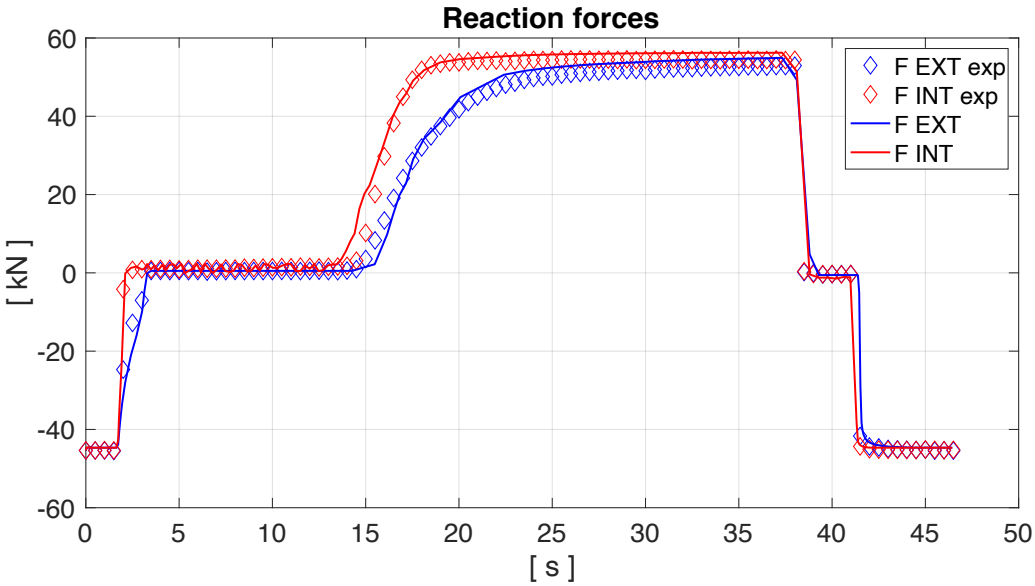

Fig. 4.12: Comparison between experimental and numerical forces provided by the pistons

Considering the experimental data, it can be seen how the reaction in the internal part of the belt begins to be felt at the time instant $13.5\ s$ which corresponds to a position

of the internal piston of $33.4\ mm$. Similarly, for the external piston, it is possible to observe that this is affected by the influence of the belt when its position reaches the value of $29.5\ mm$.

These piston position values for which the reaction of the belt begins to require a greater thrust of the actuators constitute the parameter $\xi_{0\,ext}$ and $\xi_{0\,int}$ within the models (*equations 3.1* and *3.2*).

The transient phase of wrapping the tape around the roller is modelled by considering a belt stiffness progressively increasing up to the theoretical value by mean a law experimentally evaluated.

Experimental analysis of the belt translation speed and validation

One of the aims of the TTB is to keep the rotating steel belt centered with respect to the rollers. This goal has to be guaranteed even in the presence of external forces, as the ones coming from the tyre under investigation during a test. The lack of this compliance may be dangerous for the TTB.

In order to achieve the goal when there are not external forces coming from the tyre, it is important to keep parallel the rotation axes of the rollers. The above condition cannot be satisfied imposing the same extraction position to the hydraulic actuators because the latter ones are assembled with a structural misalignment that requires to be estimated.

The idea is to experimentally characterize the relationship between the lateral drifting velocity $\dot{\eta}$ and the misalignment of the hydraulic pistons $\Delta\xi$. The latter is defined as:

$$\Delta\xi = \xi_{ext} - \xi_{int}$$

Once the steel belt has been tensioned and the desired misalignment is set through the actuation system, the drive roller sets the belt in motion.

The *figure 4.13* reports the measured transversal position η with respect to the number of turns performed by the steel belt around the rollers and the relative linear approximations (black continuous lines).

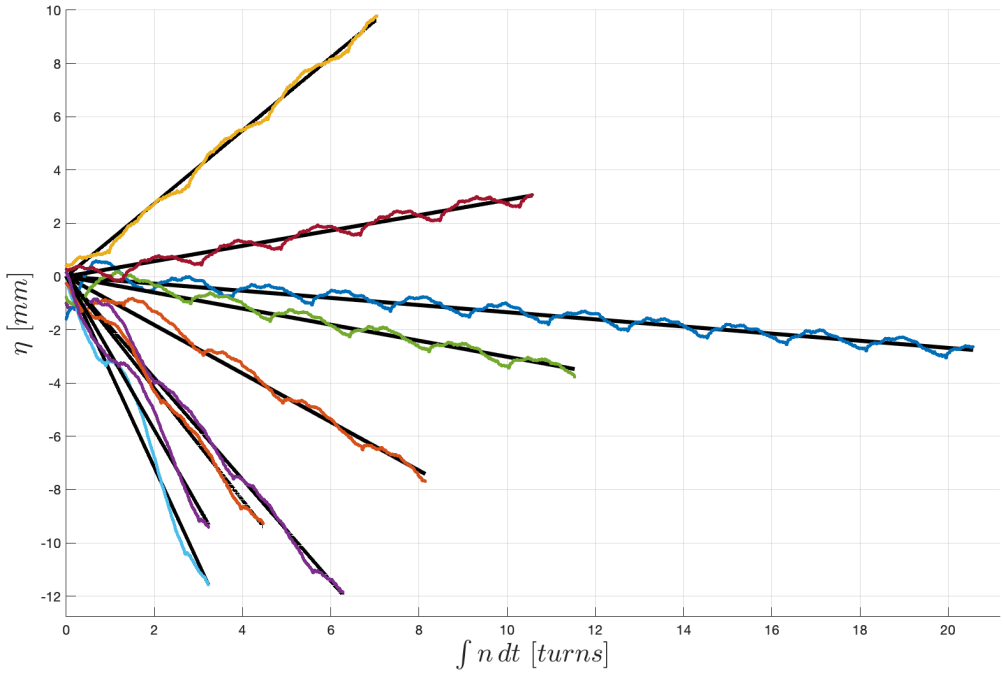

Fig. 4.13: Translation of the belt due to the imposed actuators misalignments

The transversal position of the steel belt is characterized by a periodic shifting, whose maximum amplitude is around $0.5\ mm$. These periodic oscillations are due to the imperfections of the belt's width.

With reference to *figure 4.13*, the belt-drifting per roller turn can be estimated as the slope of the linear trend. The *table 4.3* reports the estimated belt-drifting per turn (v_{drift}) with respect to the imposed misalignment $\Delta\xi$.

$\Delta\xi$ $[mm]$	v_{drift} $[mm/turn]$
-2.11	*-2.88*
-2.09	*-3.59*
-1.09	*-2.10*
-0.63	*-1.91*
0.08	*-0.91*
1.13	*-0.30*

1.16	*-0.13*
1.99	*0.29*
3.08	*1.37*

Tab. 4.3: Belt-drifting per roller turn due to the imposed misalignment

The *figure 4.14* shows the above results and the estimation of the misalignment $\Delta\xi$ that has to be imposed as offset to the hydraulic actuators in order to compensate the roller axes misalignment (red point).

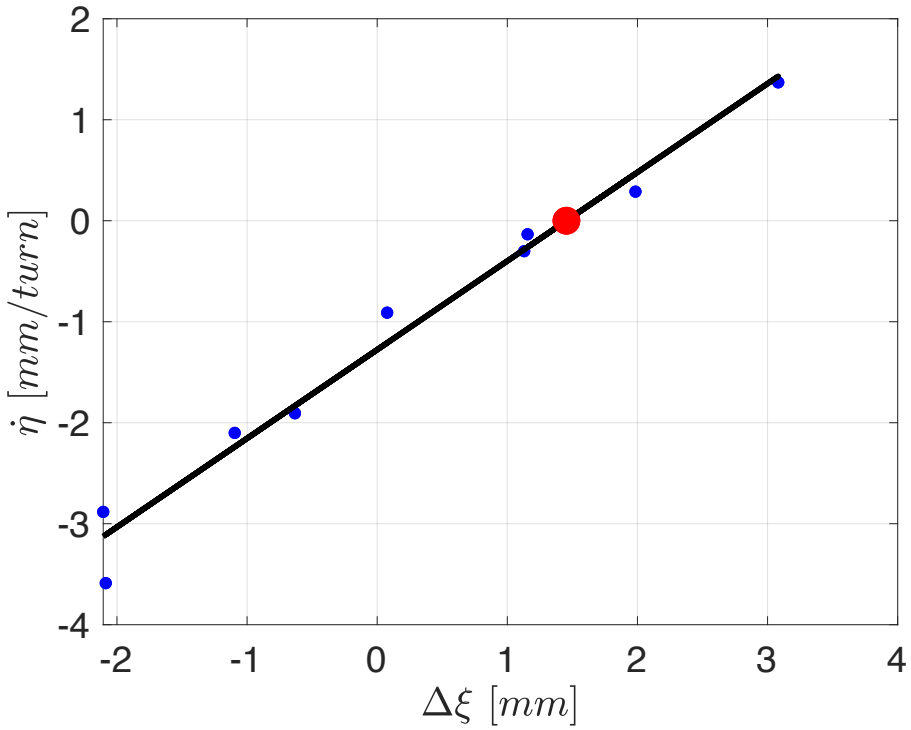

Fig. 4.14: Linearization of the translational belt speed

From the analysis performed on the belt-drifting per roller turn, the estimation of the misalignment to be imposed to the hydraulic actuators is $\overline{\Delta\xi} \cong 1.45\ mm$.
Imposing the above misalignment to the target position of the actuators, the structural offset is removed, and the rotation axes of the rollers are parallel one to each other.

From the previous results, the linearized relationship between the misalignment and the belt-drifting velocity is:

$$\dot{\eta} = [0.0146\,\Delta\xi - 0.0213]\,n \qquad \left[\frac{mm}{s}\right] \tag{4.4}$$

where:

$\Delta\xi$ is expressed axes misalignment $[mm]$

n is the roller rotational velocity $[rps]$

The above relationship can be written in the *Laplace* domain in the form of a transfer function as:

$$G_{\frac{\eta}{\Delta\xi}}(s) = \frac{0.0146}{s}\, n \tag{4.3}$$

This relationship obtained experimentally is of fundamental importance and will be used in order to design the control system for the translation of the belt.

Within the model implemented for the TTB, the relationship that describes the translation of the belt as a function of the misalignment of the actuators is given by *equation 3.3*.

The model is validated by estimating the experimental coefficient k and introducing the structural misaligned discovered $\overline{\Delta\xi}$.

It was decided to model the phenomenon by representing the linear trend estimated by *equation 4.2*. For this purpose, a misalignment of $1.45\ mm$ was introduced and the value 1.56 was assigned to the experimental coefficient k.

Figure 4.15 shows the numerical response provided by the model and the estimated speeds from the experimental data.

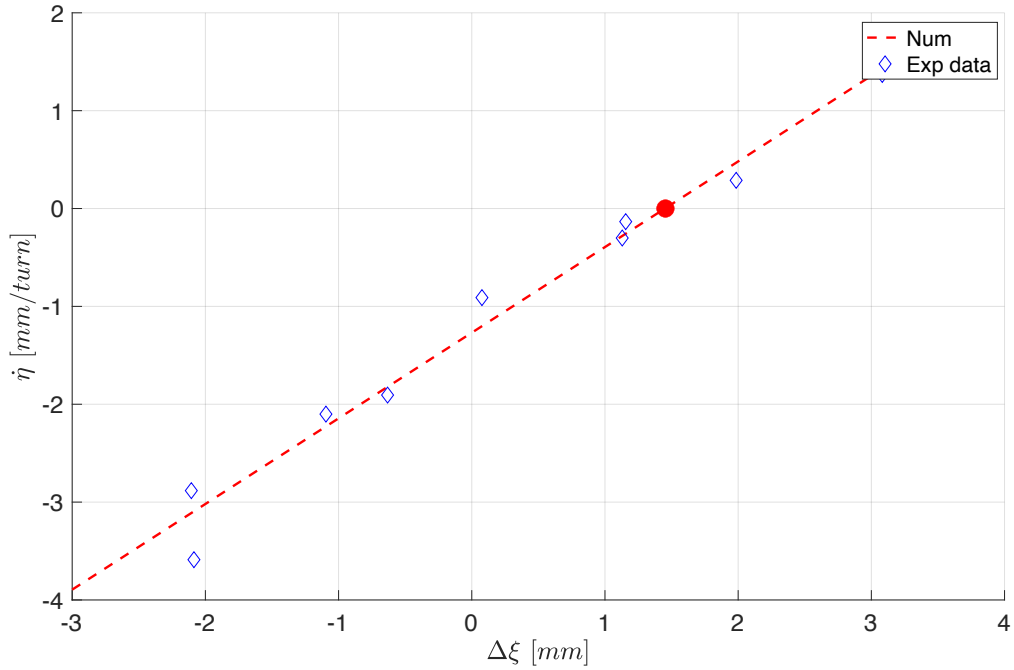

Fig. 4.15: Numerical translational belt speed

Chapter 5

Control design for the hydraulic actuator

This chapter is dedicated to the design of the position control system for hydraulic actuators. Before being able to design the controller, an identification analysis of the actuators must be carried out. That is, their transfer function must be estimated.
The first paragraph is dedicated to the identification of the actuators through experimental tests based on a command signal in the shape of a logarithmic chirp.
In order to validate the dynamic behavior of the actuator model, the same test is repeated also in the Simulink environment.
Once the transfer function related to the actuators has been estimated and the performance requirements defined, it is possible to move on to the design of the position control system, and finally, to evaluate its performance.

5.1 Hydraulic actuators identification and model validation

There are various ways to characterize the transfer function of a plant. Nowadays, the most used in the experimental field, are based on the responses produced according to the inputs provided. Among the various command signals that can be provided, one of the most used is the chirp. The latter consists of a sinusoid of constant amplitude, but whose frequency goes from a minimum to a maximum value in a given time interval.

The experimental analysis conducted to identify the transfer function of the hydraulic actuators is based on a logarithmic chirp, which has the particular characteristic of varying the frequency of the sinusoid with a logarithmic trend, thus also emphasizing the behavior at low frequencies of the established interval.

Going into the specifics of the experimental analysis conducted, the steel belt was put under tension by the advancement of the driven roller controlled by the hydraulic actuators. This first phase is intended to ensure that the test takes place in working conditions similar to those for tyre testing.

Once the belt has been tensioned, it is possible to proceed with the experimental identification of the actuators. One actuator was analyzed at a time, i.e. the chirp-shaped signal is supplied to one of the two actuators at a time, while the other is kept stationary by means of special valves in the hydraulic circuit. The logarithmic chirp provided was varied from $0.1\ Hz$ to $100\ Hz$ over a $100\ s$ interval.

In *figures 5.1* and *5.2* it is possible to observe the trends found during the identification analysis, specifically the command signal provided and the position and pressure measurements in the piston chambers for both actuators.

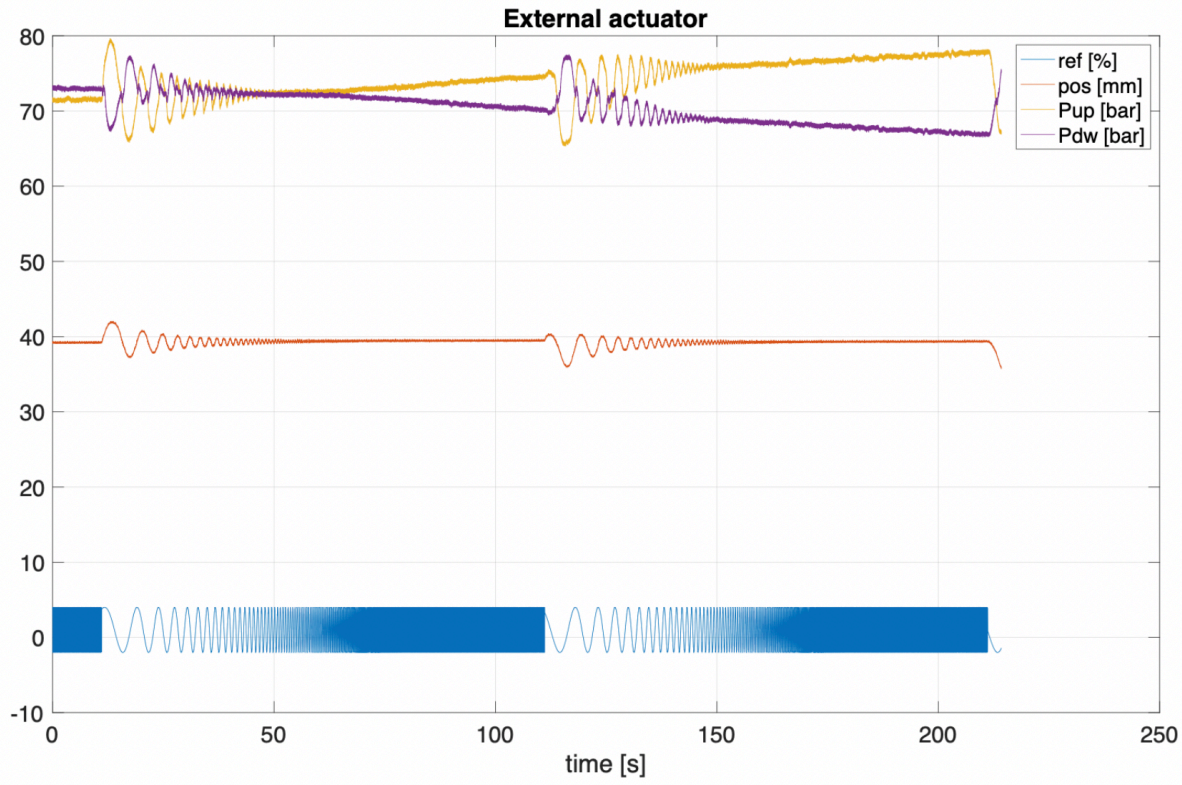

Fig. 5.1: Trend of the external actuator

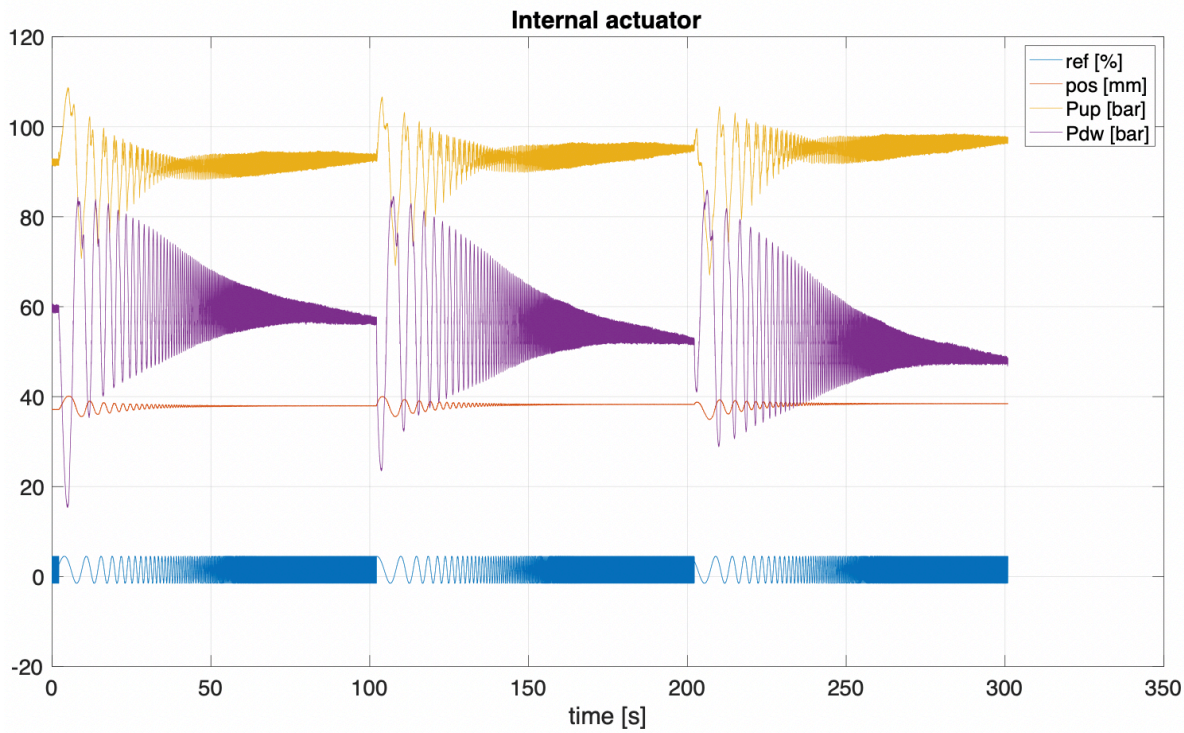

Fig. 5.2: Trend of the internal actuator

The measurements made on the command signal supplied U $[\%]$ and on the piston position $[mm]$ allow to obtain an estimate of the transfer function that correlates them. Specifically, through the Welch's averaged periodogram method based on these measurements, it is possible to obtain the corresponding Bode diagrams.

Figures 5.3 and *5.4* show the obtained Bode plots and the relative Coherences. This last parameter is reported to indicate the magnitude squared coherence between the input and output data when Welch's averaged modified periodogram method is used. The coherence value can assume values in the range $0 \div 1$.

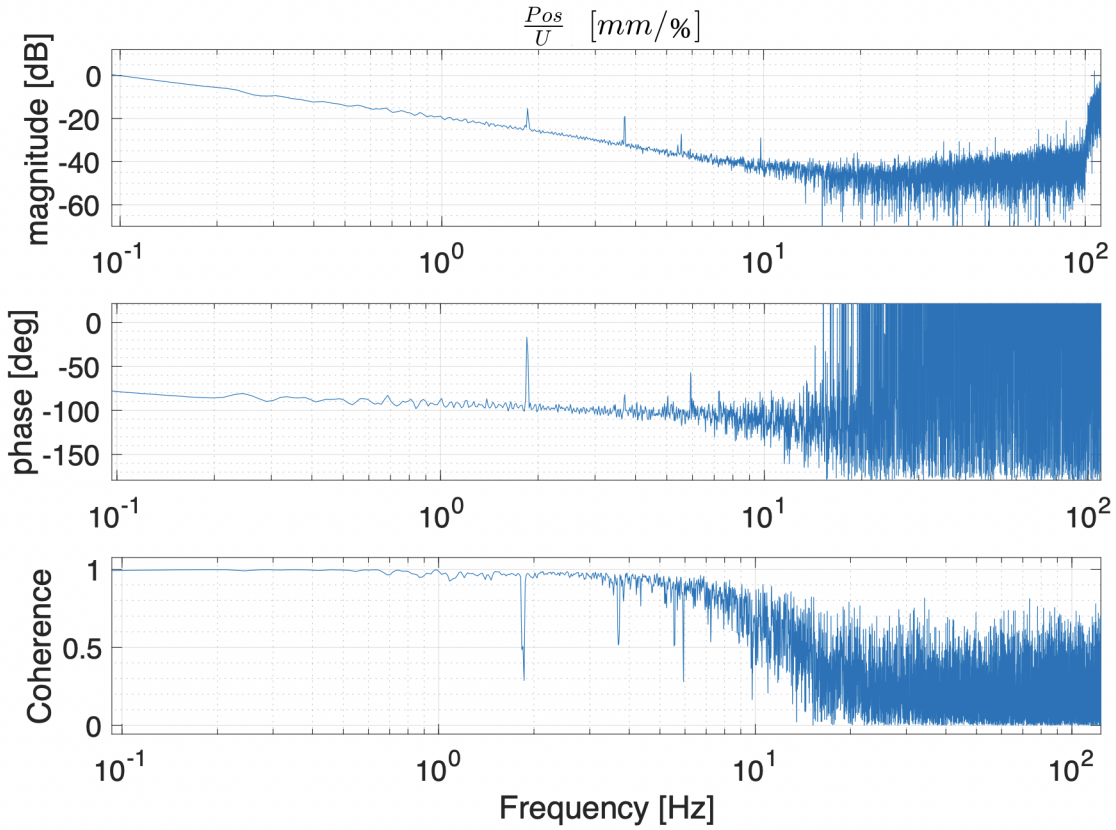

Fig. 5.3: Bode diagram for the external actuator estimated from the measurements

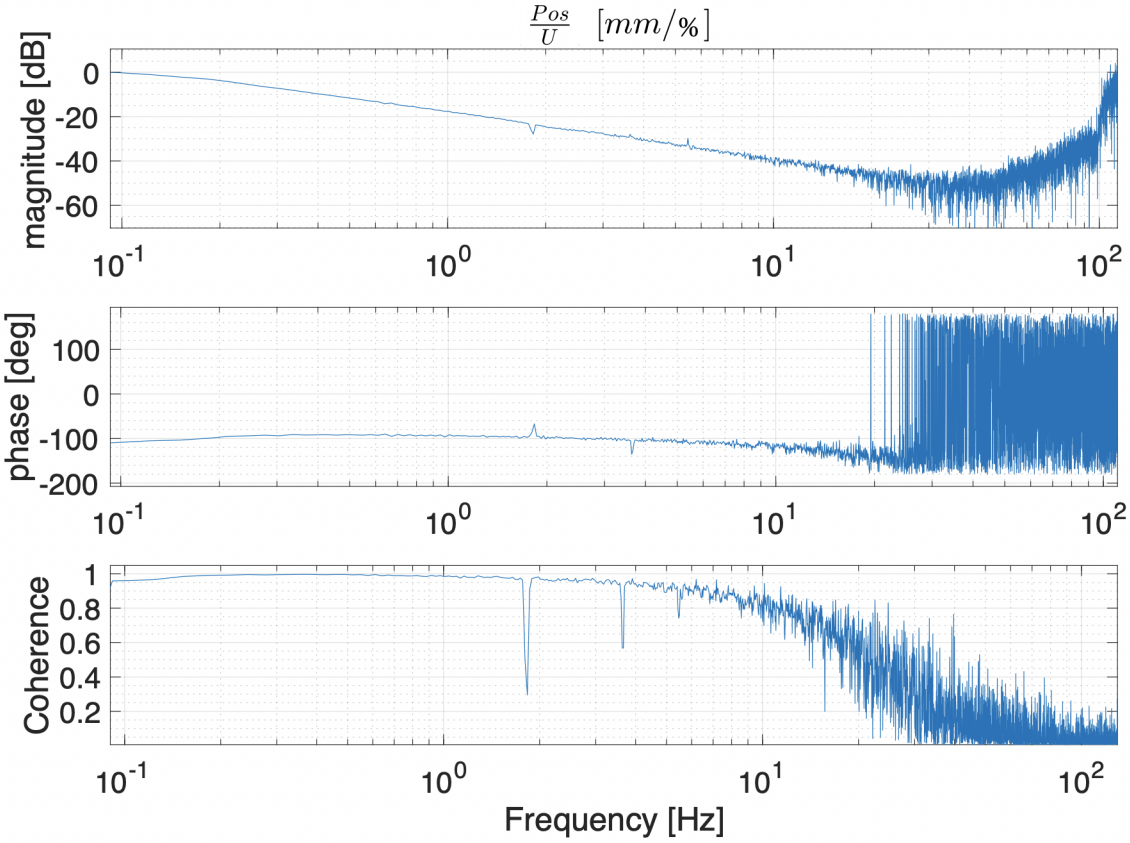

Fig. 5.4: Bode diagram for the internal actuator estimated from the measurements

Through the coherence index it is possible to state that the estimate of the Bode diagrams obtained are reliable in the frequency range $(0.1 \div 20)\, Hz$. For higher frequencies it is not possible to rely on the estimates obtained, but the high reliability frequency range obtained is sufficient for the purposes of the TTB.
The limitation on the range on which it is possible to rely is due to the measurement noise and the sampling frequency used by the TTB of $1\ kHz$.

In order to validate the model of the actuators, the same identification test was conducted on the model created in the Simulink environment.
The technique used to estimate the frequency response is the same, it is sufficient to perform the estimate based on the position data $[mm]$ produced by the model in response to a chirp-shaped input signal $U\,[\%]$. *Figures 5.5* and *5.6* show the estimated Bode diagrams and the relative consistencies for both actuators.

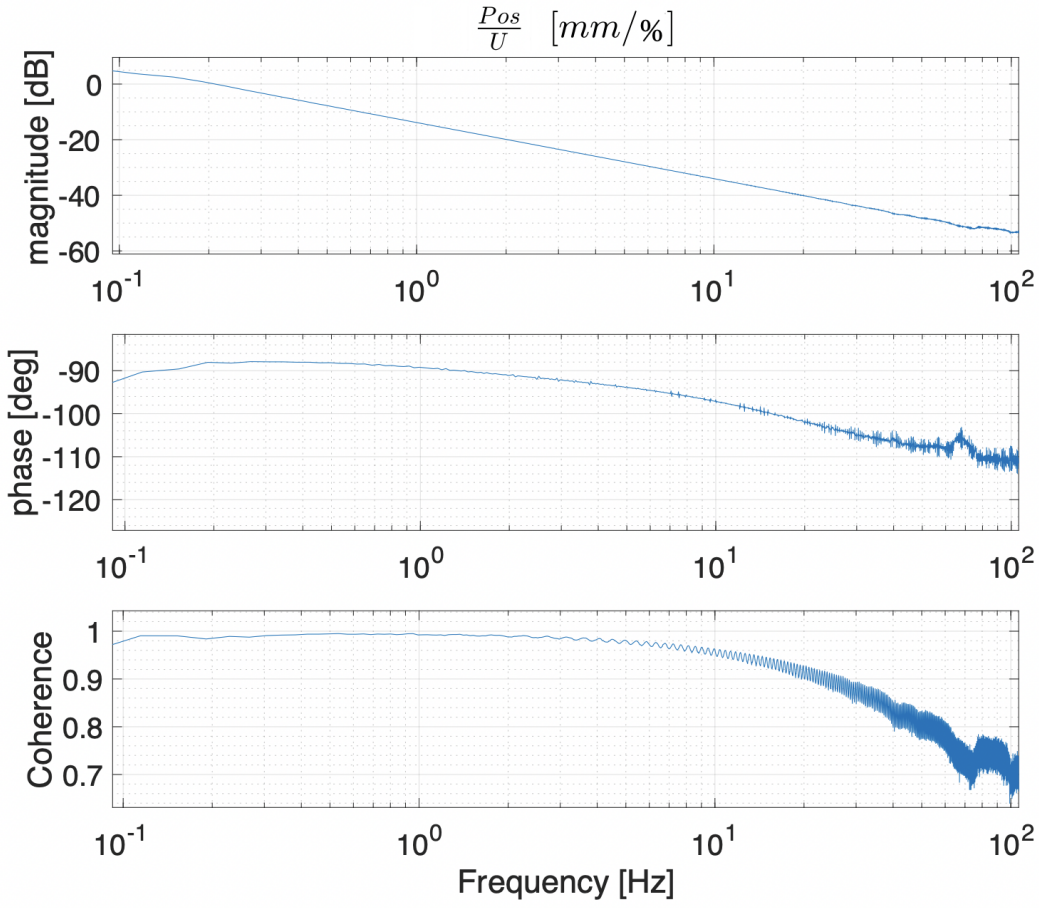

Fig. 5.5: Bode diagram for the external actuator estimated by the model

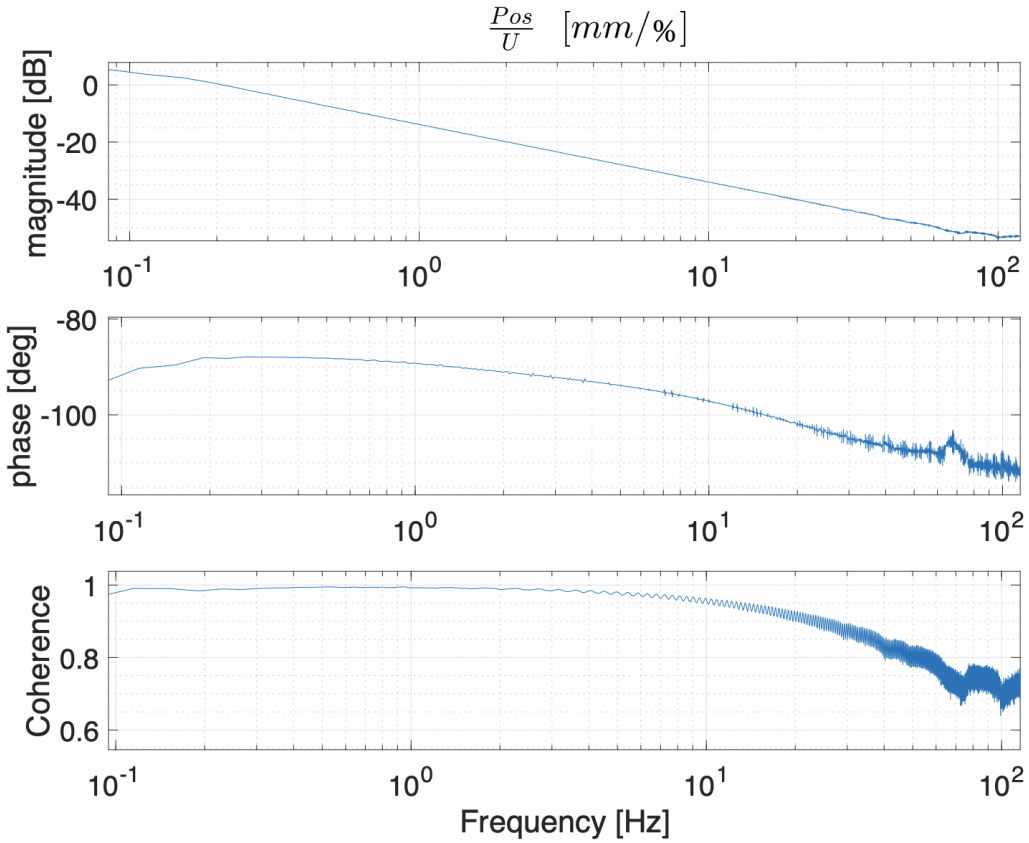

Fig. 5.6: Bode diagram for the internal actuator estimated by the model

By comparing the Bode diagrams estimated starting from the experimental data with those obtained from the models, it is possible to state that, in the working range $(0.1 \div 20)\ Hz$, both show a trend approximating that of a purely integrative system. In fact, it is possible to notice how the gain varies with a slope equal to $-20\ dB/dec$ and the phase is close to $-90°$.

What has been obtained can be demonstrated through the mathematical relations that describe the hydraulic actuator. In fact, the U command is proportional to the oil flow rate, and the latter is proportional to the piston extraction speed. It follows that the relationship between the command signal and the position is of an integrative type.

As for the behavior for frequencies higher than the working ones, it was decided to approximate the behavior by considering the insertion of two poles centered at $80\ Hz\ (500\ rad/sec)$. This choice derives from the dynamic behavior of the proportional valve in the worst possible case.

Based on what was obtained experimentally and on the hypothesis of working in the worst possible condition of the proportional valve, the transfer function of the hydraulic actuators can be approximated to:

$$G_{HA}(s) = \frac{3.635\ 10^5}{s\ (s+500)^2} \tag{5.1}$$

where the command signal U is expressed as $[\%]$ while the piston position is expressed in $[mm]$.

5.2 Hydraulic actuator positioning control design

The hydraulic actuators must allow to obtain the desired position and inclination of the driven roller at any time. In order to be able to succeed in the intended purposes it is necessary that the actuators are controlled in terms of position.

As shown up to this point, the pistons in the actuators are able to extract or retract with a speed that depends on the applied command signal. It is therefore necessary to design a control system that allows to set the position of the hydraulic pistons in the actuators.

Based on the experimental evidence, the actuators were approximated by the transfer function $G_{HA}(s)$ reported as *eq. 5.1*.

Since the TTB allows the measurement of piston positions in real time, the control system implemented is said to be of a closed loop type.

Figure 5.7 shows a basic schematic of a closed-loop control system. It can be noted that, in this case, the reference signal consists of the position to be obtained ξ_{ref}, the measured piston position is reported as ξ, the hydraulic actuator is represented by the transfer function $G_{HA}(s)$, while $G_{c\_\xi}(s)$ represents the transfer function of the controller to be designed.

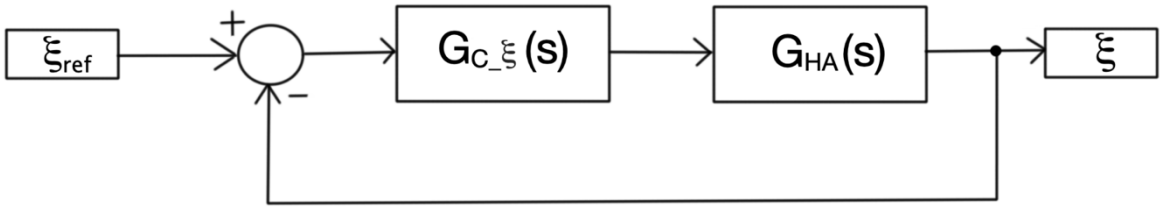

Fig. 5.7: Closed loop control system schematic

The control system must ensure that the position of the actuator piston ξ follows the reference position ξ_{ref} respecting the time requirements imposed. Compatibly with the future working conditions of the TTB, the step response of the controlled system is desired to have a settling time of 5% of the order of tenths of a second, an overshoot percentage lower than 10% and must be able to follow a first order polynomial reference (ramp) with a zero steady state error. The latter requirement allows to set the desired velocity of the hydraulic piston if needed.
The previous step response requirements are summarized in *tab. 5.1*.

$t_{s,5\%} \cong 0.1\ s$	$\hat{s} < 10\ \%$	$\left\|e^{\infty}_{\xi\_ref}\right\| = 0$

Tab. 5.1: Time domain requirements for the control system

There are multiple techniques that allow to create a control system. In this first phase it was decided to opt for a control based on the loop-shaping technique. This technique is suitable for controlling linear systems and involves modeling the open loop transfer function $L(s)$ in frequency. The latter transfer function is represented by the product of all the blocks present in the open loop. Referring to the basic schematic of the control system, it can be observed that the feedback has been considered unitary and therefore:

$$L(s) = G_{c\_\xi}(s) * G_{HA}(s) \tag{5.2}$$

Before starting with the design of the controller, it is also useful to remember the sensitivity transfer function $S(s)$ and inverse sensitivity transfer function $T(s)$ defined as follows:

$$S(s) = \frac{1}{1+L(s)} \tag{5.3}$$

$$T(s) = 1 - S(s) = \frac{L(s)}{1+L(s)} \tag{5.4}$$

These last two functions are particularly important because they allow to characterize and analyze the response of the control system both in the presence of reference signals and in the presence of any disturbances acting within the chain.
In particular, it is possible to demonstrate how the transfer function that binds the reference signal to the output signal coincides with $T(s)$ in the case of unitary retraction.

The control system design begins with the translation of time-domain specifications into frequency-domain constraints. Assuming we design the system in such a way as to have a response similar to that of the second order, i.e.

$$T(s) = \frac{\omega_n^2}{s^2 + 2\xi_0\omega_n + \omega_n^2}$$

starting from the time requirements regarding the transitory, it is possible to calculate:

- *the dumping coefficient*

$$\xi_0 = \frac{|\ln(\hat{s})|}{\sqrt{\pi^2 + ln^2(\hat{s})}} = 0.69$$

  Where it was decided to consider $\hat{s} = 5\%$ in order to have margin with respect to the requirement;

- *the natural frequency*

$$\omega_n = \frac{3}{\xi\, t_{s,5\%}} \cong 44\, rad/s \; = 7Hz$$

At this point we need to think about the time requirement $\left|e^{\infty}_{\xi\_ref}\right| = 0$. It is possible to demonstrate that, in order to comply with this stationary requirement, it is necessary that the system is of type 2. The definition of the type of a system coincides

with the number of poles in the origin possessed by the function $L(s)$. Considering the *eq. 5.2* and *5.1*, it is possible to note that it is necessary to impose a pole in the origin in the transfer function of the controller. Based on the foregoing, the controller at the beginning of the design will be of the form:

$$G_{c\_\xi}(s) = \frac{k_c}{s}$$

where k_c indicates the generalized dc gain of the controller.

Through the Nyquist's stability criterion, it is possible to assert that k_c must assume a positive value in order to make the control system stabilizable.

As announced, the controller design is done based on the frequency response of the open loop function. In particular, it is convenient to analyze the frequency response through the Nichols diagram.
On this diagram it is possible to view the progress of the module and the phase of $L(s)$ as a function of frequency.
The basic requirement of the control system is stability. In order to achieve this property, the curve representing $L(s)$ must pass to the right of the critical point, known as the point corresponding to a phase of $-180\,°$ and a magnitude of $0\ dB$.
By means of the damping coefficient ξ_0 estimated by the constraint on the overshoot, it is possible to define peak values for the transfer functions $S(s)$ and $T(s)$. These values are represented inside the Nichols diagram as ellipses which must not be crossed by the curve representing $L(s)$. This last condition has an additional functionality, in fact, in addition to allowing a determined overshoot, it allows to guarantee the stability margins of phase and gain.
The last consideration concerns the fact that the $L(s)$ curve have to cross the axis at $0\ dB$ at a frequency close to that of the previously estimated natural frequency, so as to ensure the desired bandwidth.

By initially defining k_c as unitary, it is possible to analyze the curve of the starting open loop system, that is:

$$L(s) = G_{c\_\xi}(s) * G_{HA}(s) = \frac{1}{s} \frac{3.365\ 10^5}{s(s+500)^2}$$

whose representation on the Nichols diagram is shown in *figure 5.8*.

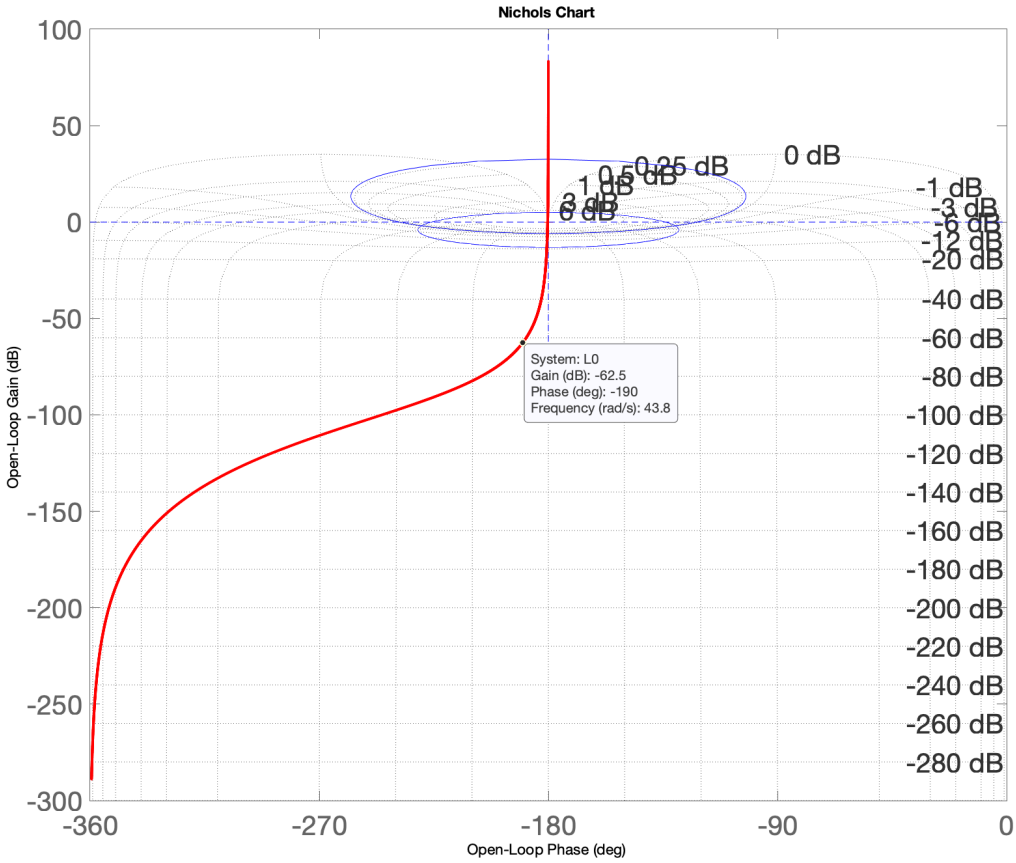

Fig. 5.8: Initial $L(s)$ on the Nichols diagram

It is possible to observe how it is necessary to translate the curve to the right and upwards. This is possible through the introduction of leading (or derivative) networks within the controller's transfer function.

The leading networks are of the form:

$$H(s) = \frac{1 + {}^{s}/_{z_d}}{1 + {}^{s}/_{m_d\ z_d}}$$

where the coefficients m_d and z_d allow to determine the range of frequencies on which acts the phase recovery and a consequent increase in gain.

A solution able to meet the imposed requirements is obtained for $k_c = 20$ and by the addition of the following leading networks:

$$H_1(s) = \frac{16\,(s+10)}{(s+160)}, \qquad H_2(s) = \frac{16\,(s+0.67)}{(s+10.67)}$$

The controller consists of a transfer function:

$$G_{c\_\xi}(s) = \frac{5120}{s}\frac{(s+10)(s+0.67)}{(s+160)(s+10.67)}$$

It is possible to note that within $G_{c\_\xi}(s)$ there are a zero and a pole similar to each other. After making the relevant checks, it was decided to simplify the controller by eliminating the similar zero and pole. It follows a controller in the form:

$$G_{c\_\xi}(s) = \frac{5120}{s}\frac{(s+0.67)}{(s+160)}$$

Figure 5.9 shows the Nichols diagram relating to the open loop function with the controller obtained after carrying out the simplification.

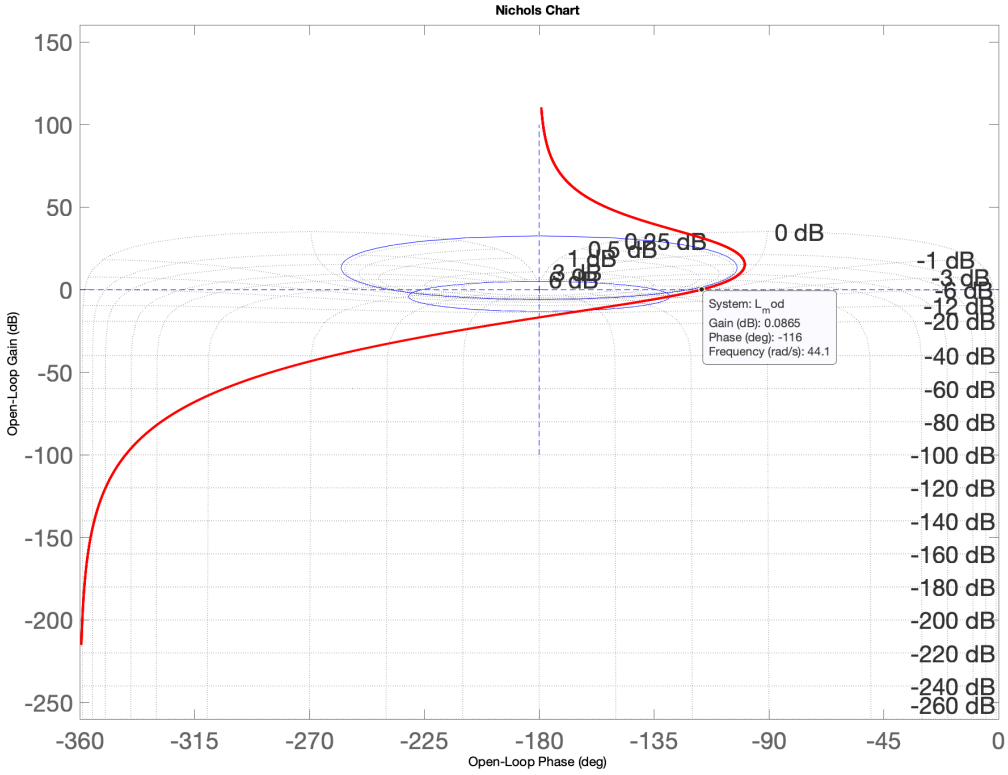

Fig. 5.9: Final $L(s)$ on the Nichols diagram

For safety reasons, it was decided to limit the velocities of the piston, i.e. the control signal of the actuators has been limited to a range equal to $\pm 30\%$ of the possible one. This condition can be interpreted as a saturation of the applicable command and can result in the phenomenon of windup, that is a non-linear overshoot due to the integrative component of the controller.

The problem can be solved by building the controller through an architecture capable of mitigating the effect of any saturation of the command signal.

Figure 5.10 shows the implementation of the anti-windup controller in the Simulink environment, which is the same used by the PLC inside the TTB.

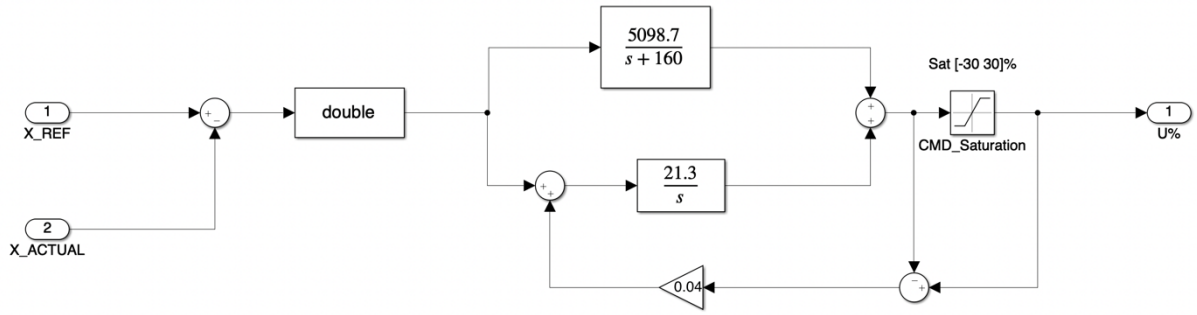

Fig. 5.10: Controller for the position of the hydraulic piston in Simulink environment

5.3 Experimental analysis and validation of the actuator controlled in position

The control system for the position of the actuator must be tested to verify that the project specifications shown in *table 5.1* are actually respected in the actuators within the TTB.

The experimental verification carried out on the test bench involves the analysis of the position assumed by the actuator in response to a reference consisting of a series of steps of varying width.

Figure 5.11 shows the position reference provided and the position assumed by the actuator.

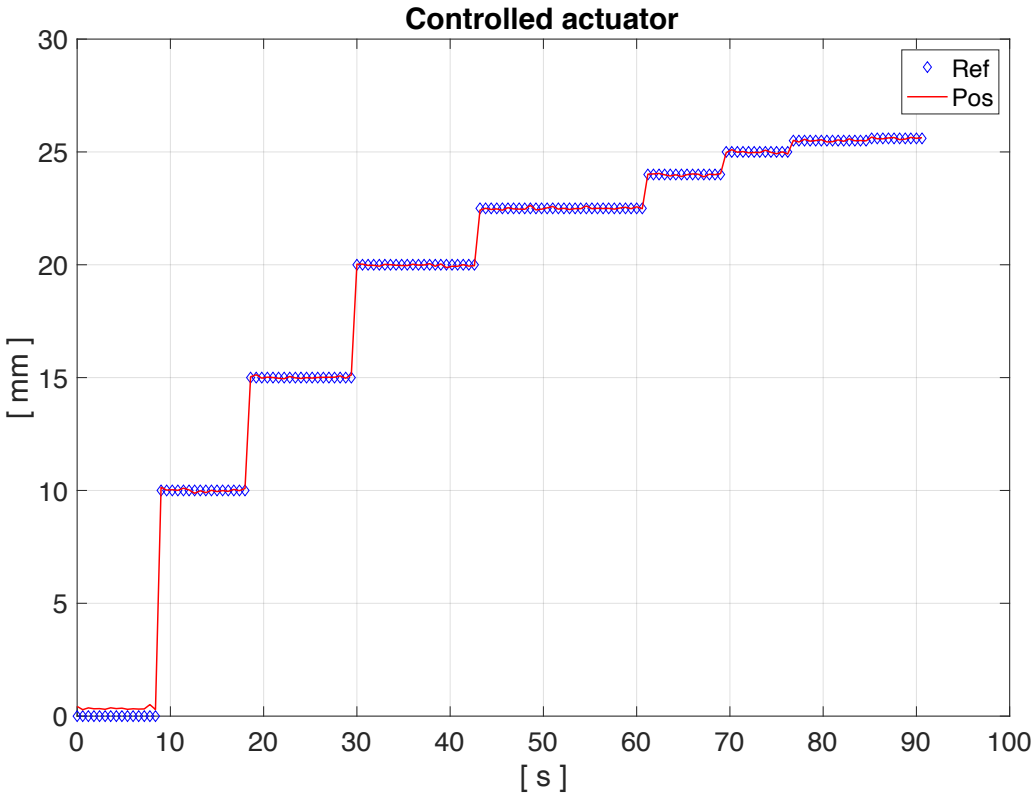

Fig. 5.11: Series of step responses

In order to be able to analyze the step response, it is sufficient to focus on one of the steps provided in the test. *Figure 5.12* shows the magnification for the second step, that is, with a width of $5\ mm$.

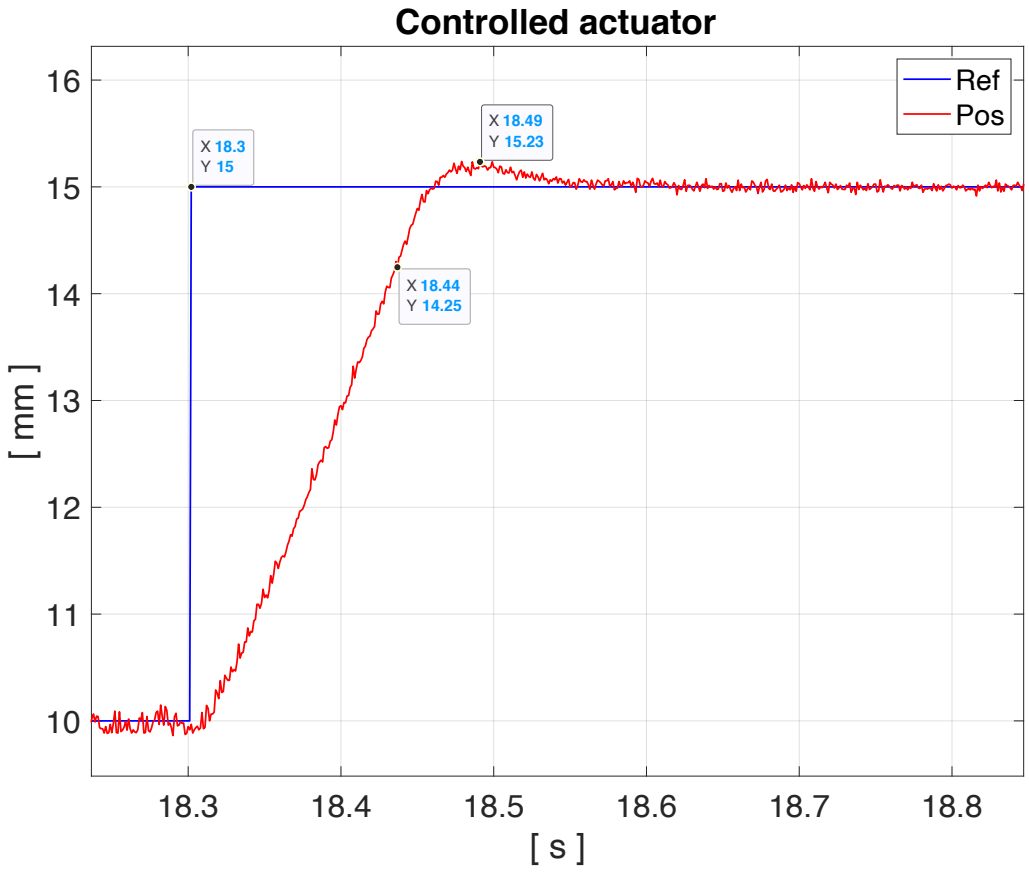

Fig. 5.12: Singular step response

Referring to the specific case shown in *figure 5.12*, the overshoot measured is $4.6\ \%$, while the settling time is equal to $0.14\ s$.

Referring to all the responses to the step carried out, the average values of the percentage overshoot and the settling time are estimated. The values obtained are shown below:

$$\overline{t_{s,5\%}} = 0{,}14\ s$$

$$\overline{\hat{s}} = 7{,}3\ \%$$

It is possible to observe how the control system respects the time specifications in the transient, in fact the requirements on the settling time and on the percentage overshoot are both respected. The performance is slightly lower than the design one, but this is due to the fact that, for safety reasons, it was decided to limit the extraction speed by limiting the possible values of U to the range $[-30 \div 30]\ \%$.

It remains to be verified that the stationary requirement regarding the tracking of a ramp-shaped reference signal occurs with a null error, that is $\left|e^{\infty}_{\xi\_ref}\right| = 0$.

Remembering that for safety reasons the command signal is limited to be $|U| \leq 30\%$, it follows a limit on the maximum extraction / retraction speed, therefore the stationary requirement can be satisfied only if the required speed is lower than a certain limit. From the previous experimental activities carried out on the actuators, it is possible to observe how a control signal $U = 20\%$ corresponds to a speed greater than $20\ mm/s$.

It should be borne in mind that the tracking of a speed reference is useful inside the TTB for correct belt tensioning. The latter is carried out with speeds not exceeding $5\ mm/s$, so by performing the tracking test for a reference speed of $10\ mm/s$ it is possible to ensure that the tensioning of the belt will be carried out in the desired manner.

Figure 5.13 shows the reference positions and those actually reached by the piston during the following test of a ramp signal with a $10\ mm/s$ slope.

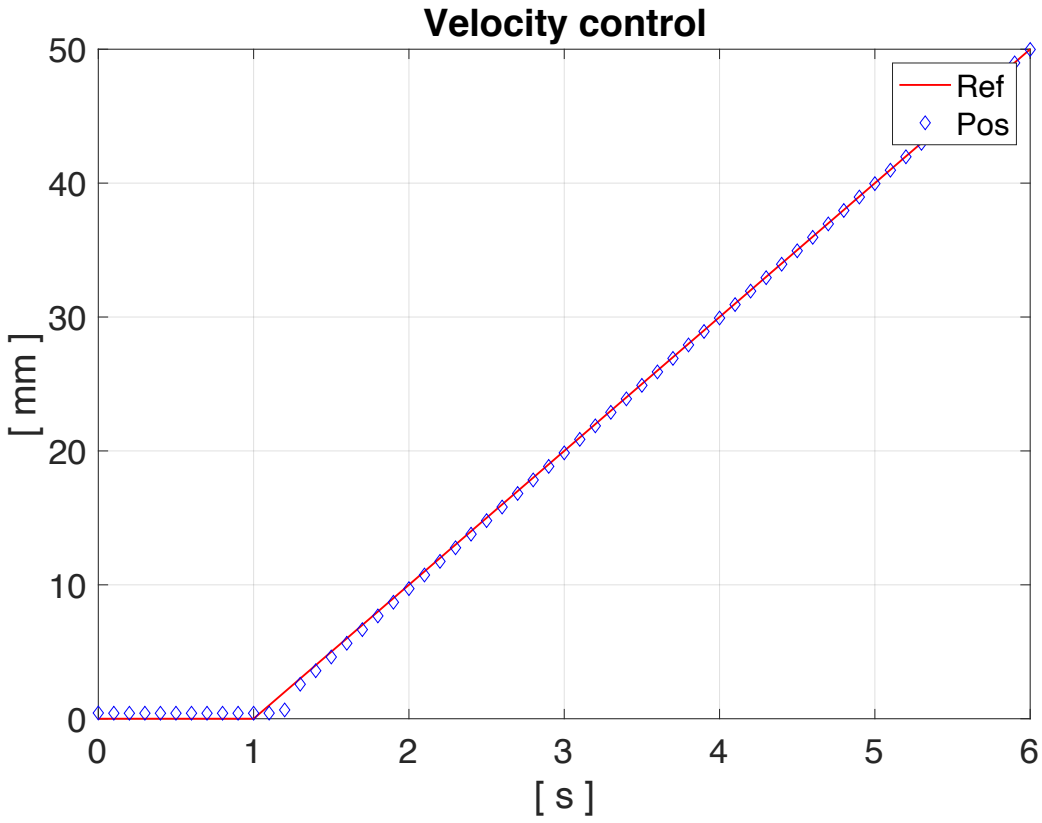

Fig. 5.13: Response to a $10\ mm/s$ ramp signal

It can be said that all three of the time requirements are met. *Table 5.2* summarizes the results obtained with regard to the control system in the position of the actuator.

	$Requirements$		
	$t_{s,5\%}$ $[\,s\,]$	$\hat{s}$ $[\,\%\,]$	$\lvert e^{\infty}_{\xi\_ref} \rvert$ $[\,mm\,]$
$Requested$	$\cong 0.1\ s$	$< 10\ \%$	0
$Achieved$	0.14	$7{,}3$	0

Tab. 5.2: Results provided by the control system

In order to validate the model of the actuator controlled in position, the same step reference signal is supplied to the model of the hydraulic actuator in the Simulink environment. *Figure 5.14* shows the comparison between the position actually assumed and that predicted by the model in the case of the same step examined previously.

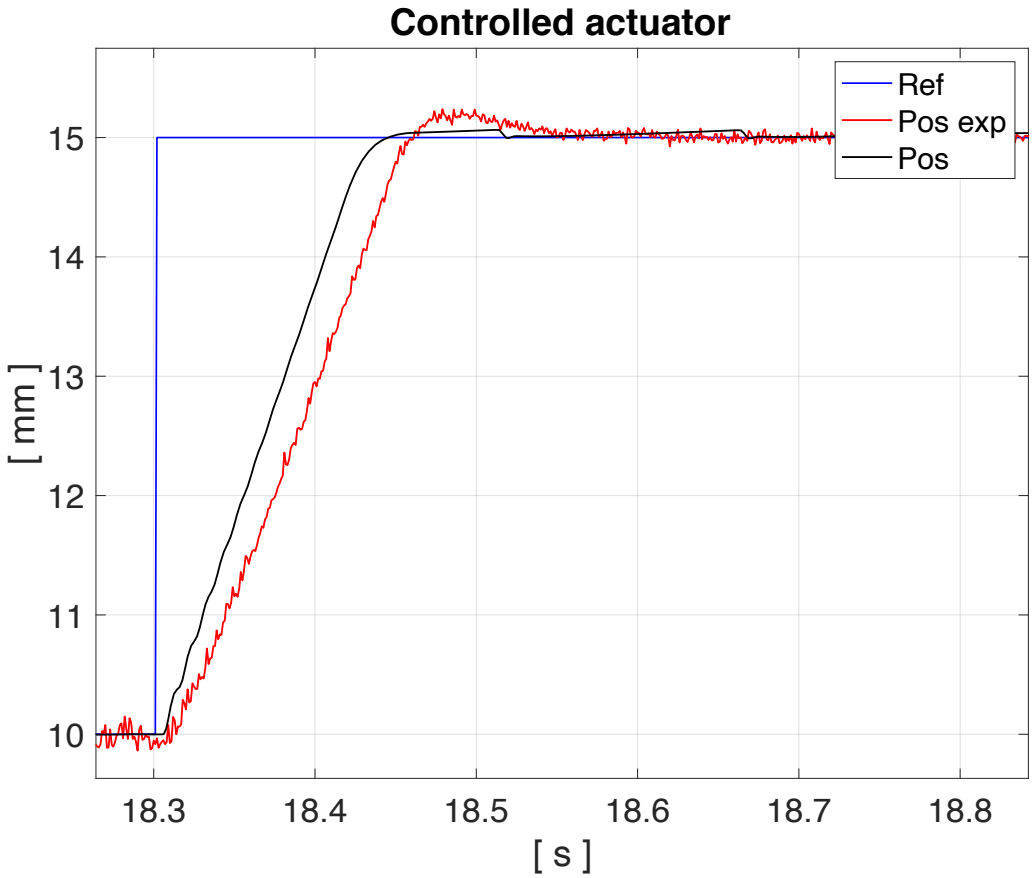

Fig. 5.14: Step response comparison between model and reality

It is possible to notice how the model presents a step response very similar to the experimental one both in terms of settling time and in terms of overshoot.

By carrying out the same type of analysis performed starting on the experimental data, it is possible to estimate an average settling time and an average percentage overshoot equal to:

$$\overline{t_{s,5\%}} = 0.11\ s$$

$$\overline{\hat{s}} = 2.1\ \%$$

As for the tracking of a ramp reference, as long as signals with a slope of less than $37\ mm/s$ are provided, the model also estimates a null error after the transient extinction.

Chapter 6

Control design for the belt

6.1 Identification of the actuators controlled in position

The TTB allows the control of the transversal translation of the belt by positioning the rotational axis of the driven roller. As anticipated, this is obtained through the actuators position control carried out in the previous chapters. In order to be able to realize a second control system able to govern the translation of the belt, we have to estimate the transfer function of the actuators controlled in position. Therefore, a new identification process based on a specific experimental analysis has been performed. The input signal, that is the position reference provided to the controlled actuator, is a logarithmic chirp of amplitude $\pm\, 2\ mm$ having a frequency in the range from $0.1\ Hz$ to $100\ Hz$ with a time window of $300\ s$.

One actuator is analyzed at a time, i.e. the chirp signal is provided to the actuator examined, while the other is kept at a fixed position by means of a constant position reference.

The *Figure 6.1*. shows the reference and the actual position signal reached by the hydraulic piston for both tests on the actuators.

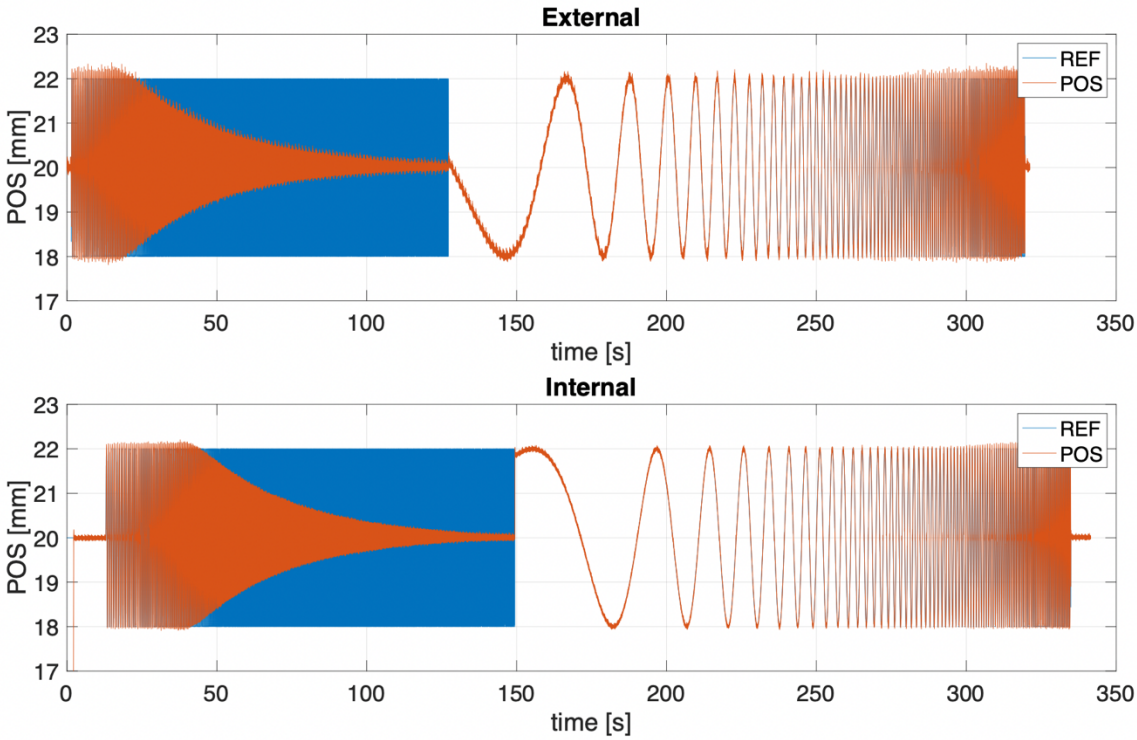

Fig. 6.1: Logarithmic Chirp responses of the actuators

An estimation of the transfer function of the controlled actuators have been obtained by applying the Welch's averaged periodogram method based on these experimental data. The *Figure 6.2* shows the obtained Bode plots and the relative Coherences for both the controlled actuators.

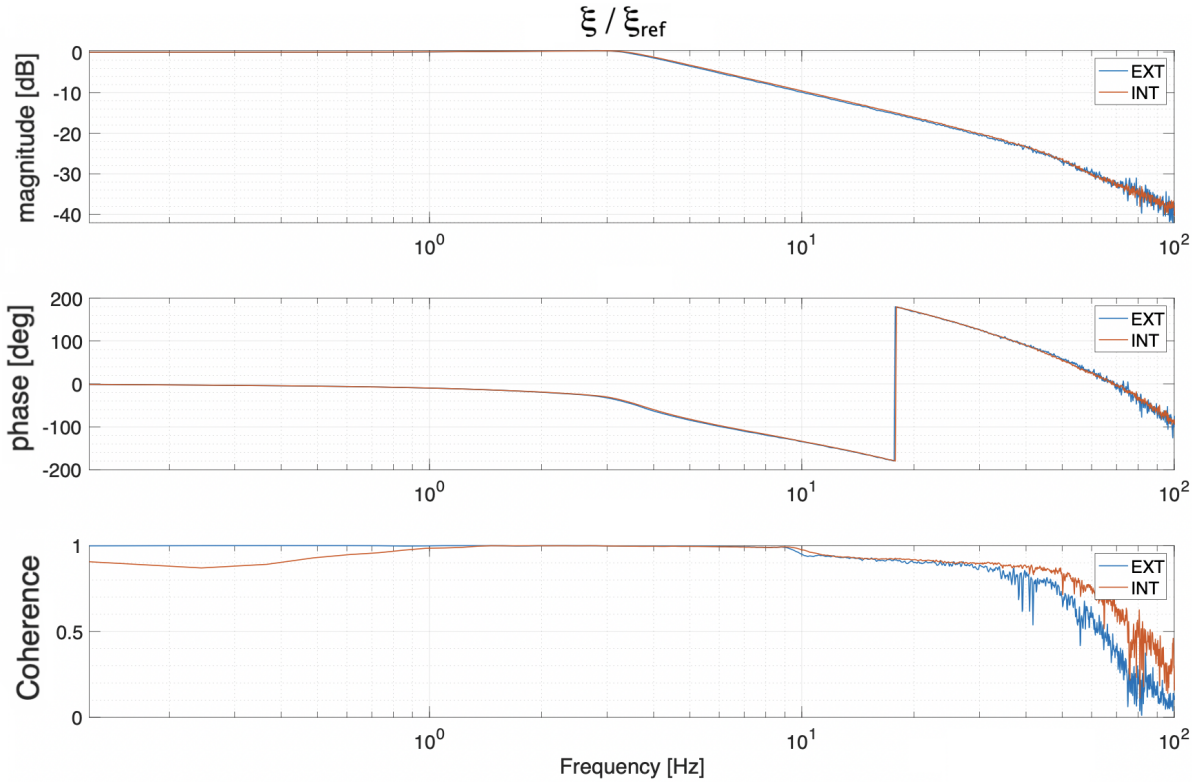

Fig. 6.2: Estimated Bode diagrams of the controlled actuators

The Bode diagrams obtained show that the two actuators controlled in position behave in a similar way. The dynamic characteristics obtained can be considered those of a low pass filter with a cut-off frequency around $5\ Hz$. The diagram shows that the actuators are able to faithfully reproduce position signals that vary with a frequency lower than $1\ Hz$, the frequencies in the interval between $1\ Hz$ and $3.3\ Hz$ are slightly amplified (the peak of $0.37\ dB$ is reached around $2.6\ Hz$), the higher frequencies up to $40\ Hz$ are attenuated with a slope close to $-20\ dB\ /\ dec$, above $40\ Hz$ further poles relating to frequencies deemed not of interest for the intended purposes are beginning to be felt.

Starting from the experimental Bode diagrams, a mask was created, that is a transfer function capable of approximating the frequency trend of the controlled actuators in the frequency range of interest. The identified transfer function as an approximation is:

$$G_{a\_ctrl} = \frac{5.5636e06\ (s + 50)\ (s + 10)}{(s + 550)\text{^}2\ (s + 19)\ (s\text{^}2\ +\ 41.8s\ +\ 484)}$$

The Figure 6.3 shows the comparison between the module estimated by the identification test and the transfer function used as an approximation for the controlled actuator G_{a_ctrl}.

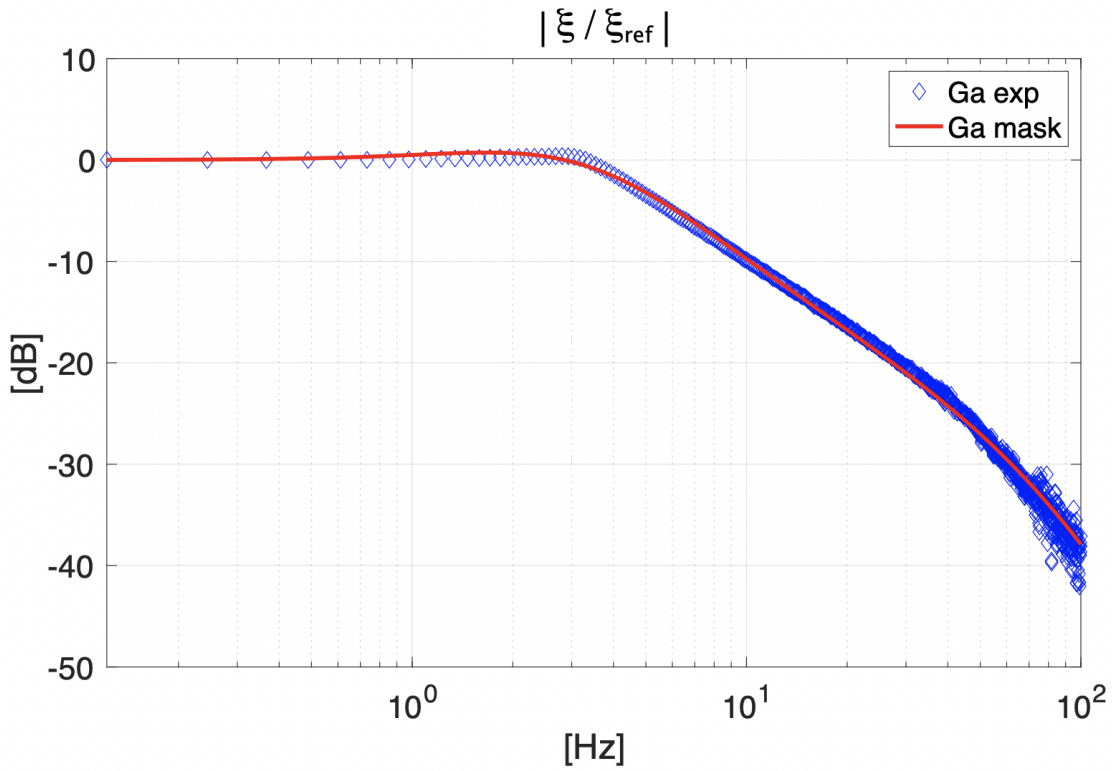

Fig. 6.3: Magnitude of the controlled actuators

6.2 Control system for the steel belt

The theoretical analyzes carried out on the steel belt have highlighted how the belt is kept in position on the rollers thanks to adherence provided by the static friction. The frictional forces depend on the force with which the belt is tensioned by the driven roller and consequently on the thrust force exerted by the hydraulic actuators.

The theoretical analysis estimates that through a thrust of $40\,kN$ for each of the hydraulic actuators, the belt is at such a tension that the forces induced by the tyre are not able to generate the relative movement between the rollers and the belt. Therefore, the belt position controller must ensure that the belt must always be

subjected to a tension value greater than or equal to the desired one during the belt positioning control.
In the following, the developed control system has been divided into two phases:
- the belt tensioning procedure;
- the belt transversal position control (belt centering).

Tensioning procedure

The belt tensioning procedure plays a fundamental role within the steel belt control system. Its task is to bring the belt to the desired tension ensuring the parallelism of the rotation axes of the rollers despite the structural misalignment found.
The procedure has been carried out trying to make it as general as possible, so that it can continue to be used even if the steel belt is replaced.
The basic idea is to bring the belt under tension by controlling the extraction speed of the two actuators. Specifically, the actuators are supplied with a position reference in the form of a ramp corresponding to an extraction speed of $3\ mm/s$. By measuring the pressure inside the chambers of the hydraulic actuators it is possible to estimate the thrust force exerted by them. When these forces reach the one foreseen as the threshold ($40\ kN$), at this point, these positions are memorized and are considered as the minimum position values that the actuators can respectively assume.

The tensioning procedure adopted has been experimentally refined in order to accurately guarantee the actual positions for which the desired thrust force for the actuators have been reached. In the preliminary phase the parallelism between the roller rotational axes is obtained. More specifically, the two actuators move with the same velocity ($3\ mm/s$) until one of them exerts a force of $5\ kN$. At this point, the actuator that has reached the threshold is kept constantly at that position until the second one reaches the same thrust force threshold. The belt tensioning procedure proceeds by providing the actuators with a ramp corresponding to an extraction speed of $1\ mm/s$ as position references until the threshold relating to the desired tensioning is reached, i.e. $40\ kN$ for each actuator.

The introduction of a low slope ramp as a position reference in this phase allows negligible pressures oscillations inside the actuator chambers. Consequently, a better estimation of the thrust forces exerted and of the actuators positions for which the force threshold is reached is obtained.

The positions of the actuators that are obtained at the end of the tensioning procedure are stored as reference value in the model. They constitute the minimum admissible values (that are named $\Delta\xi_{0\_int}$ and $\Delta\xi_{0\_ext}$ in the following) for the actuator positions.

Figure 6.4 refers to the experimental verification test in which the belt tensioning procedure has been tested. The experimental trend further confirms the presence of structural misalignment between the actuators. More specifically, the internal actuator first reaches the intermediate threshold as it is in an advanced position with respect to the external one.

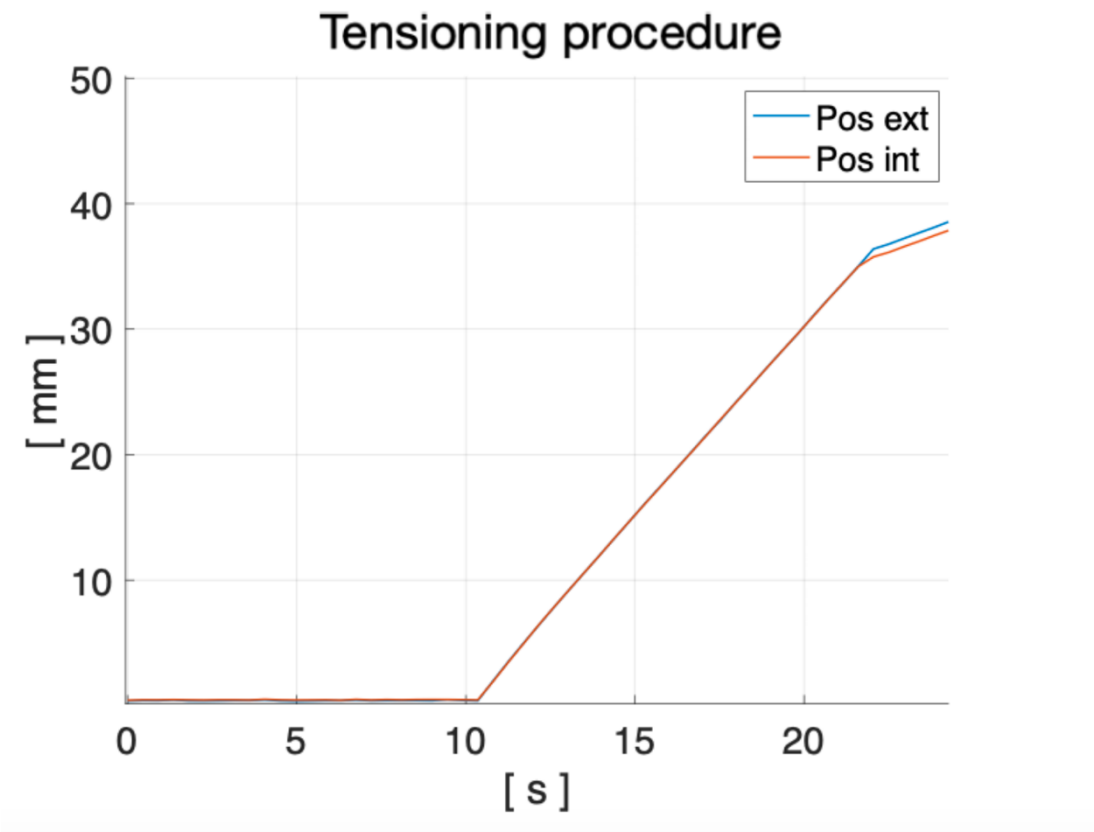

Fig. 6.4: Belt tensioning procedure

Belt centering design

Once the belt tensioning procedure has been carried out, it is possible to develop the control system relating to the positioning of the belt with respect to the rollers.

As anticipated, if the lateral position of the belt is different from the central one ($13\ mm$), the controller must act on the inclination of the axis of rotation of the driven roller so as to induce the lateral translation of the belt towards the desired position.

The architecture of the belt position controller can be schematized as in *figure 6.5*.

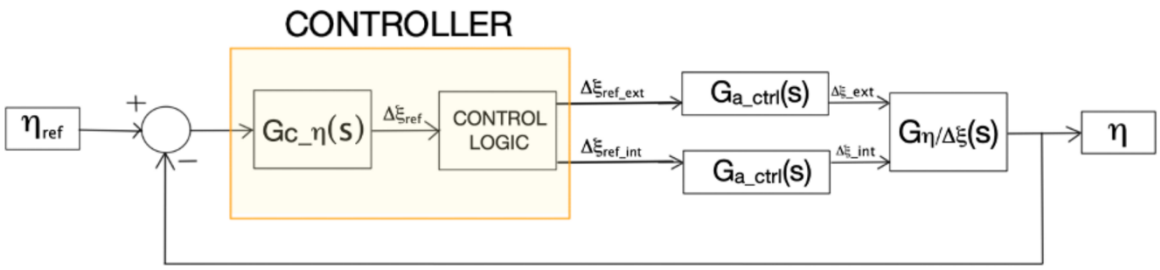

Fig. 6.5: Schematization of the belt centering control system

Within the control architecture it is possible to distinguish the transversal position of the belt η_{ref} to be obtained/maintained, the current transversal position of the belt η, the transfer functions relating to the two actuators controlled in position $G_{a\_ctrl}(s)$, the transfer function regarding the translation of the belt as a function of the misalignment imposed by the actuators $G_{\eta/\Delta\xi}(s)$ and, finally, the belt centering controller.

The controller is represented by the set of the transfer function $G_{c\_\eta}(s)$ and the "CONTROL LOGIC" block. This last block is used to represent the logic used to control the misalignment provided to the hydraulic actuators. Specifically, the block receives as input the total misalignment that must be imposed to the actuators $\Delta\xi_{ref}$ and starting from this it provides the reference positions for each of the two hydraulic actuators ($\Delta\xi_{ext}\ and\ \Delta\xi_{int}$). The logic adopted consists in halving the $\Delta\xi_{ref}$ resulting from $G_{c\_\eta}(s)$ and adding/subtracting it to the reference positions corresponding to the minimum tension for the belt $\Delta\xi_{0\_int}$ and $\Delta\xi_{0\_ext}$ (estimated at end of the tensioning procedure). In order to always guarantee the minimum tension of the belt, the

positions given as a reference to the actuators are saturated to the values corresponding to the minimum tension. This logic allows the belt to be moved to the desired position by eventually keeping one actuator stationary (to the position relative to the lower saturation) and by advancing the other by a value $\Delta\xi_{ref}/2$.

Thanks to the introduction of the "CONTROL LOGIC" block within the control architecture, it is possible to design $G_{c\_\eta}(s)$ by referring to only one of the two actuators controlled in position. This approximation is justified by the fact that the two actuators controlled in position can both be represented through the transfer function $G_{a\_ctrl}(s)$ in the frequency range of interest (*figure 6.2*). Based on these considerations, a simplified control architecture is carried out and depicted in *figure 6.6*.

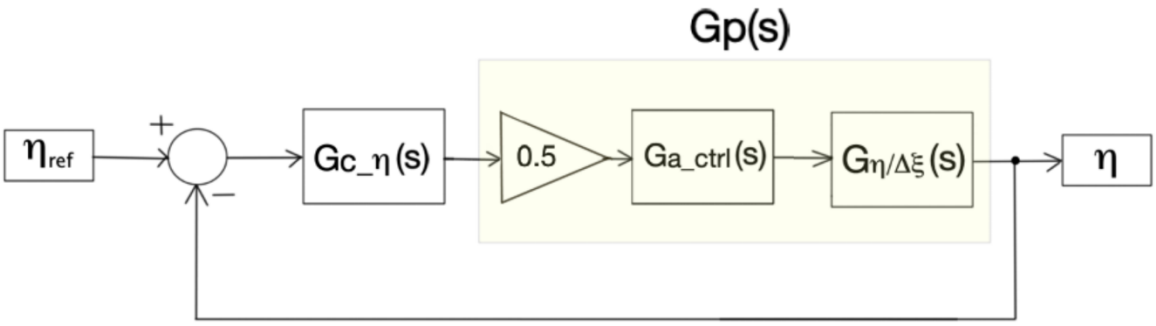

Fig. 6.6: Simplified control architecture for the belt centering

The system to be controlled can be considered as the series of transfer functions relating to the actuators controlled in position and the translation of the belt according to the misalignment of the actuators, it can be expressed as:

$$G_p(s) = 0.5 * G_{a_{ctrl}}(s) * G_{\frac{\eta}{\Delta\xi}}(s) =$$

$$= \frac{4.061e04\ (s+50)\ (s+10)}{s\ (s+550)^2\ (s+19)\ (s^2 + 41.8s + 484)}\ n$$

where n is the rotation velocity in rps.

The control system for the position of the belt must be designed considering that the width of the steel belt has imperfections. In chapter 4 was underlined as the belt shows oscillations having a width of approximately $0.4\ mm$ along the perimeter of the belt. When the belt is rotating, these imperfections are detected by the micrometer and can be represented as a noise whose frequency depends linearly on the belt speed. These fluctuations can be considered as a disturbance acting downstream of the plant to be controlled and, therefore, the link with the position of the belt can be associated with the sensitivity transfer function $S(s)$ of the control system. Since the frequency of the fluctuations is a multiple of the rotation speed, it is not possible to create a control system capable of attenuating the high frequency noise on the system, but by acting on the control system bandwidth, it is possible to make these fluctuations pass without being amplified.

The control system for the position of the belt is designed on the basis of the following requirements:

- $|e_r^{\infty}| = 0$, null steady-state error in following a step reference;
- $\hat{s}\ \% < 5\%$, as a limit for the overshoot;
- $t_{s,5\%}$ of the order of $20\ s$ so as not to generate significant pressure peaks inside the hydraulic actuators.

Referring to the transfer function of the system to be controlled $G_p(s)$, it is possible to note how the presence of the origin pole is able to guarantee the stationary requirements in the step response. It follows that the controller can be made without poles in the origin and the control system will be defined as type 1.
The controller design has been based on the loop-shaping of the open loop function $L(s)$ through the use of Nichols diagrams.
Starting from the requirements regarding the transient, a damping coefficient around 0.69 and a crossover pulsation around $0.29\ rad/s$ have been estimated.
The peculiarity with respect to the position control system for actuators lies in the fact that $G_p(s)$ linearly depends on the rotation speed n, which causes the variation of the generalized *DC* gain. The controller design has been done by freeing itself from the rotation speed, i.e. a unit rotation speed is considered during the design phase and

then the term n is introduced directly as a further dividing in the transfer function obtained for the controller $G_{c\_\eta}(s)$. This is possible since the TTB is equipped with a torque-meter capable of measuring the rotation speed of the driving roller.
Figure 6.7 shows the initial situation, it is possible to notice how it is sufficient to act through a proportional control that allows to define the desired bandwidth.

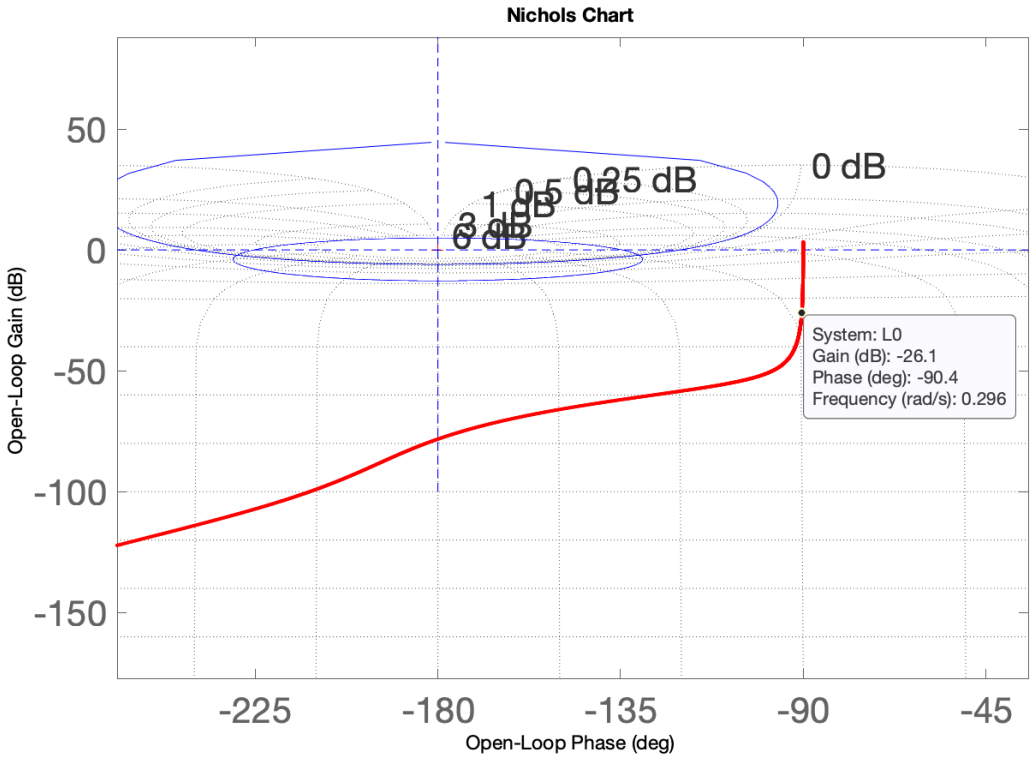

Fig. 6.7: Initial open-loop transfer function $L(s)$

The proportional controller was implemented within the test bench, but the results obtained were not considered satisfactory. More specifically, the belt reaches the reference position with a non-zero steady-state error. This behaviour is attributable to the asymmetry in the actual actuation systems of the TTB.

In order to solve the problem, a new controller $G_{c\_\eta}(s)$ capable of eliminating the steady-state error has been designed. This has been obtained by introducing an integral action, i.e. a pole in the origin in the controller.
In this case, the controller design is a little bit more complex because a higher phase recovery is required in the working frequencies range.

Figure 6.8 shows the Nichols diagram of the open loop transfer function $L(s)$ at the beginning of the design and after the use of the designed controller:

$$G_{c\_\eta}(s) = \frac{358.4\ (s+0.2)(s+0.02)}{s\ (s+3.2)(s+0.32)\ n}$$

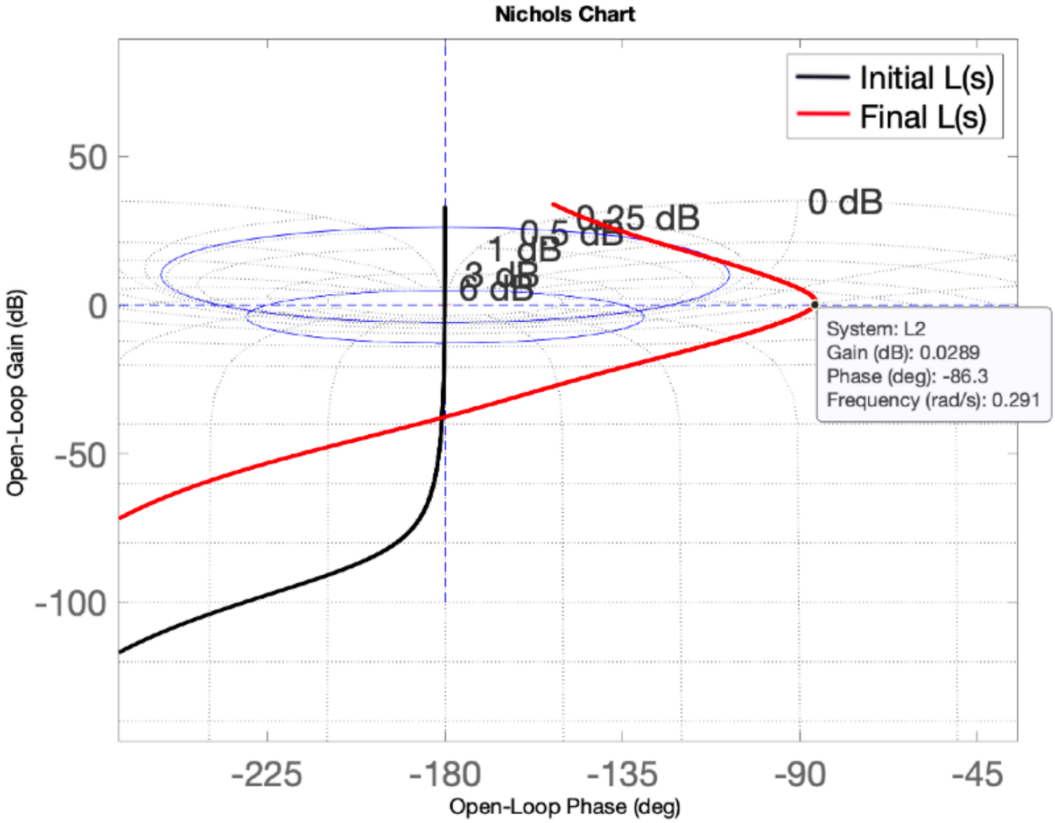

Fig. 6.8: Nichols diagram of $L(s)$ before and after the implementation of the controller

The belt centering controller calculates the reference misalignment to be imposed on the hydraulic actuators $\Delta\xi_{ref}\ [mm]$ based on the rotation speed n, the desired transversal position of the belt $\eta_{ref}\ [mm]$ and the measured one $\eta\ [mm]$.

In order to avoid overloading the driven roller bearings, it was decided to limit the maximum misalignment for the hydraulic actuators to $4\ mm$. As for the control of the position of the actuators, the $G_{c\_\eta}(s)$ controller was then implemented through an architecture able to mitigate the eventual windup phenomenon.

Figures 6.9 and *6.10* show the implementation of the controller and the control logic directly implemented in the Simulink environment.

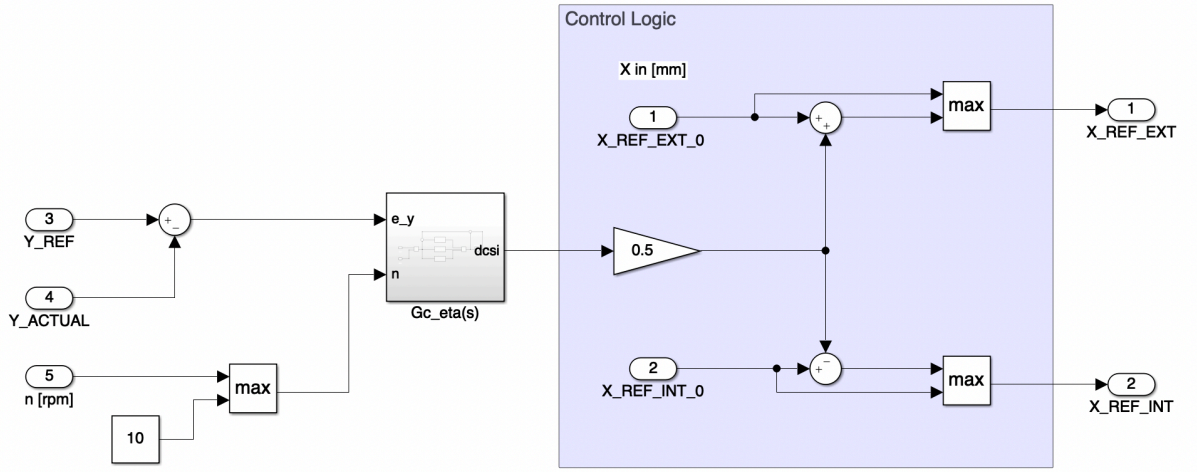

Fig. 6.9: Controller and control logic designed

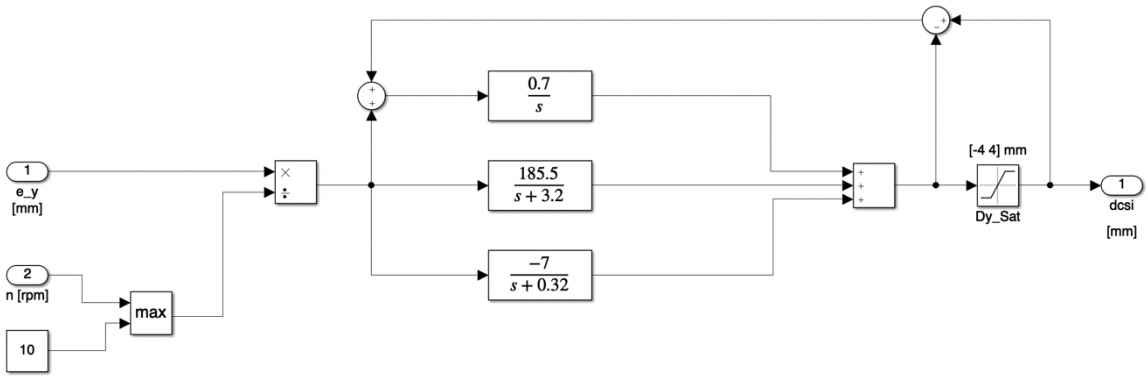

Fig. 6.10: Anti-windup controller designed

VERIFICATION AND VALIDATION OF THE BELT CENTERING SYSTEM

As anticipated, in order to carry out the tests on the tyre, it is necessary that the steel belt is at a tension that prevents the forces produced by the tyre from causing a lateral translation of the belt. Furthermore, if the belt is in a position different from the one corresponding to the centering with respect to the rollers (for example after the initial tensioning procedure), the belt must self-center through its rotation.

In order to verify that the built control system is able to perform both tasks simultaneously, an experimental analysis was carried out based on the step response for the lateral position of the belt η.

The *Figure 6.11* shows the desired lateral reference position $\eta_{ref}\ [mm]$ (red line) and the measured one $\eta\ [mm]$ (blu line).

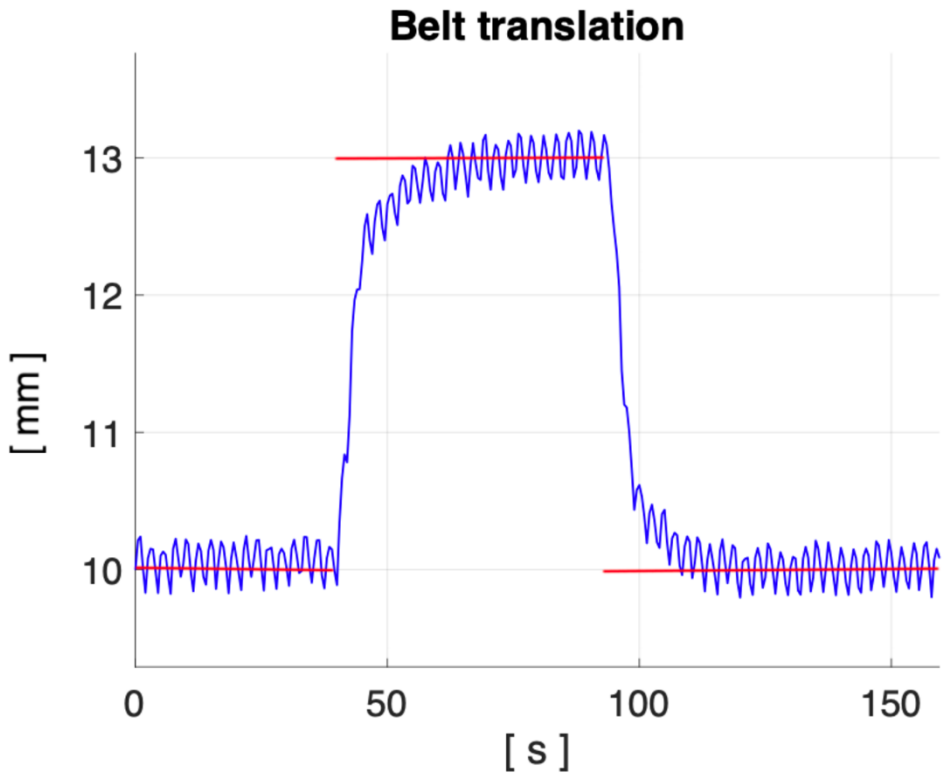

6.11: Step response on η measured on the TTB

Based on the shown response, it is possible to state that both the stationary and transient requirements are satisfied. More specifically, it can be noted that the steady-state error and the overshoot are close to zero and the settling time $t_{s,5\%}$ is in the order of $20\ s$.

A similar test was also repeated by using the TTB model in order to validate it. The *Figure 6.12* shows the comparison between the numerical and the experimental results.

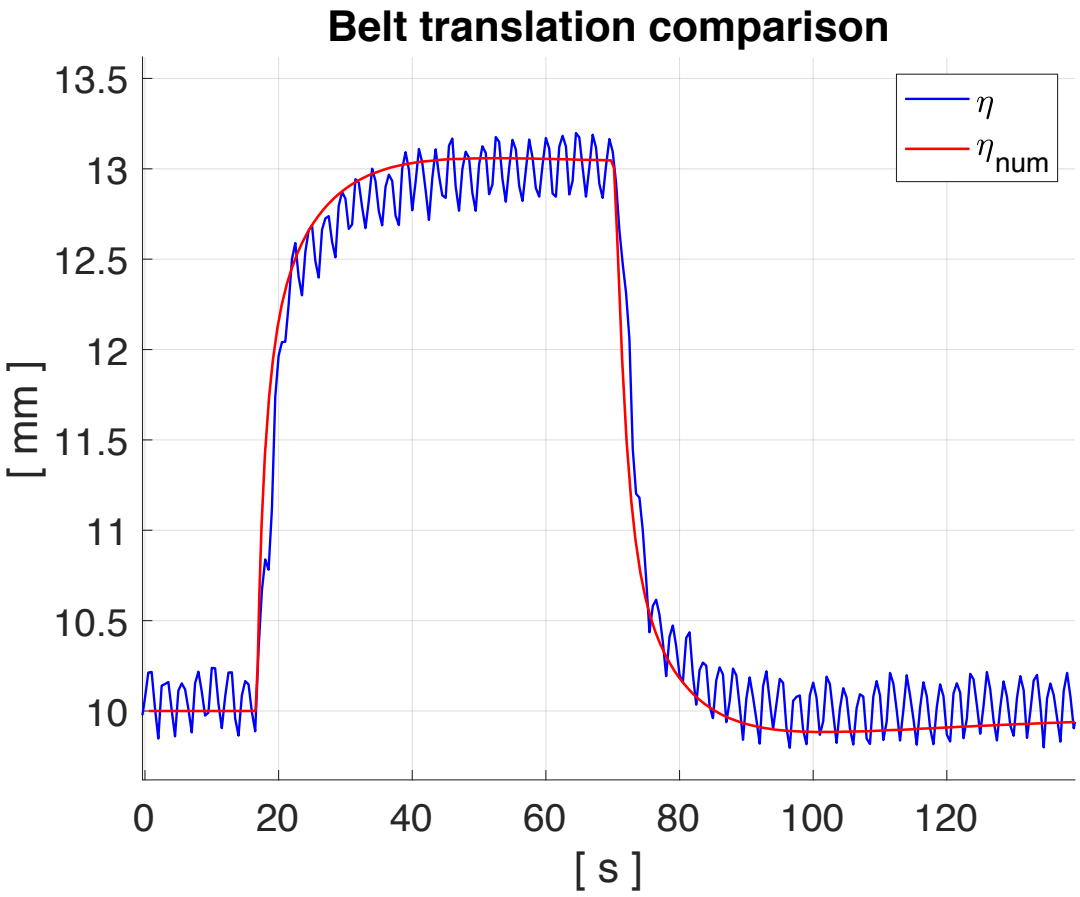

6.12: Numerical and Experimental Steps response comparison

6.3 CONTROLLER IMPLEMENTED INSIDE THE PLC

The control system developed for the tyre test bench was created in the Simulink environment and integrated directly into the PLC via TwinCat 3. This operation was possible since the TTB is equipped with a PLC capable of working in real time with the blocks generated in the Matlab's Simulink environment.

Figures 6.13, 6.14 and *6.15* show the controller as a whole.

Figure 6.13 shows the signals through which the controller communicates with the PLC. The INPUTS represent the signals coming from the TwinCat environment and they can be classified as: the measurements made on the test bench (piston positions, pressures in the cylinder chambers of the hydraulic actuators, transversal

position of the belt and rotation speed of the drive roller), the digital signals coming from the user interface (ENABLE, START/STOP) and the parameters related to the tensioning procedure. It is important to emphasize that the parameters coming from TwinCat can be easily changed if required.

The controller produces as OUTPUT the command signals relating to the hydraulic actuators and a flag (*Tension done*) to communicate the end of the belt tensioning procedure.

Figure 6.14 shows all the variables that are used within the controller, both those coming from the PLC and those internal to the controller or calculated inside it.

Figure 6.15 represents the actual controller, it possible to see how this is managed by the state machine (in yellow), whose content is expressed by the state diagram created through StateFlow and shown in *figure 6.16*.

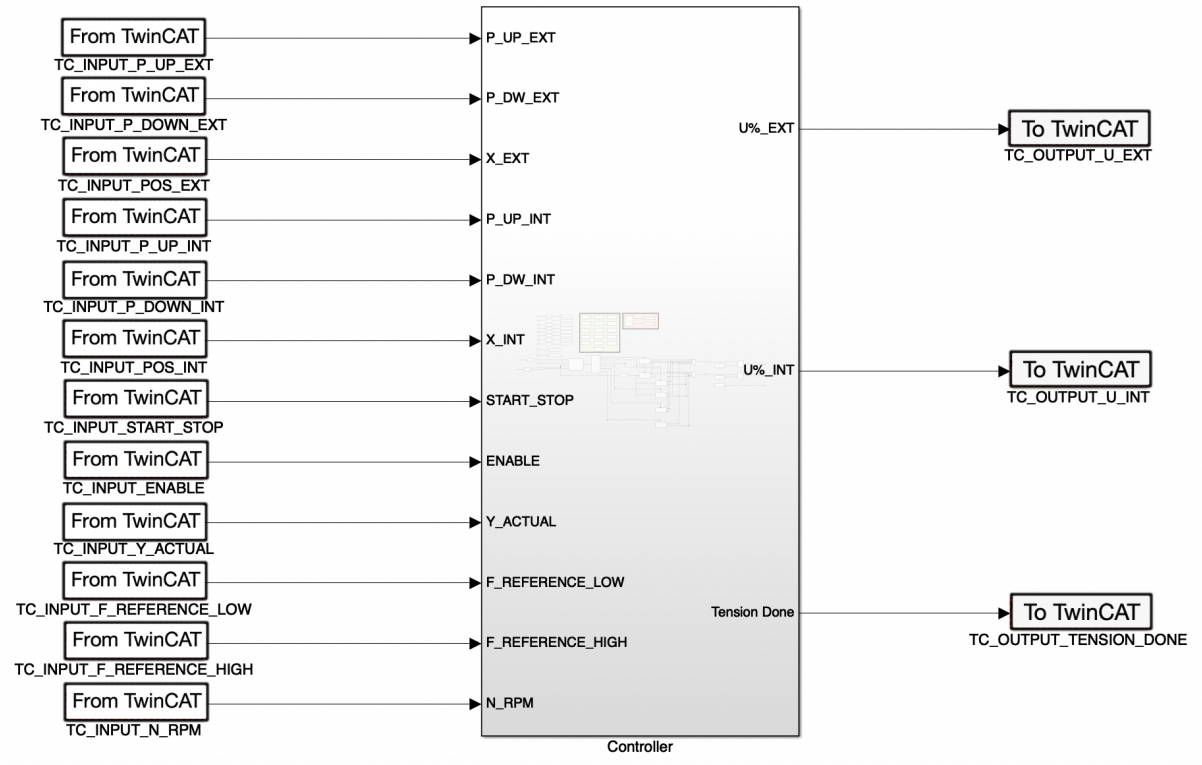

Fig. 6.13: Controller from the highest-level point of view

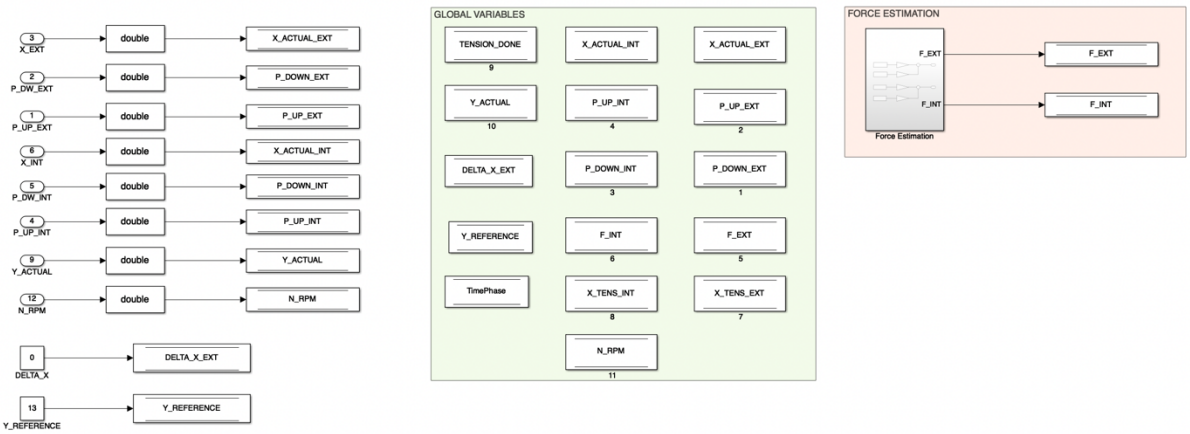

Fig. 6.14: Variables used inside the controller

In order to activate the controller, the user must provide the ENABLE signal via the appropriate user interface.

Once the controller is active, the user can activate or deactivate the belt tensioning procedure through the appropriate START_STOP signal on the interface.

Once the tensioning procedure is completed, the *Tension done* flag is activated by the controller to communicate the end of the tensioning phase. From this moment, the belt centering control begins, and for this purpose, the user can put the steel belt in rotation by controlling the rotation speed of the driving roller via the specific user interface.

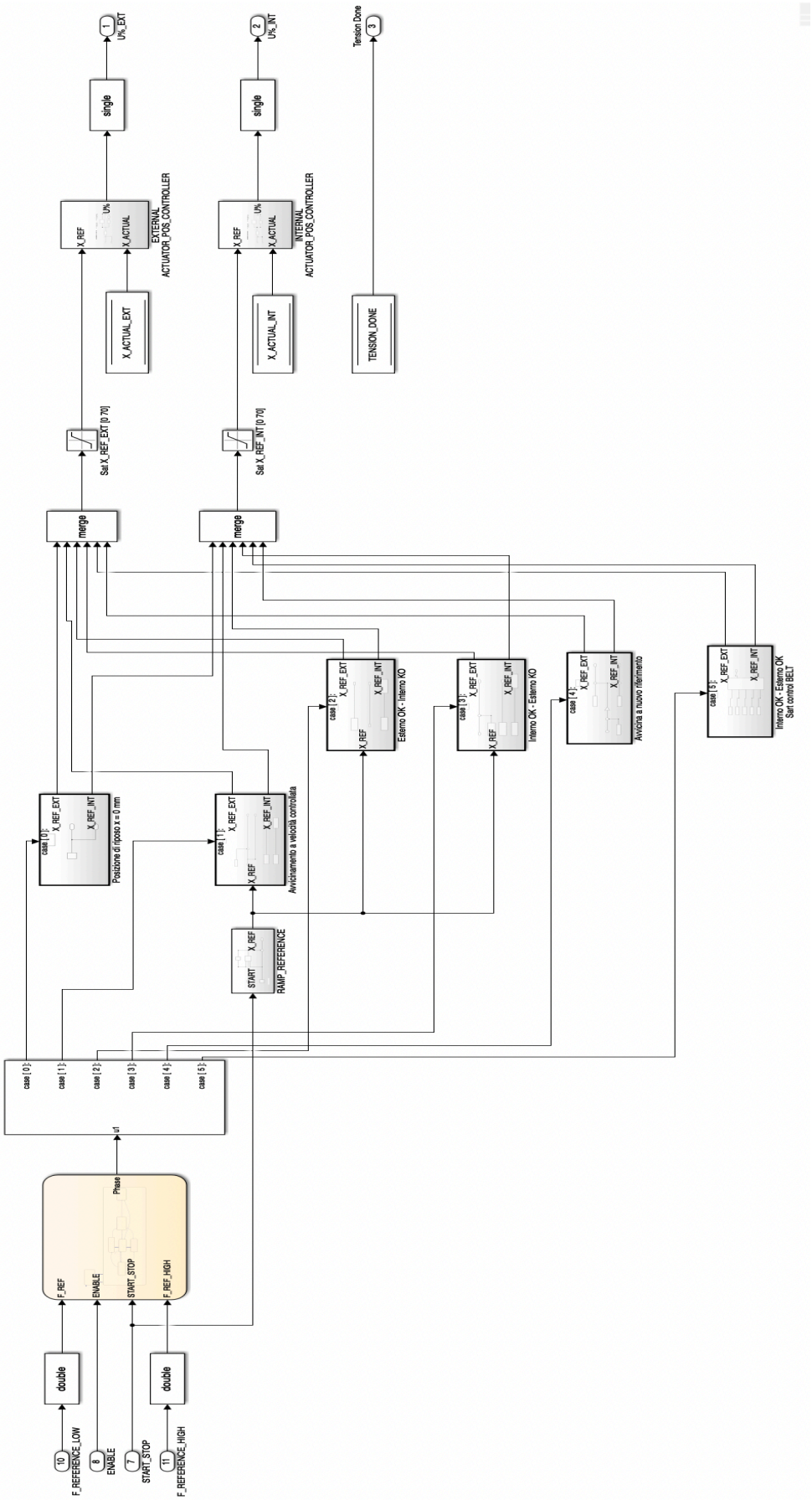

Fig. 6.15: Controller implemented in Simulink

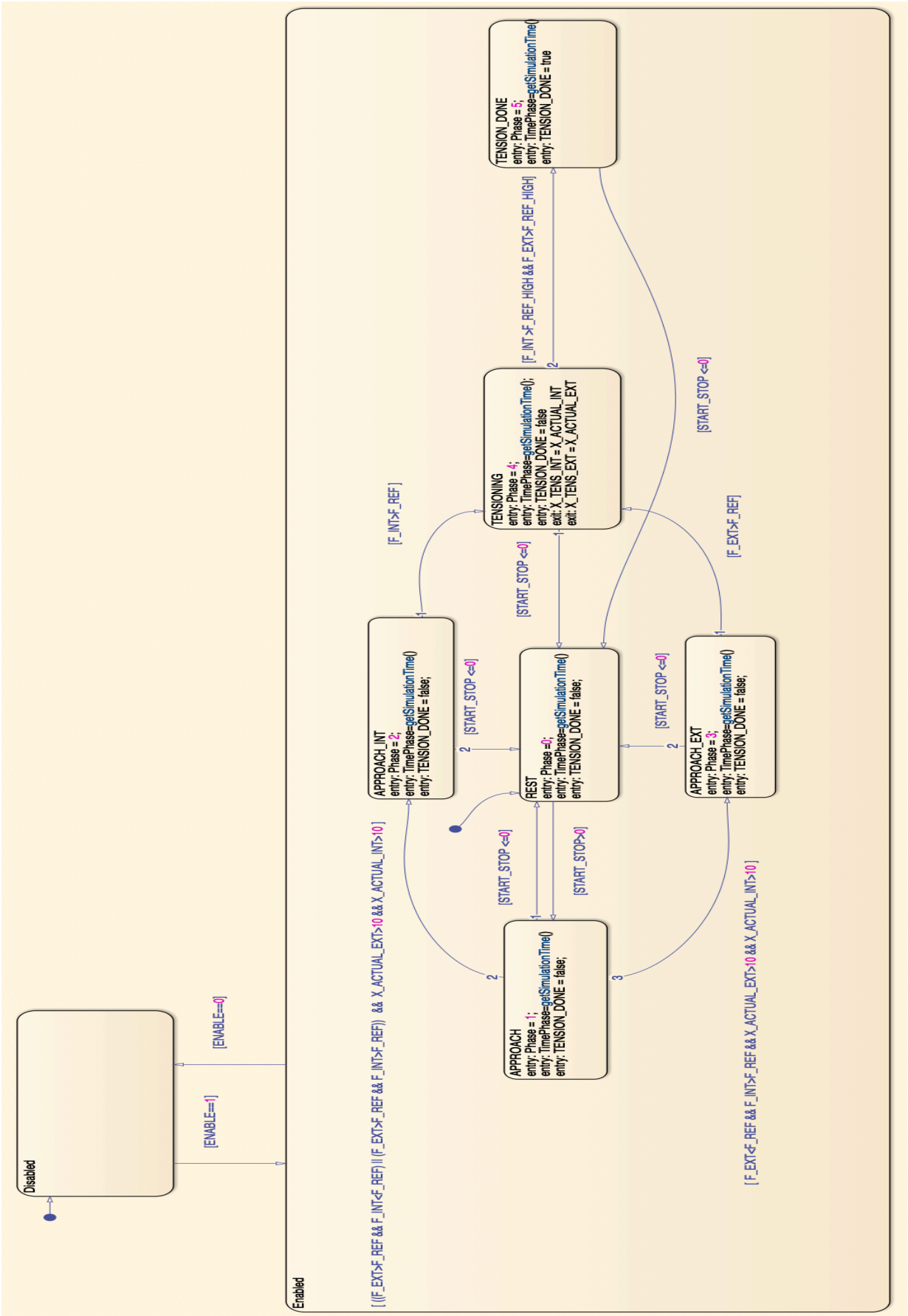

Fig. 6.16: State machine implemented through StateFlow

Conclusions

The Tyre Test Bench analyzed in the present thesis work shows a steel belt that is would around a couple of rollers. The rollers have to moves the belt by guaranteeing the belt tensioning and the belt centering during the tyre test procedure.

In the first part of this work, the stress analysis of the belt has been developed and it was observed that a minimum belt tension of about $80\ kN$ must be guarantee in order to keep the belt centered with respect to the rollers. This means that the two actuators acting on the driven roller have to perform the belt positioning control by applying a minimum thrust force of $40\ kN$.

The physical model of the hydraulic actuation system has been developed and experimentally validated from the static and dynamic point of view.

The control system of the actuators has been designed in order to control their position. The obtained controlled system is of the second type in order to control both piston position and the velocity.

The belt positioning control system has been developed on the base of the controlled actuators systems. The resulting control system is able to bring the belt at the desired position and to guarantee the minimum belt tension.

Finally, a belt tensioning procedure able to automatically recover the structural misalignment of the mechanical system has been developed and experimentally tested.

Bibliografy

[1] A. Gent and J. Walter, “Pneumatic Tire,” *Mech. Eng. Fac. Res.*, Sep. 2006.

[2] H. B. Pacejka, *Tyre and vehicle dynamics*. Butterworth-Heinemann, 2006.

[3] A. Morelli, *Progetto dell’autoveicolo : concetti di base*. CELID, 1999.

[4] M. Guiggiani, *The Science of Vehicle Dynamics*. Cham: Springer International Publishing, 2018.

[5] M. M. Joop P. Pauwelussen, Wouter Dalhuijsen, “Tyre dynamics, tyre as a vehicle component,” 2007.

[6] C. Dongiovanni and A. Tonoli, “Tutto ruota intorno a un test,” *Autotecnica*, pp. 122–128, 2004.

[7] *Tec-science*: https://www.tec-science.com/mechanical-power-transmission/belt-drive/maximum-belt-stress

[8] G. Belforte, Meccanica applicate alle macchine. Levrotto e Bella, 1983

[9] *Grices hydraulic cylinders*: cht series (datasheet)

[10] Sunghun Kim, Hubertus Murrenhoff, “Measurement of Effective Bulk Modulus for Hydraulic Oil at Low Pressure”

[11] *Direct Operated Proportional DC Valve*: Series D1FP (datasheet)

Thanks

At the end of this paper, I would like to mention some of the people, without whom this thesis work would not even exist.

I thank my supervisors Canale Massimo and Galvagno Enrico, who provided numerous suggestions throughout the activity carried out.

I thank Andrea Bottega for the help and patience with which he has followed me from day one.

I sincerely thank my parents. I owe to you everything I have achieved up to now.